Development of Luminescent Carbon Nanoparticles for Authentication of Petroleum Products and Investigation of Phototherapy Potential of Nanoparticles

by

Kübra Nur Özvural Sertçelik

A Dissertation Submitted to the
Graduate School of Sciences and Engineering
in Partial Fulfillment of the Requirements for
the Degree of

Master of Science

in

Materials Science and Engineering

January 21, 2022

Development of Luminescent Carbon Nanoparticles for Authentication of Petroleum Products and Investigation of Phototherapy Potential of Nanoparticles

Koç University

Graduate School of Sciences and Engineering

This is to certify that I have examined this copy of a master's thesis by

Kübra Nur Özvural Sertçelik

and have found that it is complete and satisfactory in all respects,
and that any and all revisions required by the final
examining committee have been made.

Committee Members:

_____

Prof. Havva Yağcı Acar (Advisor)

_____

Prof. Duygu Avcı Semiz

_____

Asst. Prof. Safacan Kölemen

Date: _____

Dedicated to Hasan

ABSTRACT

Development of Luminescent Carbon Nanoparticles for Authentication of Petroleum Products and Investigation of Phototherapy Potential of Nanoparticles

Kübra Nur Özvural Sertçelik

Master of Science in Materials Science and Engineering

January 21, 2022

Nanomaterials were exploited in many engineered materials since their properties can be controlled and modified by tunning their size. The relatively new member of the nanomaterials portfolio is the luminescent carbon dots (CD) which are more or less considered biocompatible, non-toxic, and environmentally friendly. However, the development of CDs with different luminescence properties can be challenging. In this thesis, the effects of small organic precursors, N-, O-, P- doping, and solvent (polarity and reducing power) on the emission wavelength of CDs were investigated. In literature, most CDs have blue emission. Examples to CDs with different emission colors exist, yet most of them have major drawbacks such as non-reproducibility, low colloidal stability. A portfolio of colloidally stable, reproducible, easily manufactured CDs to address these disadvantages was developed in this thesis. The second part of the thesis focuses on using CDs in the authentication of petroleum products as photostable optical tags. In the third part of the thesis, one of the most popular photosensitizers, BODIPY, was loaded to highly biocompatible superparamagnetic iron oxide nanoparticles for enhanced delivery of BODIPY to cancer cells and achieve highly selective and enhanced photodynamic therapy. Lastly, the phototherapy potential of aqueous red-emitting CD produced in this thesis was investigated.

ÖZETÇE

Petrol Ürünlerinin Doğrulanması için Karbon Nanoparçacıklarının Geliştirilmesi ve Nanoparçacıkların Fototerapi Potansiyelinin İncelenmesi

Kübra Nur Özvural Sertçelik

Malzeme Bilimi ve Mühendisliği, Yüksek Lisans

21 Ocak 2022

Nanomalzemeler boyutlarında yapılabilen değişikliklerle, sahip oldukları özelliklerin de kontrol edilip değiştirilebilmesine imkan sağlayan en önemli tasarlanmış malzeme kollarından biridir. Bu malzeme kollarından görece yeni sayılabilecek karbon bazlı nanoparçacıklar mevcut uygulamalar için daha biyouyumlu, çevre dostu ve toksik olmayan bir alternatif sunmaktadır. Ancak, farklı lüminesans özelliklere sahip karbon noktacıkları geliştirmek kolay bir görev olmayabilir. Bu tez çalışmasında, küçük organic hammaddelerin kullanımının, -N, -O, -P katkılamalarının ve çözücünün karbon noktacıklarının emisyon dalgaboylarına etkisi incelendi. Literatürde birçok farklı renk alternatifi olmasına rağmen bu karbon noktacıklarının çoğu yeniden üretilememe, düşük kolloidal stabilite gösterme ve baskın olarak mavi emisyona sahip olma dezavantajlarını barındırırlar. Bu tezde, bu sorunların çözümünü hedefleyen bir karbon noktacık portfolyosu geliştirildi ve bunların petrol ürünlerinin doğrulamasında optik işaretleyici olarak kullanılması üzerine çalışıldı. Tezin üçüncü kısmında, en popüler foto duyarlaştırıcılardan olan BODIPY'nin yüksek biyouyumlu super paramanyetik demir oksit nanoparçacıklarına yüklenerek kanser hücrelerine daha fazla taşınması sağlanmış, yüksek seçicilik ve geliştirilmiş fotodinamik terapi kombinasyonu sağlanmıştır. Son olarak, suda çözünen kırmızı emisyona sahip karbon noktacıklarının fototerapi potansiyeli incelenmiştir.

ACKNOWLEDGEMENTS

Our lives are connected like the roots of trees in a forest, and they nourish each other, stand together, and help to survive. Now, I would like to sincerely thank all these lives who have helped me get to this point.

Many thanks to my advisor, Prof. Havva Yağcı Acar, who was an ideal model for me at the cross-section of industry and academia, and I am truly grateful for her guidance, support, and endless energy to make me think out of the box. Also, thanks to my thesis committee members, Asst. Prof. Safacan Kölemen and Prof. Dr. Duygu Avcı Semiz for their guidance, support, and time.

I would like to thank Dr. Kübra Onbaşlı who taught me everything I know about cell studies with nanomaterials and as a chemist, this was a great chance to build a bridge between biology and chemistry. I am grateful for her support and encouragement that I feel all the time in both academia and life.

I must mention one person here since I would not have come this far without her, my dear friend Pelda Akin. During the last two years, together, we learned, worked, and sang a lot and I could not be more grateful to have such a golden heart friend.

I would like to thank Dr. Hadi Jahangiri and Dr. Barış Yağcı from KUYTAM, Prof. Cleva Ow-Yang from Sabancı University and Asst. Prof. Safacan Kölemen's PhD student Toghrul Almammadov for their friendly attitude and help in instrumental and experimental issues. I am thankful to previous and current members of the Polymers and Nanomaterials Research Group.

I have had many amazing teachers since my elementary school days, and I am grateful to all of them for their valuable lessons. Nonetheless, I would like to express my special thanks to Canan Çevikel, Derya Ebeperi, Mehmet Arslan, Ayperi Neslihan Gök, Mahmut Süreyya Karaoğlu, Ayperi Durmuş, Berna Yılmaz, Paul Harley, Dr. William Coker, Dr. Gamze Ulusoy Ghobadi, Asst. Prof. Ferdi Karadaş, Asst. Prof. Seymur Jahangirov and Asst. Prof. Hasan Demirci for teaching me to dream, be brave, and think creatively. I am deeply grateful to them for inspiring me to go my own way.

Thanks to Quantag Nanotechnologies for the funding and support they provided us in the carbon dot project.

Thanks to the Scientific and Technological Research Council of Turkey, TÜBİTAK, for awarding me the 2210-E Graduate Scholarship, providing me with the financial means to complete this thesis. And finally, thanks to my husband Hasan Berk Sertçelik, my parents Muammer and Sevinç Özvural, my sister Fatma Nur Özvural, and numerous friends like family to me who endured this long process with me, always offering support and love.

TABLE OF CONTENTS

LIST OF TABLES

LIST OF FIGURES

ABBREVIATIONS

BODIPY	Boron Dipyrromethene
bPEI	Branched Polyethyleneimine
CD	Carbon Dot
Cet	Cetuximab
CNDs	Carbon Nano Dots
CQDs	Carbon Quantum Dots
DMF	Dimethylformamide
DSC	Dye-sensitized Solar Cells
EA	Ethyl Acetate
EtOH	Ethanol
FBS	Fetal Bovine Serum
FDA	Food and Drug Administration
FRET	Fluorescence Resonance Energy Transfer
FTIR	Fourier Transform Infrared Spectroscopy
GQDs	Graphene Quantum Dots
HER	Hydrogen Evolution Reaction
HOMO	Highest Occupied Molecular Orbital
LUMO	Lowest Unoccupied Molecular Orbital
MTT	Thiazolyl Blue Tetrazolium Bromide
NIR	Near Infrared
OA	Oleylamine
OECD	Organization for Economic Cooperation and Development
oPDA	ortho-Phenylenediamine
PBS	Phosphate Buffered Saline
PDT	Photodynamic Therapy
PEC	Photoelectrochemical Cell
PL	Photoluminescence
pPDA	para-Phenylenediamine

PS	Photosensitizer
PTT	Photothermal Therapy
QCE	Quantum Confinement Effect
QDs	Quantum Dots
QY	Quantum Yield
ROS	Reactive Oxygen Species
SPION	Superparamagnetic Iron Oxide Nanoparticles
TEL	Tetraethyl Lead
TEM	Transmission Electron Microscopy
TNP	Trinitropyrene
UV	Ultraviolet
XPS	X-ray Photoelectron Spectroscopy
XRD	X-ray Diffraction

Chapter 1: INTRODUCTION

Nanomaterials are chemical substances that possess at least one external dimension measuring 1-100 nm. On such a small scale, they demonstrate quite different physical, chemical, and optical properties than their bulk-form (Xu et al., 2016). This extraordinary behavior of nanomaterials has drawn significant attention which leads to expansion in nanomaterial variety and consequently, increasing demand. Possible candidates addressing this interest are metal nanoparticles, metal oxide nanoparticles, chalcogenide nanoparticles, and more recently carbon-based nanoparticles. Because of the environmentally friendly nature of carbon elements, carbon-based nanoparticles have the advantage to create more biocompatible, non-toxic, and stable designs. Hence, the first part of this thesis will focus on understanding the design parameters to tune their properties which will be followed by the second part focusing on their exploitation as a fluorescent marker for liquid petroleum products.

1.1 Nanoparticles

At the macroscopic level, materials have physical properties which are independent of size, shape, and geometry. Therefore, chemical, physical, optical, electrical, magnetic, etc. properties can be only changed by changing the molecular structure or composition of the matter. However, this general information will not be completely accurate when moving from the macroscale to the nanoscale since quantum mechanics overcome classical mechanics at this extremely small scale. Hereby, a change in the size of the nanoscale material changes chemical and physical properties such as melting point, reactivity, optical, electrical, and magnetic properties dramatically, and provides unique features which are not possible at the macroscopic level.

In this thesis, the main size-dependent property that will be investigated and exploited is *photoluminescence*. Photoluminescence is the emission of light from a material exposed to electromagnetic radiation (Zhu et al., 2015).

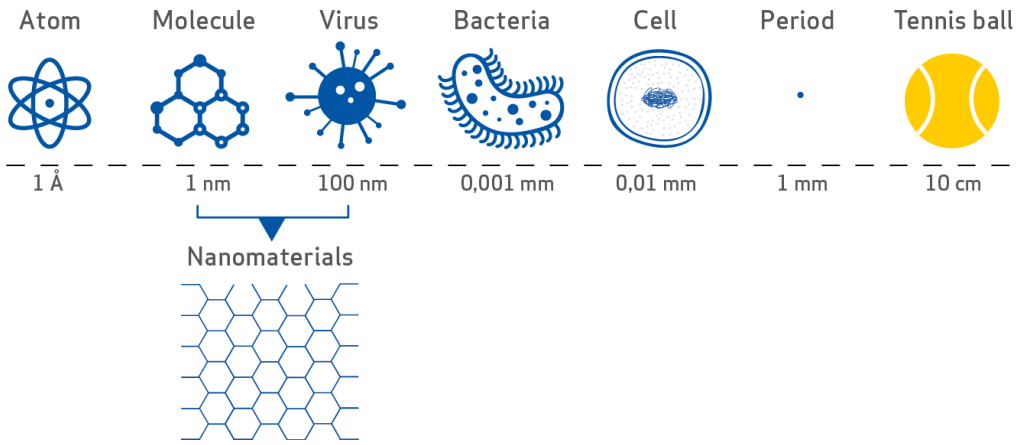

Figure 1.1. Scheme of size comparison of nanomaterials with general objects. (European Chemicals Agency, 2016).

This size-dependent luminescence feature at the nanoscale is highly worthy for material scientists because it opens a way to create new materials for numerous technological needs and hence many types of engineered nanomaterials have been developed, such as luminescent quantum dots, gold nanoparticles, and recently carbon dots (CDs). This thesis specifically focuses on CDs as luminescent nanoparticles from its design, synthesis, and investigation of their potentials as optical tags for fuel and in biomedical applications.

1.1.1 Carbon Dots

Carbon dots (CDs) are considered as a group of ultra-small and photoluminescent nanoparticles such as graphene quantum dots (GQDs), carbon quantum dots (CQDs), carbon nano-dots (CNDs), and polymer dots (Zhu et al., 2015). In the scientific community, there is no consensus about the origin of their luminescence. However, several highly important mechanisms were proposed such as bandgap transitions of conjugated π-domains and surface defect states (Yan et al., 2019). The conjugated π-domains act as a carbon-core fluorescence center based on another phenomenon which is called the *quantum confinement effect* (QCE) (Yan et al., 2019). This effect is considered as the change of continuous energy bands to discrete energy levels and increasing bandgap with decreased size of CDs which causes to blue shift. This mechanism includes the direct transition of conduction band electrons to valence band holes, and this is the reason to call it bandgap fluorescence (Yan et al., 2019). Another mechanism is surface defect states which are based on dominant surface groups over carbon core. These surface

groups may be sp^2 and sp^3 hybrid carbons or other defects which are commonly originated by surface oxidation, and they capture the exciting photons during their relaxation to ground state (Fang et al., 2017).

CDs are generally synthesized from conjugated carbon structures by using different synthesis methods some of which are highly straightforward and low-cost which is a significant industrial advantage. Their unique properties depend on size, surface structure, reaction solvent, etc. (Wang & Hu, 2014). Therefore, their properties may be tuned for a specific application. Besides, CDs are reported as highly biocompatible materials with good stability in the biological environment, making them one of the most promising candidates for both commodity products and biomedical applications (Jia et al., 2020). If the surface of CDs is functionalized different groups such as carboxylic acid, amine, or hydroxyl groups, new chemical, physical, optical properties may be obtained (Li & Dong, 2018) for different applications such as fluorescent imaging (Liu et al., 2016), bio-sensing (Loo et al., 2016), photocatalysis (Liu et al., 2015), security (Jiang et al., 2018), etc.

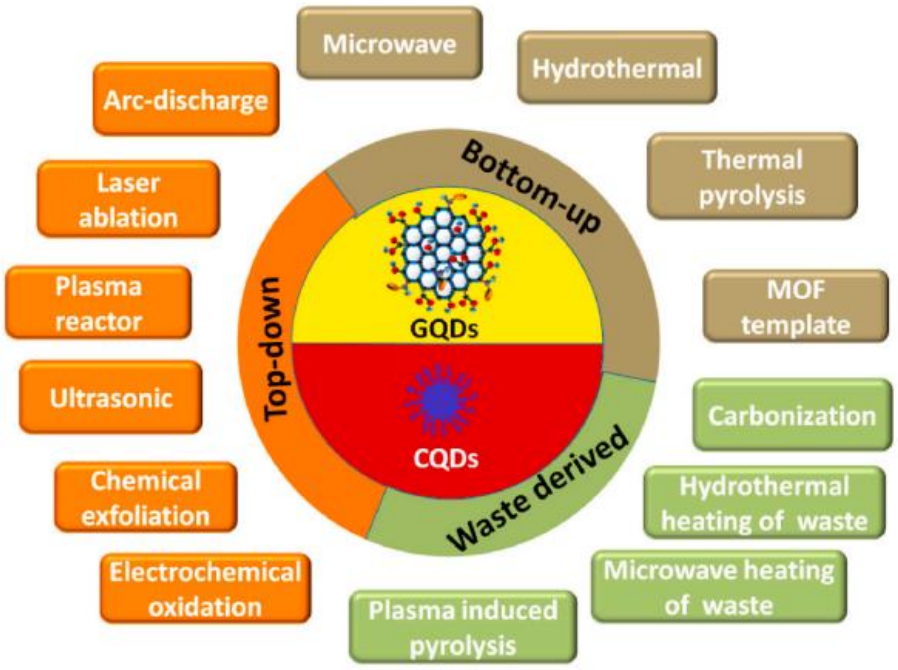

Figure 1.2. Scheme of synthesis method for CDs (Ghosh et al., 2021).

CDs are synthesized either via chemical or physical methods. Physical methods include laser ablation, plasma treatment, and arc discharge, which are relatively more difficult and expensive methods than chemical methods. The most widely used chemical

methods are electrochemical synthesis, hydrothermal treatment, microwave irradiation, and solution chemistry (Li et al., 2012).

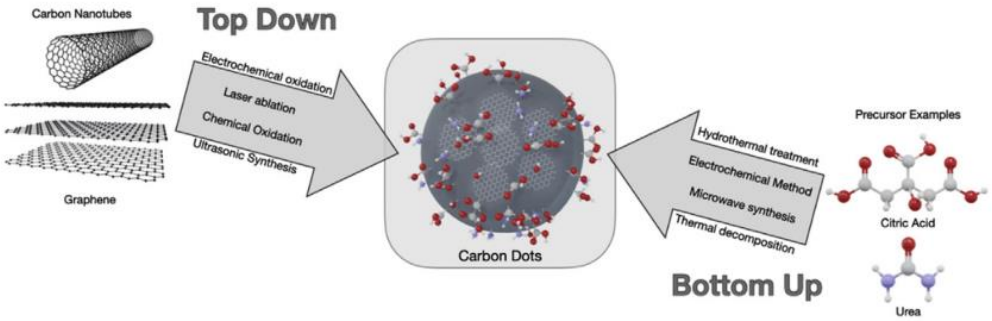

Figure 1.3. Diagram of two different approaches for CDs synthesis; top-down and bottom-up (Ross et al., 2020).

These synthesis methods are also classified into two extensive groups, top-down and bottom-up approaches (Ghosh et al., 2021). Bottom-up methods such as hydrothermal treatment, microwave irradiation, or electrochemical synthesis are based on fabricating CDs from smaller organic precursors such as citric acid, urea by pyrolysis or carbonization (Ross et al., 2020).

1.1.2 Hydrothermal Synthesis of Carbon Dots

The most common chemical synthesis method of CDs is hydrothermal treatment a relatively low-cost, non-toxic, environmentally friendly procedure that converts various precursors to CDs in an acceptable time. In this method, typically, a solution of an organic precursor is sealed and reacted in a hydrothermal reactor at high temperatures. Synthesis may be performed in aqueous or organic solvents, and optical properties and solubility may be changed by surface functionalization (Ross et al., 2020). Therefore, after hydrothermal carbonization followed by extraction, there may be both hydrophobic (in organic solvent) and hydrophilic (in water) CDs. For example, the luminescence of hydrophilic CDs may be shifted to longer wavelengths by acid treatment (Wang & Hu, 2014). But the disadvantage is poor control over the size of CDs and low quantum yield (QY) compared with other methods such as microwave or calcination (Crista et al., 2020).

Table 1.1. Synthesis of CDs from small organic molecules via hydrothermal treatment (Sharma & Das, 2019).

S. No.	Source	Method of preparation	Doping (d)/surface passivating (p) agent	Color	Size (nm)
1.	L-Ascorbic acid	Hydrothermal treatment	–	Violet	2
2.	Glucosamine HCl	Hydrothermal treatment	Glucosamine HCl (d)	Green	15–70
3.	Glucose, monopotassium phosphate	Hydrothermal treatment	–	Violet	1.83–3.83
4.	Dopamine	Hydrothermal treatment	–	Blue, yellow, green	3.8
5.	Sodium citrate	Hydrothermal treatment	–	Blue	1.59
6.	Citric acid and ethylene diamine	Hydrothermal treatment	–	Blue	2–6
7.	bPEI, ammonium persulfate	Hydrothermal synthesis	bPEI	Blue	3–4
8.	Streptomycin	Hydrothermal treatment	–	Violet	2.97
9.	Histidine, NaOH	Hydrothermal treatment	–	Blue	3–5
10.	Ammonium citrate, ethylenediamine	Hydrothermal treatment	N (d)	Blue	4.8
11.	L-Serine, L-cystine	Hydrothermal treatment	N, S (d)	Orange	2.6
12.	1-Octadecane 1-hexadecylamine, citric acid	Hydrothermal synthesis	Dihydrolipoic acid (p)	Yellow	6–8
13.	Citric acid	Hydrothermal treatment	Isoleucine (d)	Violet	6–15
14.	Ammonium citrate	Hydrothermal treatment	Ethylene diamine (d)	Indigo	4.8
15.	Citric acid, ethanediamine	Hydrothermal method	–	Violet	<5
16.	L-Serine, L-cystine	Hydrothermal treatment	N, S (d)	Orange	2.6
17.	Citric acid, GSH	Hydrothermal treatment	–	Blue	2.5–3
18.	1-Octadecane 1-hexadecylamine, citric acid	Hydrothermal synthesis	Dihydrolipoic acid (p)	Yellow	6–8
19.	Citric acid, NaOH	Hydrothermal treatment	–	Green	11.3
20.	Citric acid, NH_3-H_2O	Hydrothermal treatment	N (d)	Blue	2
21.	Folic acid, phosphoric acid	Hydrothermal treatment	Folic acid, phosphoric acid (d)	Indigo	13.2 ± 1.6
22.	Glucose	Hydrothermal treatment	–	Blue	1.65
23.	Sodium nitrate, histidine	Hydrothermal treatment	–	Indigo	1.5
24.	L-Phenylalaninol	Hydrothermal carbonization	–	Violet	2.8
25.	Folic acid, phosphoric acid	Hydrothermal treatment	Folic acid, phosphoric acid (d)	Indigo	13.2 ± 1.6
26.	APTS (3-Aminopropyl)triethoxysilane), Glycerol	Hydrothermal synthesis	–	Violet	9 ± 0.5
27.	Citric acid, PEI (polyethyleneimine)	Hydrothermal treatment	–	Blue	4.5

1.1.3 The Relationship Between the Chemical and Optical Properties of CDs

The discovery of CDs was unintentional. It was discovered by scientists during the purification of carbon nanotubes at the beginning of the 2000s (Xu et al., 2004). The following two decades were full of CD research to understand the nature of these carbon-based nanoparticles. The most exciting result was excitation-dependent emission characteristics of CDs since this is not a common feature of the luminescent quantum dots (QDs), the previous star of that area. One significant drawback is a dramatic decrease of luminescence intensity at longer wavelengths, despite the broad emission spectrum of CDs. Possible causes of such behavior have been suggested as selectivity at the optical level due to the change in the size of nanoparticles, also known as quantum effect or trap states on the surfaces. Briefly, CDs entered the scientific world as nanoparticles with absorption in UV-Visible range and dominant blue emission (Liu et al., 2018).

This is a limitation in terms of biological applications since the penetration depth of blue emissions is relatively short, preventing deep tissue imaging (Mauro et al., 2020). It is also a limitation in sensing and tagging applications where colored substrates or analytes are used (Liu et al., 2018). Besides, this lack of color tunability which is easily achieved with quantum dots excludes CDs from various application areas. Hence, a great

effort towards color tunning of CDs and the development of red-luminescent CDs have started. Red emission with longer penetration depth is highly preferred in bio-applications and tagging of colored materials (Lee et al., 2016). In literature, numerous reports are claiming successful synthesis of red CDs (rCD) case. However, most of the time, they produce CD mixture with emissions in the whole visible range and then separate them using column chromatography (Ding et al., 2015). Therefore, one of the goals of this thesis is the synthesis of color tunable CDs and the synthesis of rCDs without size separation processes.

Based on the literature, there are mainly two parameters affecting the emission color of CDs: *reaction solvent* and *precursor*.

Common precursors for CDs in the literature are citric acid and urea (Simões et al., 2016). They are not aromatic or does not contain conjugated carbon structures. The products synthesized from citric acid and urea require a size separation process to obtain single color luminescent CDs.

Interestingly, the use of malic acid shifted the blue emission of CDs obtained from branched polyethyleneimine (bPEI) to green with high QY (41%) (Guo et al., 2019).

Usually, aromatic molecules are preferred as precursors to produce CDs with emission colors beyond blue and especially red. Aromatic precursors inherently lower the energy bandgap by generating large sp^2 domains and shifting the emission to longer wavelengths (Yan et al., 2019). Therefore, for example, phenylenediamines are one of the most popular precursors for CDs.

Another chemical feature of the desired precursor is the heteroatom content because N, O or S atoms introduce new energy bandgaps within CDs. Nitrogen doping (N-doping) is shown as a red shifter in literature due to the generation of additional states between HOMO and LUMO, which reduces the bandgap (Ding et al., 2020; Wang et al., 2015; Zhang et al., 2014).

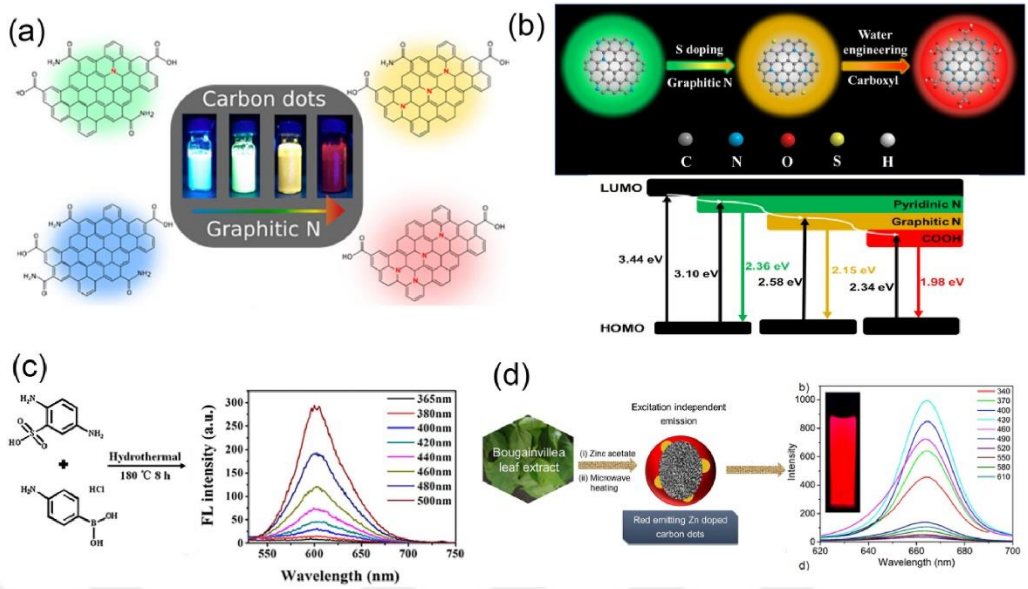

Figure 1.4. Examples of heteroatom doping effect on optical properties of CDs (Ding et al., 2020).

The position of N atoms on the CDs influences the emission wavelength (Zhang et al., 2014). In 2015 and 2017, two different studies show that ortho-phenylenediamine (oPDA) gives green emission in ethanol (EtOH) and dimethylformamide (DMF) (Jiang et al., 2015), respectively, but para-phenylenediamine (pPDA) gives red emission in DMF (Lin et al., 2017). However, rCDs were also synthesized from oPDA by acid treatment, specifically with HNO_3. Acid acted both as catalyst and reactant through electrostatic interaction with the precursor. Eventually, that caused changes in the electronic properties of CDs (Liu et al., 2018). Based on these reports, a highly acidic environment promotes the redshift by improving the carbonization degree and domain size of CDs (Ding et al., 2018).

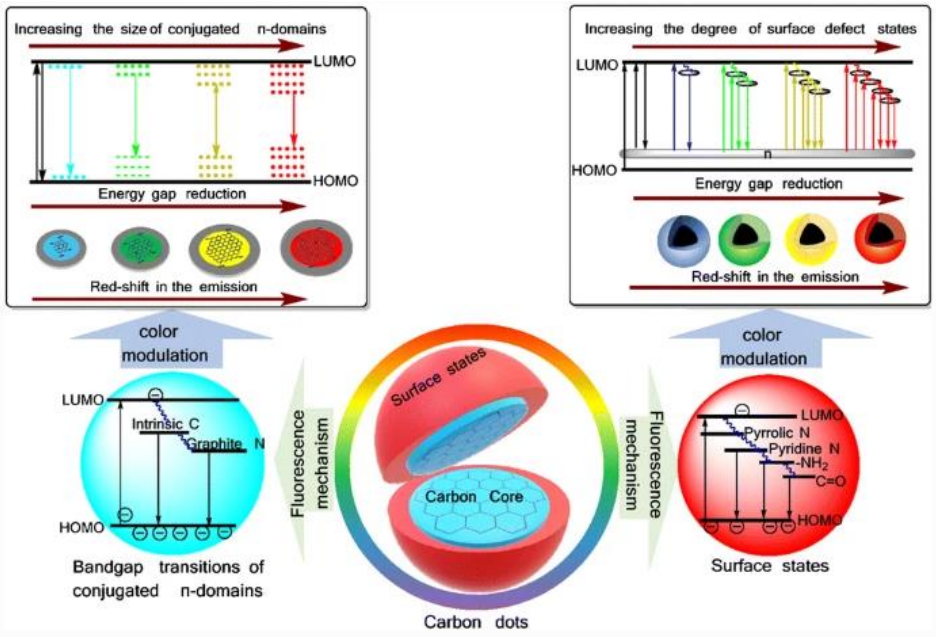

Figure 1.5. Examples of N-doping effect on optical properties of CDs (Yan et al., 2019).

A mixture of precursors with different heteroatoms is also a possible way to tune luminescence color. Dopamine/oPDA mixture in an acidic aqueous medium (pH=3 by addition of HNO_3) produced rCDs. Besides, the two-photon excitation of these CDs provided the red emission, which is an advantage for deep penetration (Lu et al., 2017).

There are some other possible small aromatic structures such as melamine (Pan et al., 2021) and trinitropyrene (TNP) (Bian et al., 2016) which may be also used in the solid-state reactions (Zheng et al., 2020; Ding et al., 2021). Pan et al reported the scalable synthesis of organic soluble orange CDs from TNP in toluene as the preferred solvent (Wu et al., 2017).

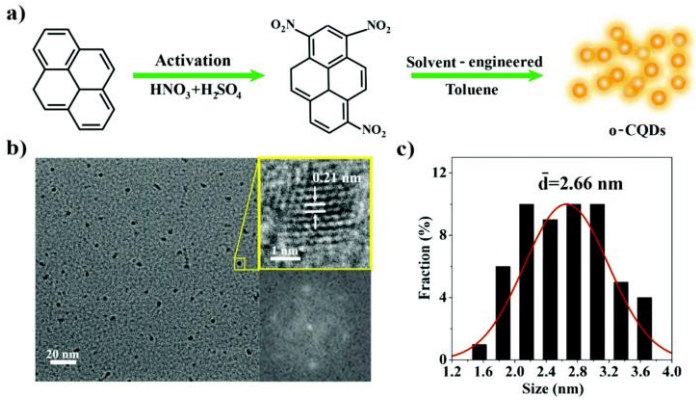

Figure 1.6. a) Synthetic pathway of CDs. b) Corresponding TEM images c) and size distribution histograms (Wu et al., 2017).

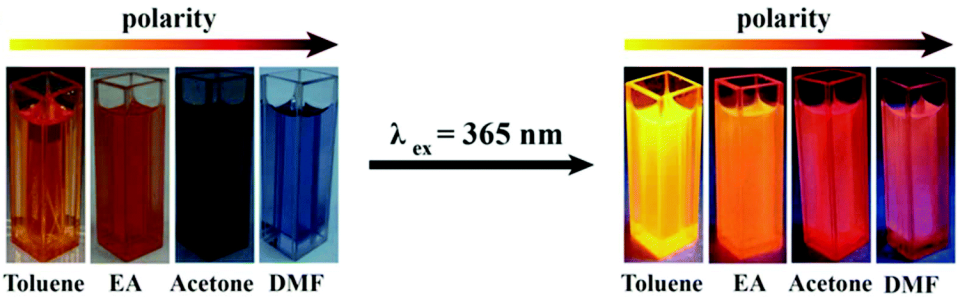

Figure 1.7. Images of CDs in different solvents in daylight and under 365 nm UV irradiation respectively (Wu et al., 2017).

A year later, Geng et al claimed NIR-responsive CDs for photothermal therapy (PTT) from TNP and bPEI precursors (Geng et al., 2018). Although CDs had a wide absorption range in the 600-850 nm region suitable for NIR-phototherapy, they did not have a long wavelength emission. As seen in Figure 1.8.a and 1.8.b. (Geng et al., 2018), the emission maxima was around 480 nm, dominated by bPEI. They suggested that since the absorbed photons at 808 nm are not released in the form of luminescence, they should be in the form of heat; hence these CDs were suitable as photothermal agents.

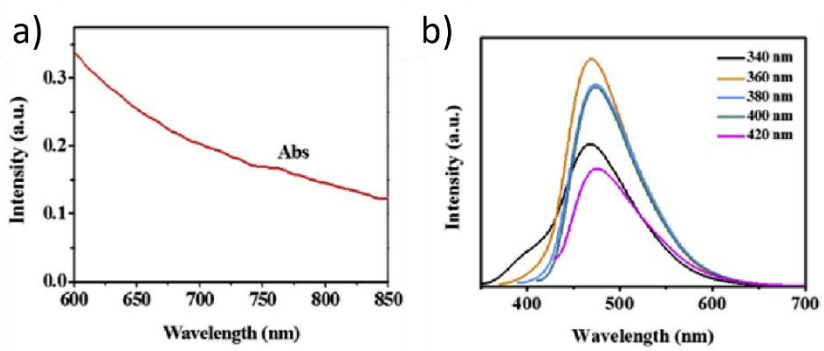

Figure 1.8. a) UV-Visible and b) PL spectra of TNP-BPEI based CD at different excitation wavelengths (Geng et al., 2018).

The selection of solvent is also critical in tuning the emission color of CDs. As shown in Figure 1.7 (Wu et al., 2017), the emission of CDs produced from TNP redshifted with the increasing polarity of the solvent from toluene to ethyl acetate, EA, to acetone and DMF. On the other hand, it was also reported that as the hydrophilicity and polarity of the solvents decreased, N-containing photoluminescence, PL, centers could be formed

easily, thereby leading to an increased red emission of CDs produced from pPDA (Zhang et al., 2017).

Interestingly, the solvent may not be just a reaction medium. Several studies are showing that formamide as a reaction solvent gives better yellow/red emissions than DMF. That means formamide itself or decomposed products take a part in the formation of red-shifted CDs (Ding et al., 2017; Zhu et al., 2019).

As a reaction solvent for CDs, water is a good choice especially for aqueous colloidal CDs because of its safety and convenience. But CDs produced in aqueous solutions usually have blue emission with low intensity (Khan et al., 2020). In addition, the high polarity of water and poor solubility of conjugated carbon precursors seem to prevent red-shifted emissions (Yang et al., 2019).

There is also an interesting phenomenon that is observed with some CDs: the *solvatochromic effect*. As the solvent polarity increases, the dipole moment affects the surface electronic structure more and more, reducing the bandgap and shifting the emission to longer wavelengths (Reckmeier et al., 2016). In 2017, Wang et al. claimed that this direct relationship between solvent polarity and red-shift in emission is valid only for aprotic solvents. In terms of protic solvents, hydrogen bonds form between nitrogen or oxygen atoms on the surface of CDs and hydrogen atoms of protic solvent. Consequently, these hydrogen bonds stabilize the excited states and similar orange-red color emission is observed in all protic solvents such as alcohol and water (Wang et al., 2017).

The solvatochromic effect is also observed when CDs were embedded in solid substrates like polymers. Wang et al produced solid CD/polymer composites by using different types of polymers (PS, PMMA, PVP, PEG and PVA). CD was obtained from pPDA in diphenyl ether. Figure 1.9 shows all CD/polymer composites had dark green to red emissions, which was not excitation dependent. Here, as the polarity of the polymer increased, emission color shifted to longer wavelengths (Wang et al., 2017).

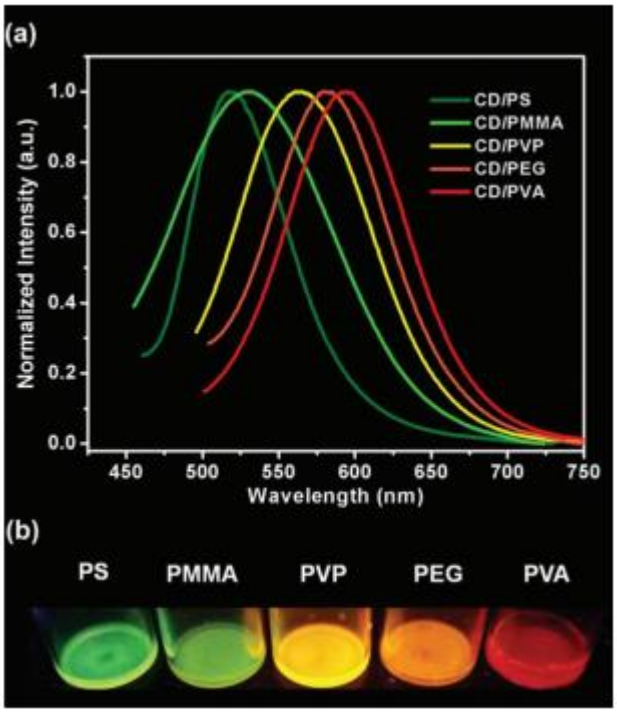

Figure 1.9. a) PL spectra of CD/polymer composites excited at 420 nm b) corresponding photos of these composites (Wang et al., 2017).

On the other hand, there is a different type of CD/PVA composite exhibits *phosphorescence* with a long lifetime (~380ms) as an addition to its fluorescent feature (Deng et al., 2013). Fluorescence disappears immediately when the light source is off; however, phosphorescence lingers as an afterglow process due to energy transition from excited triplet states to the ground state. The study claimed that hydrogen bonding between PVA and CD stabilizes the excited triplet states, promoting phosphorescence. These are highly promising features for using CD/polymer composites in different optical applications.

1.2 Applications

Carbon dots with luminescent properties and lack of toxic heavy atoms are quite popular in medical, environmental and energy applications.

Biomedical applications will be discussed in detail in the following sections, but a couple of highly popular energy-related applications should be given here. CDs became highly popular in the field of photocatalysis in recent years as renewable energy sources became a hot topic for a better, sustainable future. Advanced materials for electrocatalytic

and photoelectrochemical, PEC, hydrogen evolution reaction, HER, is central to the area of renewable energy (Zhang et al., 2013). Dye-sensitized solar cells, DSCs, are also a hot topic in the sustainable energy area. However, the photobleaching of organic dyes or the high cost and toxicity of favored ruthenium containing dyes are some of the limitations. Therefore, people are working on ruthenium or platinum-free systems for PECs. Recent evidence suggests that Ru can be replaced with Fe successfully and that is an excellent solution for the main drawback of expensive and toxic metal components in photoelectrochemical hydrogen evolution reaction (Ulusoy Ghobadi et al., 2018).

Pt-free photoelectrochemical cells have been designed for solar hydrogen generation based on quantum dots with high efficiency (Adhikari et al., 2016). This work is highly encouraging to use CDs instead of CdSe-QDs in photoelectrochemical cells. Thus, not just platinum but also cadmium can be eliminated, and this will be a much more environmentally friendly approach towards renewable energy sources.

However, the world still depends on the petroleum-based energy system, and high demand with limited sources causes the illegal trade of these resources of high economic value. To control the trade and product quality, tagging technology is developed for petroleum-based oils and lubricants.

1.2.1 Fuel Applications

The world economy has laid on the fuel industry for a long time and that dependency affects every living and non-living subject on a daily basis. Debate continues about the best strategies for production and harvesting energy from ideal renewable resources, however, it is undeniable that oil is still the main player. Therefore, while criticizing the drawbacks of petroleum and derivatives, it is also important to understand the fuel industry's historical background and current situation not to create new problems.

Crude oil and natural gas are a mixture of complex chemicals that should be refined for further use. Crude oil consists of different hydrocarbon molecules with different sizes. Each type of hydrocarbon vaporizes at different temperatures depending on their sizes, so crude oil fractions are collected by distillation (Allison & Mandler, 2018).

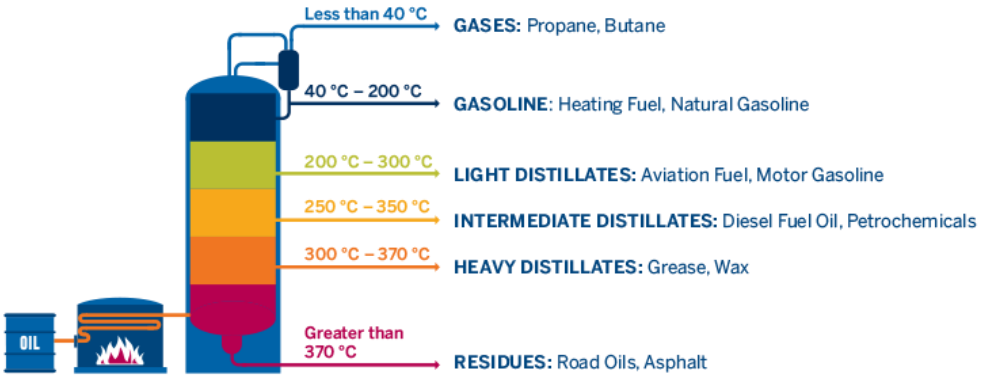

Figure 1.10. Refined product distribution from crude oil. Copyright 2021, CME Group.

Gasoline, also known as petrol, and diesel have the highest percentage in terms of consumption since the automotive industry with fuel oil-based cars creates a huge demand for them. Both are obtained by fractional distillation of crude oil and the only difference is in their hydrocarbon compositions. Gasoline consists of 5-12 carbons, and it has a lower boiling point than diesel which has 10-15 carbons and provides more energy per liter from burning. However, the burning of gasoline is cleaner than diesel. That's why diesel cars require another filtration method in diesel engines. And AdBlue, a diesel exhaust fluid, made with 32.5 % urea and 67.5% deionized water was introduced for this purpose and announced as mandatory to use in diesel engine cars since 2010.

Many problems with oil and derivatives come from fuel additives used to enhance the performance of fuels. Questions have been raised about the safety of using fuel additives for a long time and the most serious mistake was using lead additives in petrol.

Figure 1.11. A sign on a leaded petrol station. Copyright 2013, Wired.

This historical catastrophe started in 1921 with the discovery of tetraethyl lead, TEL, which effectively reduced engine knocking, the characteristic sound created by shock waves in engine cylinders due to unevenly burned fuel and increased the octane rating. The 0-100 scale octane rating system is used to measure octane similarity in the fuel mixture of alkanes depending on their knocking tendency. For instance, unbranched chains like heptane have zero octane rating but 2,2,4-trimethyl pentane has a 100. If the octane rating increases, energy loss due to knocking decreases and eventually, the maximum energy will be obtained from fuel burning. Before that, in the nineteenth-century, ethanol was used as the main fuel source in the first internal combustion engines. Oil won the battle since ethanol is not patentable, which means the petrol and automotive companies will not profit. However, they commercialized the gasoline with lead additive in 1922 and the brand name of this tetraethyl lead, TEL, was Ethyl to hide the negative effect of lead in public.

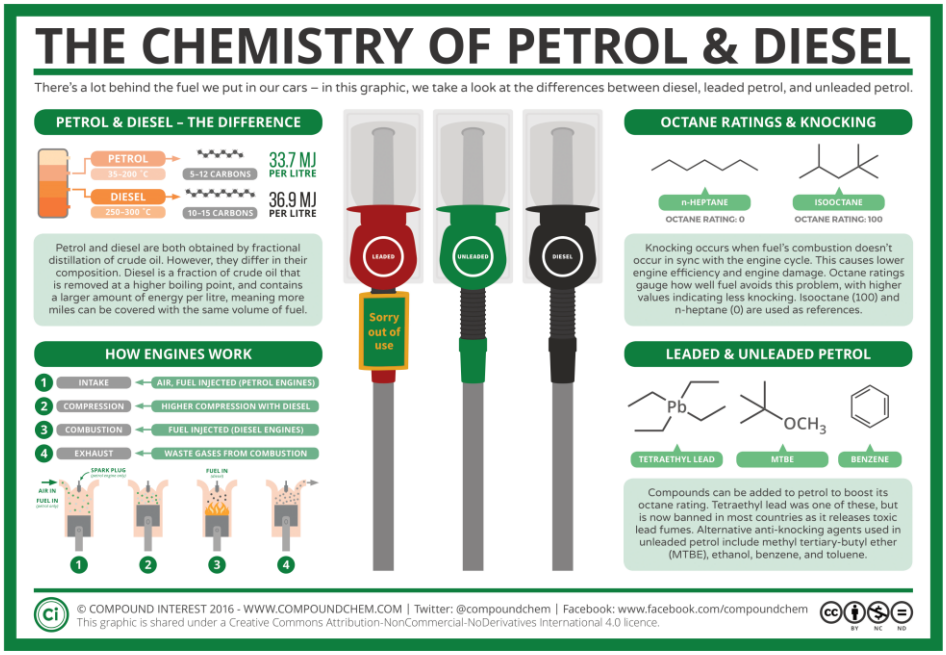

Figure 1.12. An illustration of gasoline and diesel chemistry. Copyright 2016, Compound Interest.

By the 1970s, most petroleum products already contained lead. There have been many attempts to ban lead in oils by showing the public health risks such as loss of intelligence, disruption of behavior and high blood lead levels, putting obstacles in front of independent scientific research delayed its banning.

In 1999, Organization for Economic Cooperation and Development, OECD, organized a meeting with United Nations Environment Programme in Paris. Contamination of air, dust, soil, drinking water, and food crops and the tragic effects of this contamination on public health, especially on children, were reported (Landrigan, 2002).

Although scientific evidence demonstrating the high risks of lead, leaded gasoline could not be completely phase out until the middle of the first decade of the 2000s. Many studies were performed to find new additives as octane rating enhancers. Ferrocene, methylcyclopentadienyl manganese tricarbonyl and copper are common octane examples, however other than health risks, these additives promoted instability of the fuel by catalyzing oxidation reactions (ATC Europe, 2013). Hence, metal-free additives are preferred for future developments.

The addition of dyes into fuel oils is a critical practice. In general, this procedure is performed to classify fuels for different duties, identify the products by UV, IR, or PL spectroscopy due to optical properties of the added dyes and prevent illegal activities such as smuggling. Therefore, fuel oils are colored using azo compounds. Identification requires a heating process of fuel samples to distinguish diesel fuel from higher-taxed diesel fuel (ATC Europe, 2013).

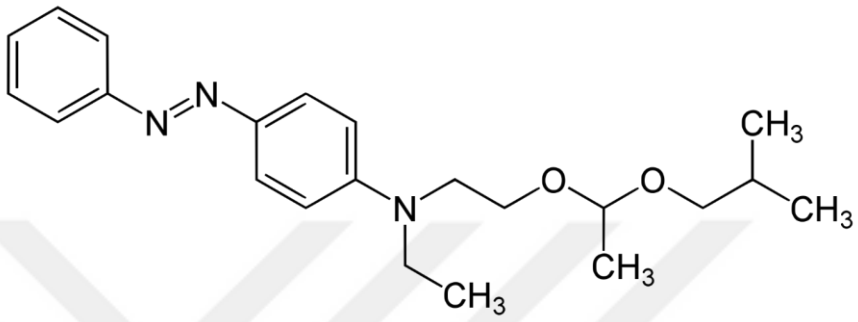

Figure 1.13. A common dye example, Solvent Yellow 124 also known as Euromarker.

In the following years, these kinds of markers had to be replaced by newer technology alternatives, allowing simpler detections with non-destructive analytical methods, such as UV, IR, or PL spectroscopy. In 2020, researchers have developed carbon quantum dots, CQDs, as green tracers in the oil and gas industry (Franco et al., 2020). This is so far the only example of CD tagged oils.

1.2.2 Biomedical Applications

The quality of human life has been increased over the past century. Improvement of medical technologies and supported by scientific research extend the human lifespan. Yet, this encouraged scientists to discover and do even more towards improving the health of individuals and society. One area that has been under heavy research is the utilization of nanotechnology and nanomaterials in medicine to create tools, materials, and models for therapeutic and diagnostic applications. Figure 1.14 shows that nanoscale properties of materials may be exploited in many ways in medicine (Zhao et al., 2015).

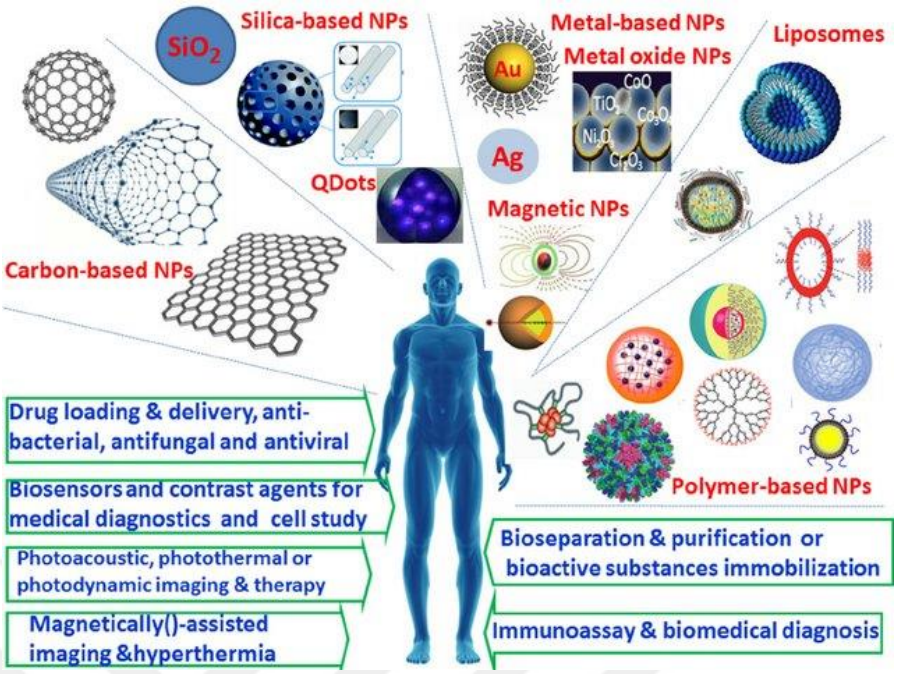

Figure 1.14. Examples of nanoparticles and their biomedical applications (Zhao et al., 2015).

1.2.3 CDs in Biomedical Applications

The majority of the existing studies show that CDs are highly biocompatible however, further investigations are still ongoing and needed (Esfandiari et al., 2019). It was reported that CDs have negligible cytotoxicity at concentrations required for fluorescence bioimaging (Han et al., 2012). The passivation of CDs with functional groups such as PEG, PEI and PAA helped to keep cytotoxicity negligible but enhance fluorescence (Wang et al., 2011). Wang et al. claimed that PEI-functionalized CDs show more cytotoxicity at higher concentrations compared to PEG-functionalized CDs and surface passivation with PAA required a short incubation time to eliminate the cytotoxicity. Liu et al. used a one-step method to obtain PEI-functionalized CDs instead of post-synthetic modification and showed an increase in luminescence intensity which is critical for bioimaging (Liu et al., 2012). Another significant outcome in that study was controlling cytotoxicity by tuning pyrolysis time.

Before 2009, common optical imaging agents were cadmium chalcogenide quantum dots, QDs, which had significant toxicity. This shifted the research towards heavy-metal free and even metal-free quantum dots. At that point, CDs offered several advantages, including lack of metals, better safety profile so far, and the possibility of two-photon excitation which is very attractive for bioimaging (Yang et al., 2009). In 2012, a good

example of fluorescence contrast by using CDs was obtained at an excitation of 595 nm (Tao et al., 2011).

CQD-based fluorescent nucleic acid detection detecting and imaging of mitochondrial H_2O_2 and fluorescence resonance energy transfer, FRET, based detections are a few examples of different uses of CDs in medicine (Li et al., 2011; Du et al., 2013).

Luminescent nanoparticles with large surface area started a new era where scientists can combine imaging and therapy. The use of drug loaded luminescent nanoparticles allows visualization of the nanoparticle and drug distribution and allows monitoring of drugs' effects during therapy (Wang & Hu, 2014). There are few examples of such theranostic nanoparticles based on CDs. For example, conjugation of anticancer drug, oxaliplatin, (oxa (IV)-COOH) to the surface amine groups of CDs, increased the luminescent properties of the CD, improved the biocompatibility and efficacy of the drug (Correa-Baena et al., 2017). The strong bioimaging function and anticancer effects opened a path to personalized medicine where the dose and administration time of the drug may be customized (Zheng et al., 2014).

Table 1.2. The list of common CDs used in PDT and PTT applications (Sharma & Das, 2019).

S. No.	Source molecule	Ligand attached	Targeted cell type
1.	Polythiophene phenylpropionic acid	–	Hela cells
2.	Diaminohexane and carboxylic group of Ce6	Ce6-HA (hyaluronate)	B16F10 melanoma
3.	Acrylic acid, 1, 2-ethylenediamine (EDA) and $Mg(OH)_2$	Mg/N	HepG2
4.	Hydrophobic cyanine dye and poly(ethylene glycol)	–	HepG2, CT26
5.	Citric acid and urea	–	HeLa
6.	Dopamine	–	Hela cells
7.	Urea	Carbon nitride (C_3N_4)	4T1
8.	Citric acid and 5,10,15,20-tetrakis(4-aminophenyl)porphyrin	Cetuximab (C225)	HCC827 and MDA-MB-231 cells
9.	*m*-Phenylenediamine and L-cysteine	Protoporphyrin IX (PpIX)	HeLa
10.	EDTA-2Na and $CuCl_2$	–	Murine melanoma (B16) cells

Nanoparticles may act as a therapeutic agent as well. Magnetic hyperthermia via superparamagnetic iron oxide nanoparticles, SPION, and phototherapies via SPIONs, QDs or metallic nanoparticles such as gold are relatively new and popular in recent years (Yetisgin et al., 2020). There are only a few reports on CD-based photodynamic therapy, PDT, and photothermal therapy, PTT. Ge et al. tried PTT with red-emitting CDs on HeLa cells, but cytotoxicity was a problem (Ge et al., 2015). Li et al. developed CDs from very common reagents, citric acid and urea, and managed to get high PTT efficiency (Li et al., 2016).

1.2.4 Photodynamic and Photothermal Therapy

There have been many deadly diseases in human history, but some of them are already forgotten with the help of science and technology. However, cancer is not one of them since its therapy has never been an easy task due to the complexity of the disease. Every patient experiences this disease in a unique way, which makes the solution complicated in most cases. Therefore, there have been many new drugs, and combination of different therapies such as nuclear medicine, immune therapy, etc. in addition to surgery and chemotherapy. Phototherapy is a relatively new therapeutic modality based on the light-initiated killing of cancer cells.

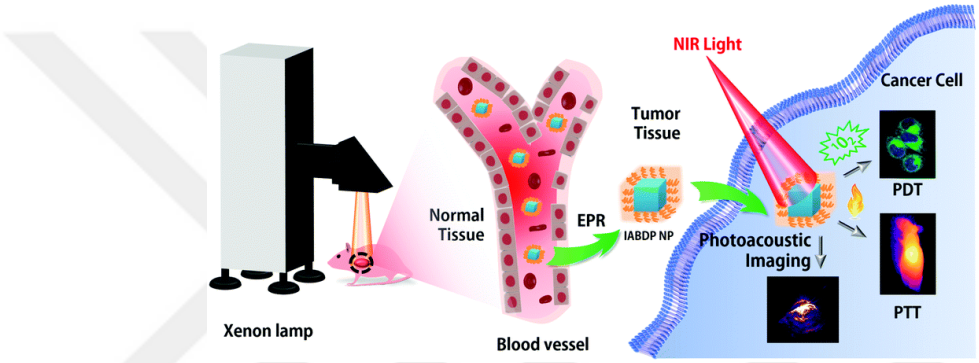

Figure 1.15. Schematic illustration of phototherapy methods (Tang et al., 2017).

Photodynamic therapy, PDT, and photothermal therapy, PTT, are two main classes of light-initiated therapeutical applications. In PDT, specialized molecules called a photosensitizer, PS, is activated by light at a specific wavelength which triggers a series of photochemical reactions (Figure 1.16).

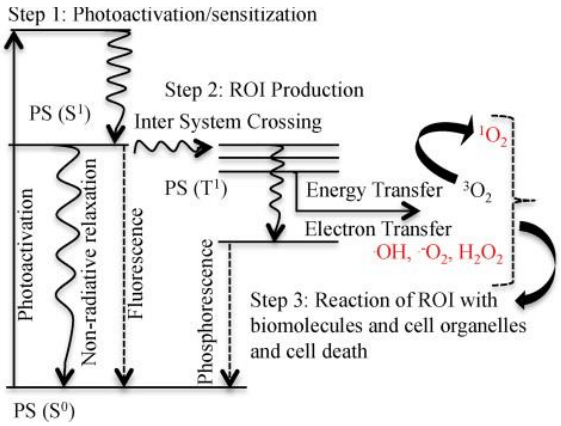

Figure 1.16. Schematic illustration of processes in photodynamic therapy (Shibu et al., 2013).

When light activates the PS, it will be excited to singlet energy state, S^1, and then converted to triplet energy state, T^1, via inter system crossing. A relatively longer lifetime of the T^1 state provides enough time for the activated PS molecule to react with its surroundings, and generally, there are two different pathways for this: Type I and Type II. In the Type I mechanism, electrons are transferred from excited PS to the substrate but in the Type II mechanism, energy transfer happens between excited PS and ground-state molecular oxygen $^3O_2$. From this interaction, reactive oxygen species, ROS, as $^1O_2$ form, and their extremely short lifetime causes a quick reaction of ROS with biomolecules in the tumor cells. The critical point is the localization of PS at the tumor to get maximum efficiency and successful tumor damage through PDT (Shibu et al., 2013).

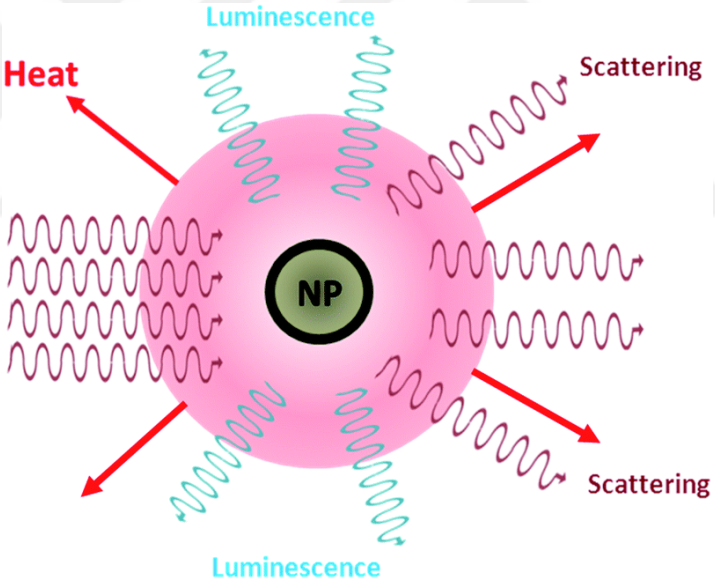

Figure 1.17. Schematic illustration of possible processes after the incident beam (Jaque et al., 2014).

In PTT, absorbed energy by light irradiation of the PS is released as heat during relaxation to the ground state. Figure 1.16 shows other forms to release this energy as fluorescence, phosphorescence, and intersystem crossing as in PDT. This non-radiative relaxation-based heat causes hyperthermia (41-47°C) as seen in Figure 1.18 and vital functions of cells collapse due to denaturation of proteins and disruption of the cell membrane (Jaque et al., 2014).

The common method to apply light for cancer therapy is using lasers at specific wavelengths for the PSs. Laser is localized at the site of interest containing PSs to provide high local therapy. The wavelength of light usually varies between UV, red and NIR, with increasing safety and penetration depth in the clinic (Shibu et al., 2013).

One limitation of PTT is the necessity for high power and necrotic cell death which is preferred less by the doctors (Zhang et al., 2018). PDT, in general, may be conducted at lower irradiation powers and usually triggers apoptotic cell death (Kessel & Oleinick, 2018).

Most PSs used in PDT are organic molecules (Lan et al., 2019) such as porphyrin, phthalocyanine, indocyanine and BODIPY, while some of them offer both PDT and PTT, such as indocyanine green, ICG. In the case of PTT, mostly inorganic nanoparticles such as gold, silver, quantum dots such as Ag2S, SPIONs, etc. are used for sufficient light to heat conversion (Han & Choi, 2021). Of course, nanoparticles may absorb or scatter the incident light and may some luminesce while releasing the absorbed energy as heat (Jaque et al., 2014). Therefore, the best particle design for photothermal therapy is suggested as having a high absorption coefficient and low quantum yield. Consequently, the light to heat conversion efficiency is the key in PTT, whereas in PDT the amount of ROS produced is the key for quality.

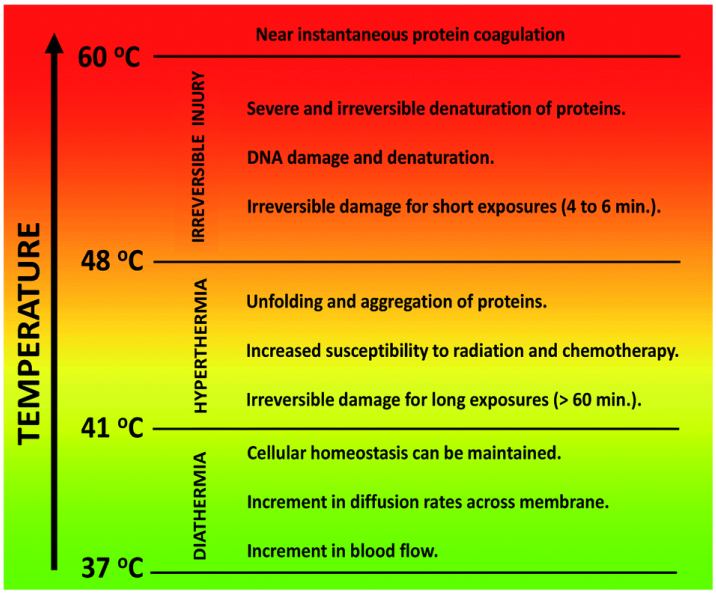

Figure 1.18. Schematic illustration of operating temperatures and their results (Jaque et al. 2014).

1.2.5 SPIONs in Photothermal Therapy

Carbon-based nanoparticles are not the only materials that can be used in biomedical applications. Superparamagnetic iron oxides, SPIONs, are also highly popular in many applications including magnetic resonance imaging, MRI (Harisinghani et al., 2003), drug delivery (Hayashi et al., 2013), magnetic hyperthermia (Alexiou et al., 2000) however have been not known as photothermal agents, PA, for a long time. In 2014, researchers have reported for the first time the photothermal potential of magnetic iron oxide nanoparticles with NIR laser irradiation. The drawback of using iron oxide nanoparticles is the high irradiation requirement to achieve sufficient temperature increase which may be dangerous for healthy tissues (Estelrich & Busquets, 2018).

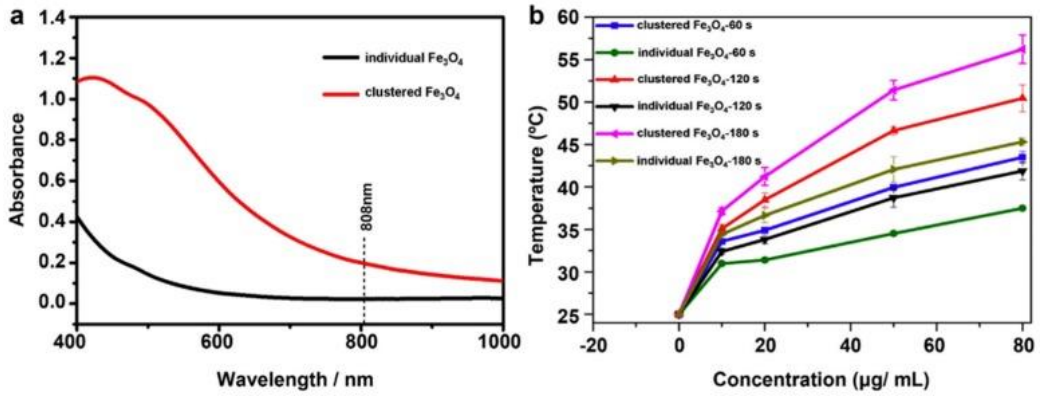

Figure 1.19. a) UV-Visible spectra and b) measured temperature increase after 1-3 min of laser irradiation of aqueous SPIONs with and without the cluster (Shen et al., 2015).

Shen et al. claimed that clustered iron oxide nanoparticles increase PTT efficiency (Shen et al., 2015). They reached to a higher temperature in a shorter NIR irradiation time and with a lower concentration.

Another method to improve the efficiency of iron oxide nanoparticles as photothermal agents is to encapsulate them. Several works are using different coating materials such as polyethyleneimine, PEI, poly(acrylic acid), PAA. The advantage of PEI coating on SPION was reported as better ability to interact with negatively charged DNA due to the cationic character of PEI and that reinforces the death of tumor cells (Steitz et al., 2007; Lungwitz et al., 2005). In 2018, our research group also published an article

and pointed that better stability and lower toxicity can be provided by PAA coating SPIONs (Bilici et al., 2018).

1.2.6 BODIPY in Photodynamic Therapy

Typically, the PDT area is dominated by organic photosensitizers (Figure 1.20). Most of such PSs have significant hydrophobic interactions causing aggregation which reduces solubility, photoactivity and biodistribution. Besides, most of them have very low bioavailability, lack tumor selectivity, and pose significant dark toxicity (Escudero et al., 2021).

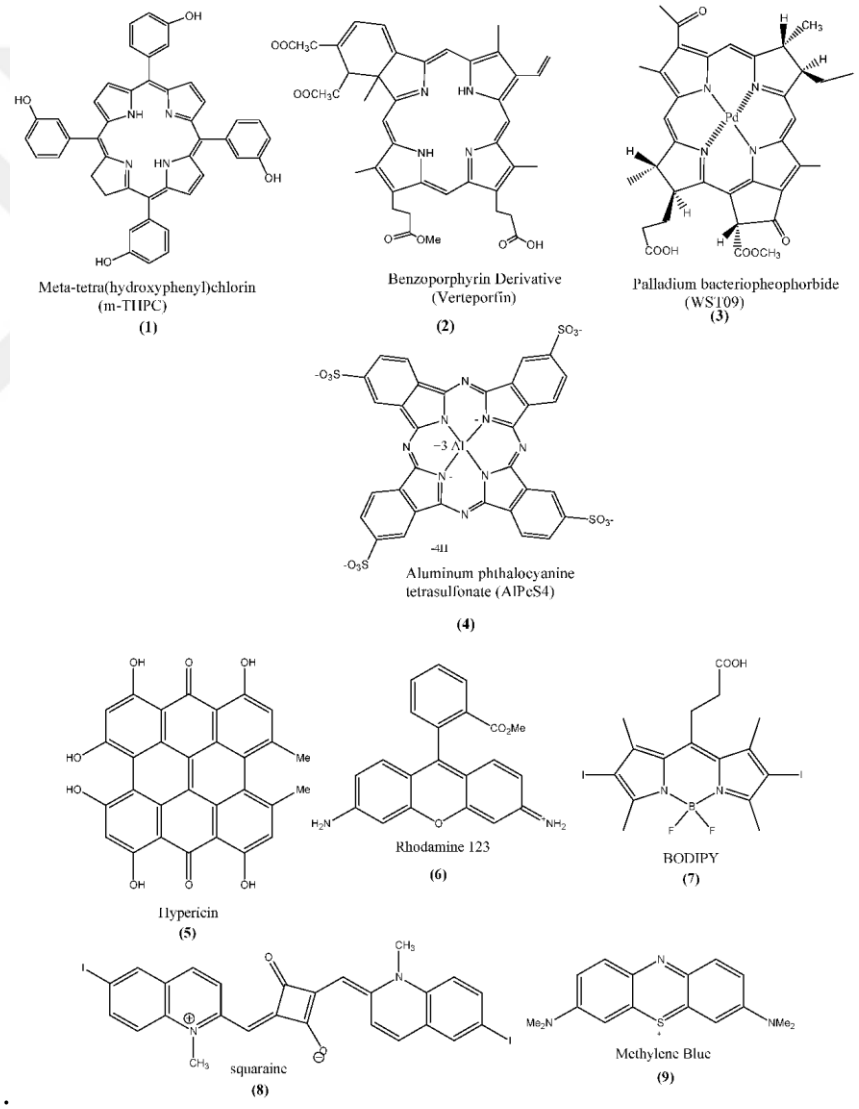

Figure 1.20. Examples of commonly used PSs (Mehraban & Freeman, 2015).

BODIPY dyes have emerged as a new class of PS in the past decade (Kamkaew et al., 2013). It represents a whole class of 4,4-difluoro-4-bora-3a,4a-diaza-s-indacene core-based structures. They have high luminescence efficiency and that causes excited electrons to choose intersystem crossing transitions poorly. Therefore, the number of electrons reach to the triplet state may be too low to produce enough singlet oxygen and that will end up in the low level of ROS production (Escudero et al., 2021). Fortunately, researchers overcame this limitation by adding substituents such as bromine to the BODIPY core at the very beginning of the 2000s (Atilgan et al., 2006). And absorption maxima were reported as 625 nm and 660 nm for these brominated systems. In general, BODIPY is accepted as a successful PS with some disadvantages such as dark toxicity, toxicity to healthy cells and low tumor selectivity (Karaman et al., 2019).

However, at least part of the drawbacks can be solved by using a nanoparticle-based PS delivery system in PDT. In 2014, Ertem et al. claimed that BODIPY functionalized SPIONs have a potential for diagnosis and therapy, but the preliminary study did not include any cell studies for PDT (Ertem et al., 2014).

1.3 The Proposal and the Aim of the Thesis Work

The main motivation behind the development of luminescent CDs is to adapt them into numerous applications since they are metal-free and potentially have high biocompatibility and low toxicity. However, unlike chalcogenides, the color tunning of CDs is not straightforward. Literature suggests heteroatom doping to alter the emission color of CDs. For example, N-doping is suggested to promote red-shift in the emission wavelength of CDs. Despite the fact that most CDs are emitting blue, red CDs and NIR CDs are highly desired for many applications since they hold the advantage of deeper penetration depth in biological applications and less luminescence overlapping in fuel applications. Small organic precursors are usually preferred during the hydrothermal synthesis of CDs. Even though there is some literature on the production of NIR and red QDs as well as a portfolio of colorful CDs with emissions from blue to green, yellow, orange and red, most of them are either non-reproducible or indeed produce all of the CDs in one pot and then subject that to post-synthetic fractionation.

One of the goals of this thesis is to investigate major factors, specifically the aromatic nature of the precursor, N-, O-, P- doping and solvent (polarity and reducing power), on

the production of CDs with different emission colors without any post-synthetic fractionation process.

As described in previous sections, authenticating petroleum products is an important and challenging task. The primary application of CDs in this thesis is the fluorescent tagging of petroleum products with CDs. This requires strong emission, especially at long wavelengths, colloidal and luminescent stability of CDs in petroleum products for at least 1 month. Also, post-synthetic surface treatments with oleylamine to enhance the dispersibility of CDs in hydrophobic petroleum products and enhance the luminescence intensity of CDs is suggested and studied in this thesis. For gasoline and diesel hydrophobic CDs, for AdBlue, aqueous CDs were prepared.

In the second part of this thesis work, photosensitizer loaded SPIONs for enhanced PDT is discussed to kill tumor cells. A derivative of BODIPY was used as a sensitizer that lacks tumor specificity and suffers from instability. In this thesis work, the hypothesis behind combining BODIPY photosensitizer with PAA coated SPION was to enhance the stability of the BODIPY and its tumor accumulation by delivering it specifically to tumor cells by attaching an antibody to nanoparticles specific to tumor cells, i.e. to EGFR.

Lastly, the PDT and PTT potential of aqueous red-emitting CD are investigated to evaluate the potential and blaze a trail for the CDs produced here to take part in phototherapy.

Chapter 2: DEVELOPMENT OF CARBON NANOPARTICLES

2.1 Introduction

Carbon nanoparticles have several features that make them in demand; easy to manufacture, low-cost synthesis and open to tailor of optical properties. Among the nanoparticles, carbon-based ones have been known with excitation dependent emission characteristics. Alteration in emission with the change of excitation wavelength offers a genuine feature to use in applications. However, not all carbon dots have to show excitation dependent emission trends sometimes optical properties may depend on environmental parameters such as pH or having a coating. Nevertheless, their photoluminescence is the focus in terms of applications and literature there are many examples of carbon dots with different colors and high QY (Chahal et al., 2020; Xie et al., 2021), yet still, there is a lack of reproducible, stable, and strongly emitting CDs, especially red-emissive CDs.

2.2 Experimental

2.2.1 Materials

Pyrene (98%), nitric acid (65%), xylene (isomeric mixture), dimethylformamide, melamine, o-phenylenediamine, p-phenylenediamine, branched polyethyleneimine (Mw 2 kDa) were purchased from Sigma (Missouri, U.S.). Sulfuric acid (35%), maleic acid and phosphoric acid were obtained from Merck (Darmstadt, Germany). Pure water (18.2 mΩ, RephiLe Bioscience and Technology, Shanghai, China) was used.

2.2.2 CDs Synthesis

One of the precursors 1,3,6-trinitropyrene (TNP) was not purchased, it was synthesized from pyrene. To do that, pyrene (1.0 g) was dissolved in the prepared acid mixture (75 mL nitric acid (65%) and 25 mL sulfuric acid (30%)) and placed into a 250 mL two neck round bottom flask. The solution was heated to 80°C in an oil bath for 24 hours. After cooling down to room temperature, it was diluted with DI water and filtered

by using a vacuum filtration setup. Eventually, the acid-free yellow colored powder was obtained after drying at 50°C for 2 days.

Table 2.1. Set of synthesis experiments for CDs.

Title of CD	**Source**	**Method**	**Temperature**	**Time**	**Medium**
F10X5	TNP	Hydrothermal	180°C	16 h.	Xylene
F10H5	TNP	Hydrothermal	180°C	16 h.	H2O
CD01	TNP, Melamine	Solid-state	180°C	12 h.	Xylene*
CD01	TNP, Melamine	Solid state	180°C	12 h.	DMF*
CD45	TNP, bPEI (2 kDa)	Hydrothermal	220°C	10 h.	H2O
CD46	TNP, bPEI (2 kDa)	Hydrothermal	220°C	10 h.	Xylene
CD33	Melamine, pPDA	Hydrothermal	200°C	8 h.	DMF
CD43	pPDA	Hydrothermal	200°C	4 h.	DMF
CD44	oPDA	Hydrothermal	200°C	4 h.	DMF
CD07	pPDA	Hydrothermal	180°C	24 h.	H2O, H3PO4
CD24	bPEI (2 kDa), Maleic acid	Hydrothermal	180°C	10 h.	H2O

**Final product was dissolved in defined solvent after solid-state synthesis.*

The common method for hydrothermal synthesis is as follows: firstly, required precursors were dissolved in solvent (aqueous or organic) and then the suspension was transferred into a Teflon-lined autoclave (45 mL) and placed into the oven according to temperature and time recipe in Table 2.1. Obtaining suspensions were filtered 0.22 µm microporous membrane to remove large size clusters and washed with cold EtOH or acetone in a centrifuge tube to remove impurities. The precipitate was the final product.

For CD07, the purification method was a pH-dependent procedure and after the hydrothermal product was filtered using 0.22 µm microporous membrane, the solution was neutralized with 0.1 M NaOH. Afterwards, this suspension was precipitated in the centrifugal tube (5000 rpm, 25 min). The precipitate was washed off with cold EtOH and

distilled water respectively to remove by-products. The final carbon dot was produced by dissolving the precipitate in 0.1 M HCl.

2.2.3 Characterization

UV-Visible spectra were obtained by using a Shimadzu UV-Vis-NIR spectrometer in the 300-1000 nm (altering range among particles). Photoluminescence spectra were measured by using four different instruments as follows: HORIBA Fluoromax, HORIBA FluoroLog-3, Edinburgh Instruments FLS1000 Spectrometer and Agilent Cary Eclipse PL. Quantum yield and lifetime measurements were performed on only HORIBA Fluoromax and Edinburgh Instruments FLS1000 Spectrometer. Hydrodynamic size measurements were completed by using a Malvern Zetasizer Nano ZS. Particle crystallinity was monitored with a transmission electron microscope (JEOL JEM-ARM200CFEG UHR-TEM) and X-Ray diffraction analysis (BRUKER D8 ADVANCE X-ray Diffractometer). Fourier Transform Infrared Spectra was recorded with Thermo Scientific iS10 FT-IR for complementary chemical analysis. Elemental analysis of samples was performed using a Thermo K-alpha X-ray photoelectron spectrometer.

2.3 Results and Discussion

From the literature, using aromatic structure precursor and the organic solvent is known as the best recipe to synthesize red-emitting carbon dots since aromatic structure generates large sp^2 domains in other words better carbonization and accordingly lower the energy bandgaps which are favorable for red emission at longer wavelengths. Additionally, nitrogen, oxygen, phosphorus, and sulfur doping increase the redshift by introducing new energy bandgaps (Zhang et al., 2017). Therefore, the first aim was to fabricate red CDs in both organic and aqueous media. TNP in Figure 2.1 was used as a starting material which is very popular to obtain a red carbon dot in an organic solvent.

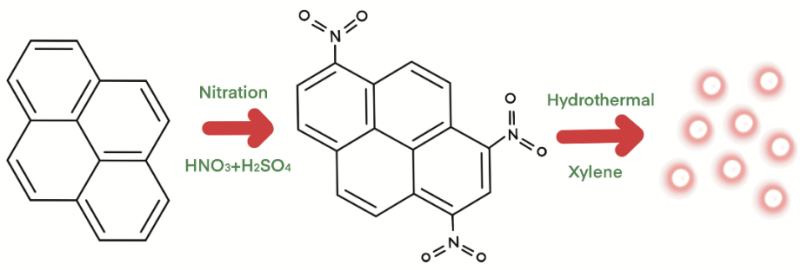

Figure 2.1. Synthetic route for red CD in an organic solvent.

And to understand the solvatochromic feature of it, the following mediums were tested to synthesize carbon dot from TNP structure via hydrothermal method; distilled water, DMF, xylene and addition of melamine in DMF as seen in Figure 2.2.

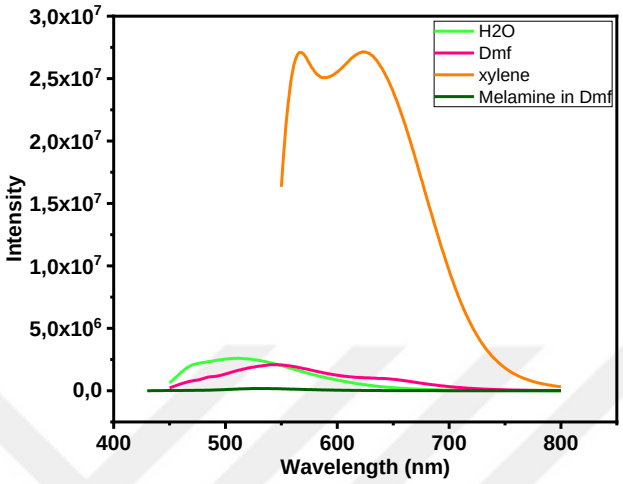

Figure 2.2. PL spectra of TNP based CDs in different solvents.

And results in Figure 2.2 show that TNP in xylene was the most promising particle which is already in the market by Quantag since it is near red-emitting CD. After confirming that xylene is the best environment for TNP, an improvement plan was made for this CD. Since literature shows conjugated structures increase the carbonization and nitrogen doping promotes the redshift, melamine was chosen as the second precursor with its nitrogen-rich and benzene-like ring structure.

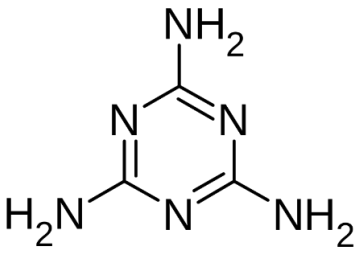

Figure 2.3. Chemical structure of melamine compound (Wikipedia, 2021).

And not only xylene but also DMF was set as experimental media to see the solvent effect on CDs. As the final control experiment, melamine was kept but TNP was

replaced with another popular structure in red carbon dots; para-phenylenediamine, pPDA (Jiang et al., 2015; Lin et al., 2017). Also literature recipe was repeated for a more comprehensive comparison and oPDA in DMF (CD44) turned out green-emitting particle as reported while pPDA in DMF (CD43) is not red but orange.

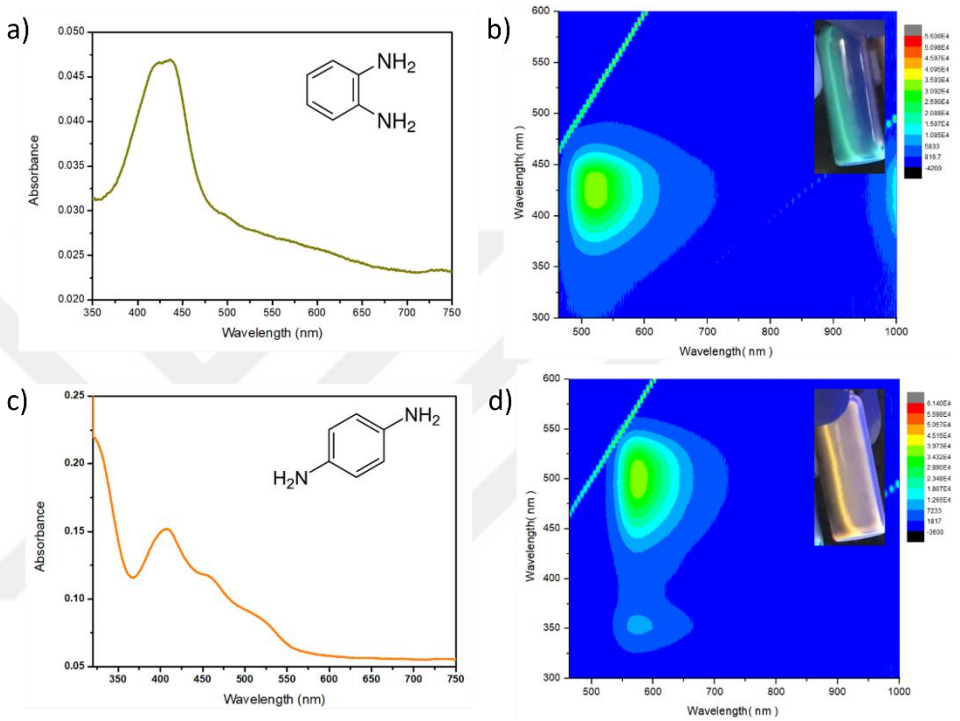

Figure 2.4. a) UV-Visible b) PL spectra of oPDA in DMF and c) UV-Visible d) PL spectra of pPDA in DMF

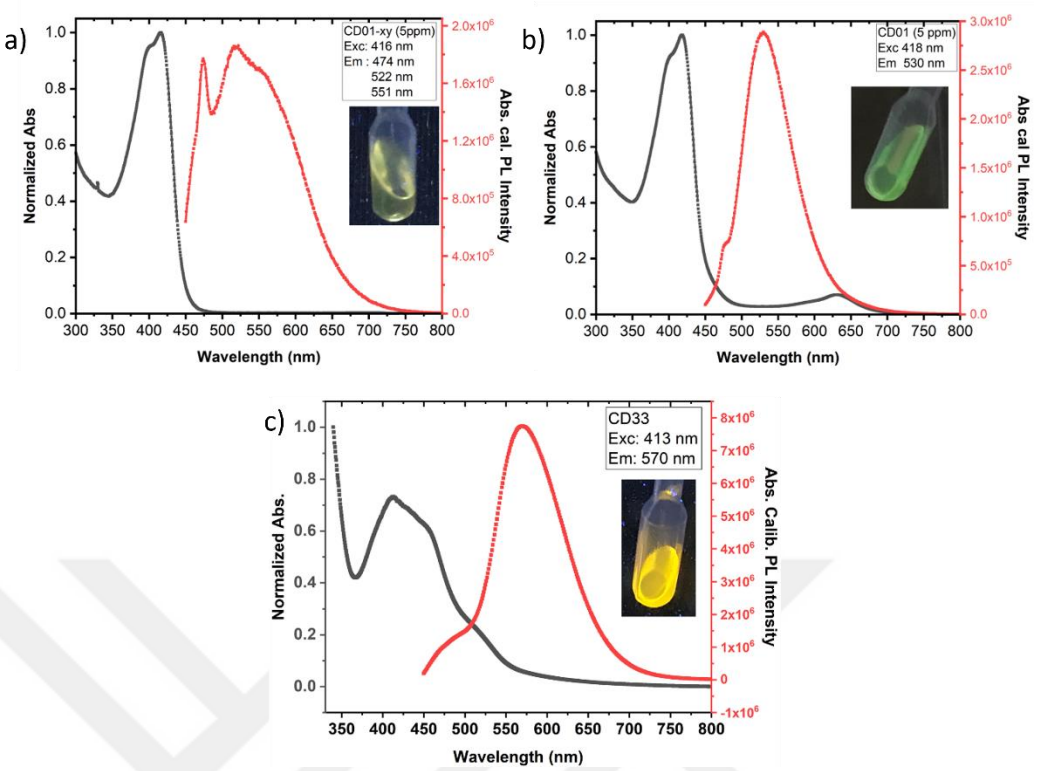

Figure 2.5. UV-Visible and PL spectra of a) CD01X, b) CD01D and c) CD33.

The main lack of red CDs is to fabricate them in aqueous solution since the high polarity of water and poor dispersibility of conjugated precursors discourage producing conjugated PL centers which are responsible for promoting red luminescence. Hence, aqueous CDs have generally blue emission and low intensity. However, in literature there are several studies show that acid treatment can improve the carbonization degree and domain size of CDs (Ding et al., 2018). Another work had strong evidence to show the effect of pPDA and acid treatment combination on red-emitting CD fabrication (Chen et al., 2017). It is also known that different acid structures may cause different color emissions. For instance, malic acid was reported as green CD when it is combined with bPEI (Zhang et al., 2015). Considering literature for aqueous CD fabrication, the set of CD07 and CD24 experiments were planned as seen in Table 2.1.

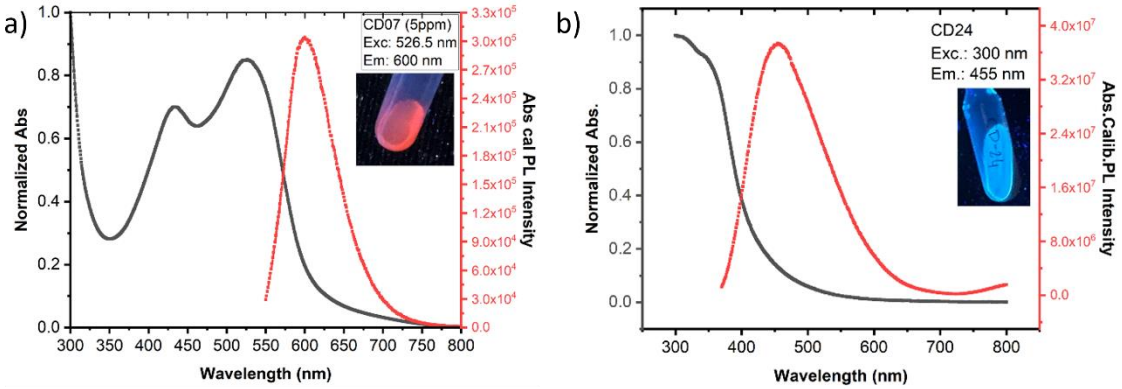

Figure 2.6. UV-Visible and PL spectra of a) CD07 and b) CD24.

In terms of acidity, it is well-known to increase redshift and PL results of CD07 confirmed this phenomenon. This is highly valuable since pPDA is already given red CDs in an organic solvent but successfully fabricating red CDs in aqueous form is another story. In literature, there was a study that used pPDA and different acid mixtures in aqueous media but there was not an example of using them in fuel or biological applications (Chen et al., 2017). In the case of CD24, maleic acid could not over the dominance of bPEI and it ended with cyan color under UV light which is closer to blue not green. The color of bPEI itself gives blue color emitting nanoparticles therefore, it is important to point that acid treatment is not always sufficient by itself but with forceful precursor choices, it would not only act as pH regulator but also may conjugate the final structure.

Furthermore, to understand the effect of changes on designed experiments, some literature recipes were also refabricated, and these are TNP in xylene (F10X5) and TNP in H_2O (F10H5) and TNP + bPEI in H_2O (CD45) in Table 2.1.

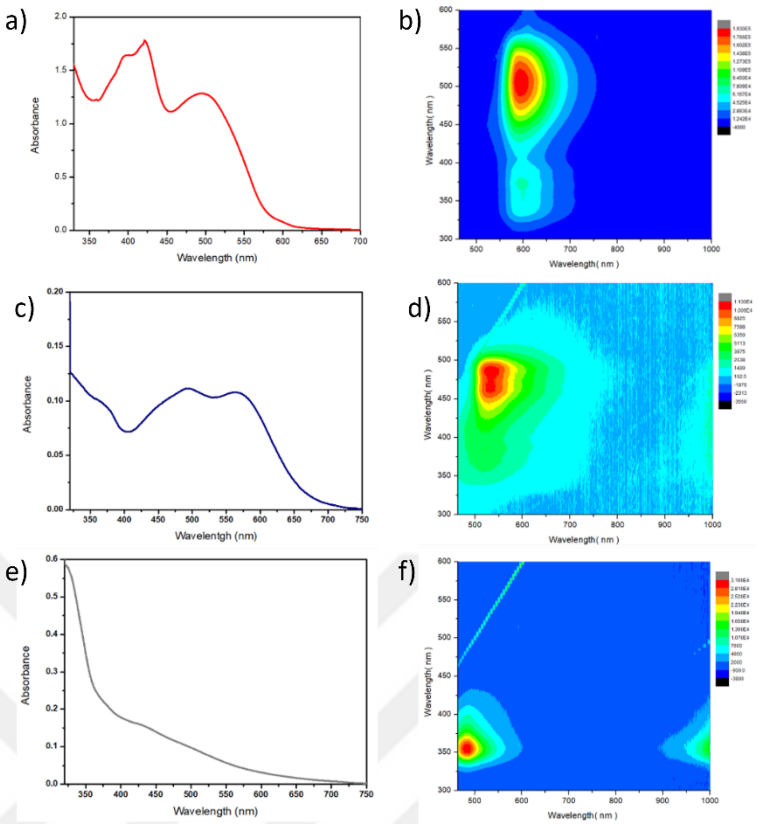

Figure 2.7. a) UV-Visible b) PL spectra of TNP in xylene (F10X5), c) UV-Visible d) PL spectra of TNP in H_2O (F10H5) and e) UV-Visible f) PL spectra of TNP + bPEI in H_2O (CD45).

TNP in xylene has approximately 600 nm emission with a reddish-orange color (Figure 2.9a). When melamine is added to this formula if xylene is a media emitting color shifts to 522 nm and absorption peak at 550 nm will disappear (Figure 2.6a). If the solvent is DMF, the emission bandwidth gets narrow (Figure 2.6b). These two phenomena are both compatible with emission shifts and the absorbance data since the reddish-orange emitting color turns yellow with xylene and green with DMF. Eventually, melamine addition improved the solvatochromic feature of well-known CD recipe and yellow and green color luminescent particles were observed.

Table 2.2. The table of hydrodynamic size and zeta potential for designed CDs.

Title of CD	**Medium**	**Size by number (nm)**	**Size by intensity (nm)**	**Zeta (mV)**	**PDI**
CD01	Xylene	6.522 (±2.169)	28.13 (±20.17)	---	0.309
CD01	DMF	6.092 (±1.799)	275.0 (±174.0)	---	0.406
CD33	DMF	232.1 (±56.58)	259.2 (±57.57)	---	0.602
CD07	H_2O	59.46 (±17.83)	115.5 (±48.36)	31.2 (±1.19)	0.526
CD24	H_2O	292.4 (±108.4)	393.1 (±138.5)	31.8 (±2.20)	0.772

After initial optical experiments were performed, CD01 in xylene and CD07 in H_2O were chosen as the best candidates for further applications. Specifically, DMF was not miscible with diesel and organic CD should be miscible with both gasoline and diesel therefore CD01 in DMF and CD33 could not fit into this. On the other hand, in terms of aqueous CDs, CD24 was not completely useless but CD07 with reddish color has strong advantages in biological applications and that was the reason for choosing it. Furthermore, in the next chapter CD24 will be shown also in the usage of barcode experiments and tagging AdBlue.

The particle size of CDs was ranging from 6 to 400 nm and higher than 100 nm would not be nanoparticle anymore. Hence, chosen two CDs were; CD01 in xylene with 6.522 nm size by number and CD07 in H_2O with 59.46 nm as seen in Table *2.2*.

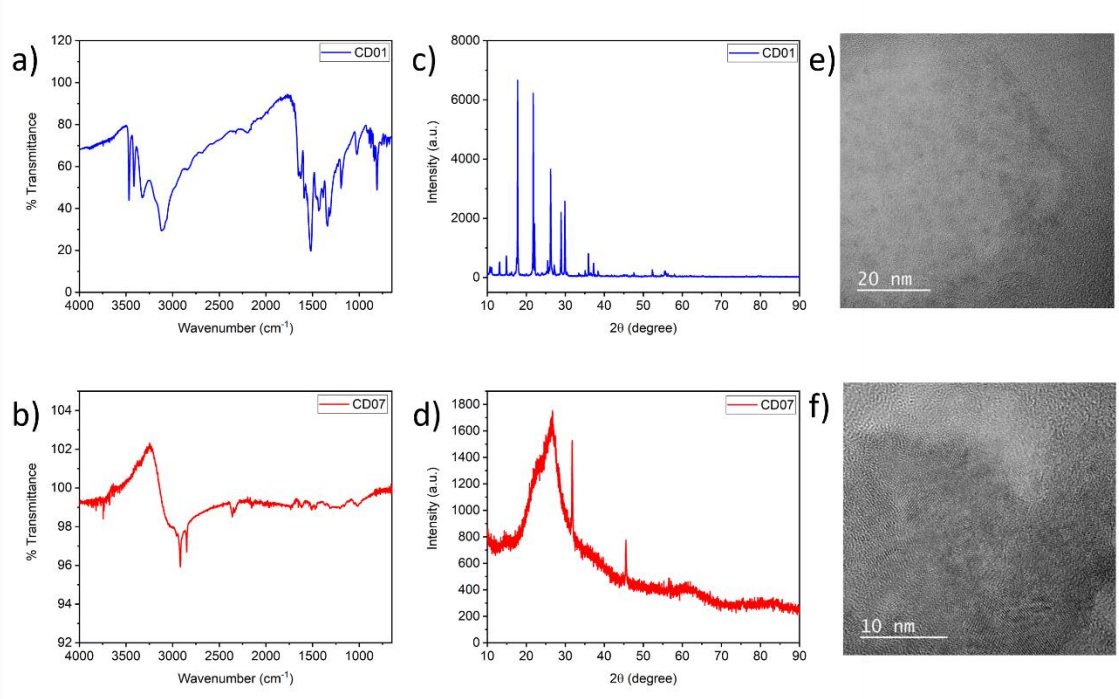

Figure 2.8. FTIR results of a) CD01 b) CD07, XRD spectra of c) CD01 d) CD07 and TEM images of e) CD01 f) CD07

The structures of the best two carbon dots CD01 (organic), CD07 (aqueous) were characterized by FTIR, XRD and TEM instruments. Figure 2.8. FTIR results of a) CD01 b) CD07, XRD spectra of c) CD01 d) CD07 and TEM images of e) CD01 f) CD07a shows the FTIR spectra of CD01 which shows bands centered at 1193 cm^{-1}, 1341 cm^{-1}, 1433 cm^{-1}, 1521 cm^{-1}, 3122 cm^{-1}, 3325 cm^{-1}, 3416 cm^{-1} and 3468 cm^{-1}. The bands centered at 3416 cm^{-1} is assigned to stretching vibrations of O-H, at 3468 cm^{-1} is N-H (primary amine), and at 3325 cm^{-1} is N-H (secondary amine). The bands at 1193 cm^{-1}, 1341 cm^{-1}, 1433 cm^{-1}, 1521 cm^{-1} correspond to the vibrations of C-N, C-H, O-H and N-O respectively. These results indicated that nitro and amine groups from precursors contributed to both surface groups and graphitic structures of CD01. In Figure 2.8.b, the bands centered at 1473 cm^{-1}, 1509 cm^{-1}, 1617 cm^{-1}, 2360 cm^{-1}, 2848 cm^{-1} and 2917 cm^{-1} correspond to the vibrations of C-H, N-O, C=C, CO_2 and C-H which confirmed amine groups from phenylenediamine and hydroxy groups phosphoric acid involved the structure of CDs.

In XRD results, the peak at 2θ~20°-25° corresponds to graphitic carbon with (002) diffraction planes which are by the characteristic structure of inter-layer packing (Shang et al., 2018). TEM images show that CD01 has an amorphous structure and CD07 has a

polycrystalline structure with an 8.7 nm diameter cluster of 1-2 nm diameter crystals, 3.8 nm diameter isolated crystals in Figure 2.10.

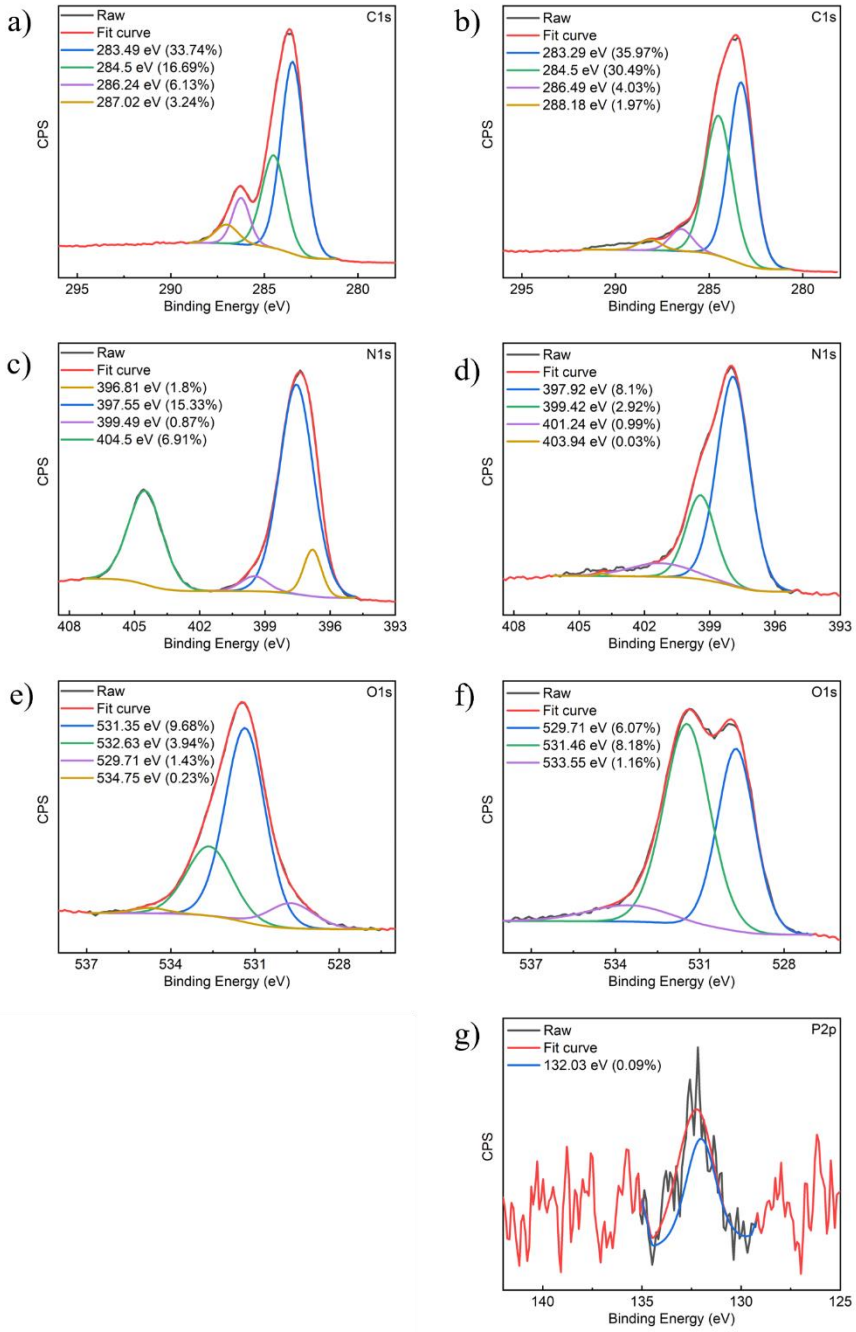

Figure 2.9. XPS results of CD01 for a) C1s c) N1s e) O1s and CD07 for b) C1s d) N1s f) O1s g) P2p

Figure 2.11 shows the elemental analysis of CD01 and CD07. According to XPS results, C1s spectrum of CD01 displays four distinct peaks at 283.49 eV (C=C), 284.5 eV

(C-C), 286.24 eV (C-N) and 287.02 eV (C-O, C=O, CNO), N1s spectrum of CD01 have four peaks at 396.81 eV, 397.55 eV (pyridinic N), 399.49 eV (C-N-C) and 404.5 eV (NO_2), O1s spectrum reveals four peaks at 529.71 eV, 531.35 eV (C=O), 532.63 eV (C-OH/C-O-C) and 534.75 eV (NO_2). These are compatible with FTIR results which show nitro and amine groups involve in the surface and graphitic structures of CD01. In C1s spectrum of CD07, there are four distinct peaks at 283.29 eV (C=C), 284.5 eV (C-C), 286.49 eV (C-N) and 288.18 eV (C-O, C=O, CNO), N1s spectrum of CD01 have four peaks at 397.92 eV (pyridinic N), 399.42 eV (C-N-C), 401.24 eV (pyrrolic N) and 403.94 eV (NO_2), O1s spectrum reveals three peaks at 529.71 eV, 531.46 eV (C=O) and 533.55 eV (C-OH/C-O-C), P2p spectrum shows single peak at 132.03 with 0.09%. Although the percentage of P is low in elemental level, still it provides evidence for involving phosphoric acid in the structure of CD07 besides arranging the acidity of the medium.

Table 2.3. Quantum yield results of designed CDs.

Title of CD	**Medium**	**Quantum Yield (%)**	**Excitation (nm)**	**Scanning Range (nm)**
CD01	Xylene	19.3	460	470-800
CD01	DMF	38.5	460	470-700
CD33	DMF	11.03	520	530-680
CD07	H2O	3.11	526	570-800
CD24	H2O	1.19	300	400-550

Quantum yield experiments were performed at the corresponding excitation wavelength, which gives the highest CDs emission. According to results, maximum QY belongs to CD01 in DMF but CD01 in xylene has still quite high QY. And relatively low QY of CD07 may have a sign for the photothermal potential of this particle since energy is not released as light, it would be released as heat.

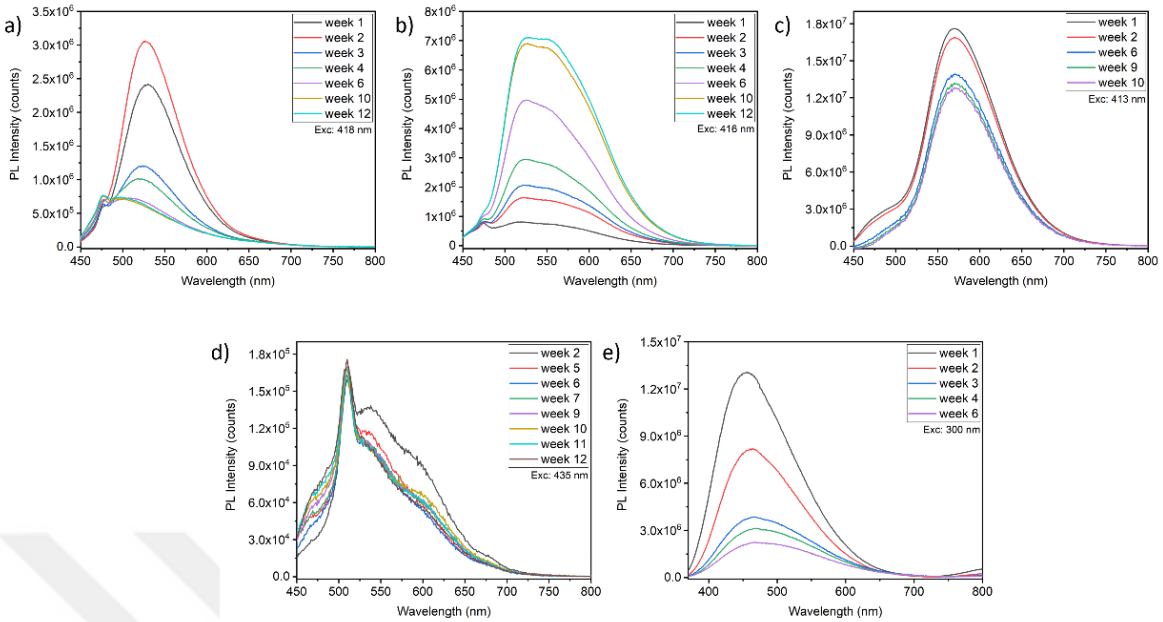

Figure 2.10. Weekly PL stability results of a) CD01 in DMF b) CD01 in xylene c) CD33 d) CD07 e) CD24

In many applications, stability is one of the major drawbacks and more stable particles are always required. In Figure 2.12, CD01 in DMF and xylene reached their plato in week 12 but interestingly PL intensity of CD01 in xylene (CD01X) increases while CD01 in DMF decreases. CD33 and CD07 reach their plato in week 9 and CD24 have close to it in week 6.

2.4 Conclusion

The possible ways to obtain red CDs or near-infrared emissive CDs are listed in general as 1) heteroatom effect like nitrogen doping 2) right precursor and solvent selection 3) increase in the acidity of aqueous solutions. Regarding rCDs, N-rich precursors or solvent choices did not help redshift and partially excitation dependent and photostable particles were produced. The highest QY achieved was 38.5% which belongs to CD01 in DMF. It provides strong evidence that DMF is not just a solvent but also involved in the reaction. The highest PL intensity was achieved by CD01 in xylene and its intensity kept increasing until week 12. Most importantly, difficult task of aqueous rCD synthesis was achieved. This was a major step to investigate the CDs in phototherapeutic applications.

Chapter 3:
INVESTIGATION OF CARBON NANOPARTICLES AS TAGGING MATERIAL FOR FUEL APPLICATIONS

3.1 Introduction

Working in nanosize is a great tool to create easily dispersible nanoparticles in organic and aqueous solvents. With one of the bottom-up methods, hydrothermal synthesis makes it possible to fabricate hydrophilic and hydrophobic nanoparticles. This development is significantly important for the oil industry since the usage of nano-additives in engine systems increases gradually. There are several purposes to use them such as reducing the friction and wear, marking fuel oils, etc. (Shang et al., 2018).

In this chapter, nitrogen-rich carbon dot, CD01 and its derivatives will be shown as colloidally stable and strong particles at least for three months. Concerning these features, the potential of them as tagging material in fuel oils (gasoline, diesel) and AdBlue will be discussed.

3.2 Experimental

3.2.1 Materials

Oleylamine (OA) was purchased from Sigma (Missouri, U.S.). And gasoline, diesel and AdBlue were provided by Quantag.

3.2.2 Synthesis

CDs in this chapter were synthesized according to the given recipe in Table 2.1. The derivatives of CD01 were obtained as follows; CD01OAX was obtained by addition of 750 µL of OA to 1 mg prefabricated CD01 and dissolved them in 2 mL xylene. For CD01AOAX, firstly CD01 was annealed under air with 200°C, 1 h. And then 750 µL of OA was added into 1 mg of obtained powder and dissolved in 2 mL xylene. Similarly, for CD01AArOAX, firstly CD01 was annealed under argon with 200°C, 1 h. And then 750 µL of OA was added into 1 mg of obtained powder and dissolved in 2 mL xylene.

3.2.3 Characterization

UV-Visible spectra were obtained by using a Shimadzu UV-Vis-NIR spectrometer in the 300-1000 nm (altering range among particles). Photoluminescence spectra were measured by using four different instruments as follows: HORIBA Fluoromax, HORIBA FluoroLog-3, Edinburgh Instruments FLS1000 Spectrometer and Agilent Cary Eclipse PL. Quantum yield and lifetime measurements were performed on only HORIBA Fluoromax and Edinburgh Instruments FLS1000 Spectrometer. Hydrodynamic size measurements were completed by using a Malvern Zetasizer Nano ZS. Particle crystallinity was monitored with a transmission electron microscope (JEOL JEM-ARM200CFEG UHR-TEM) and X-Ray diffraction analysis (BRUKER D8 ADVANCE X-ray Diffractometer). Fourier Transform Infrared Spectra was recorded with Thermo Scientific iS10 FT-IR for complementary chemical analysis. Elemental analysis of samples was performed using a Thermo K-alpha X-ray photoelectron spectrometer.

3.3 Results and Discussion

3.3.1 CDs in Gasoline and Diesel

In Chapter 2, CD33 was mentioned as a not ideal choice for fuel applications since it is immiscible with diesel. However, it is still important to demonstrate how different CDs act as tagging material. In Figure 3.1, excitation independent CD33 is shown in gasoline in terms of PL intensity and ΔPL was 46.15% at 510 nm excitation wavelength. The reason to choose 510 or 520 nm is this wavelength is the longest wavelength which CDs have still strong luminescence intensity, but gasoline gets weaker. Therefore, these wavelengths are ideal to eliminate to luminescence overlap between gasoline and CD and define ΔPL. Although 46.15% ΔPL was quite high, CD33 was not colloidally stable in gasoline, there were some precipitates after a month.

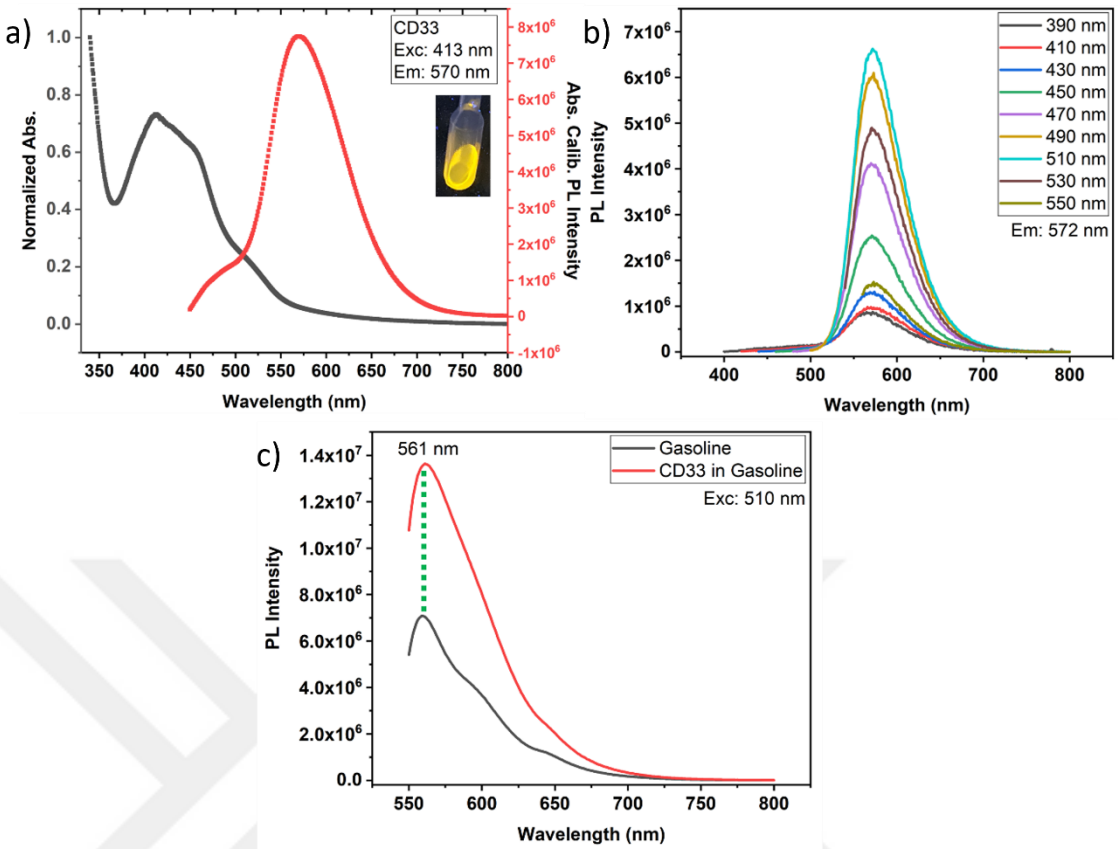

Figure 3.1. a) UV-Visible and PL spectra b) excitation dependent emission spectra of CD33 c) PL intensity comparison of CD33 and gasoline at 510 nm excitation.

Since gasoline and diesel are luminescent particles themselves, it is hard to escape their emission range. If near-infrared (NIR) nanoparticles are made, it would be an ideal scenario but to produce NIR-CDs have not been successfully managed so far. The second way is to compare PL intensities between the nanoparticle and fuel oil. By using ΔPL information, CDs may serve as fuel tagging material. In Figure 3.2, it is shown that CD01X have a highly wide range of luminescence and despite some overlapping with gasoline, there is 61.90% ΔPL at 510 nm excitation wavelength. And it is colloidally stable until week 25 in gasoline and diesel mediums but luminescence in the range of 550-650 nm increases in time because of the time-dependent PL increase feature of CD01X as seen in Figure 3.3.

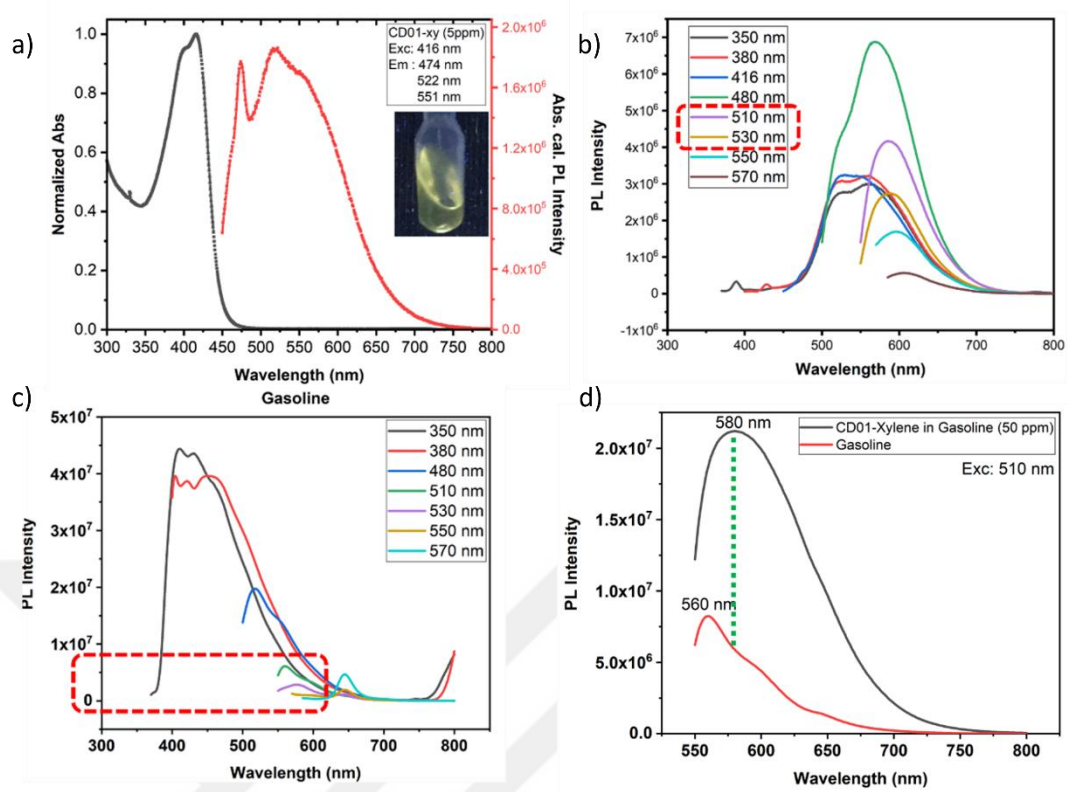

Figure 3.2. a) UV-Visible and PL spectra of CD01X, excitation dependent emission spectra of b) CD01X c) gasoline, d) PL emission comparison of CD01X and gasoline at 510 nm excitation.

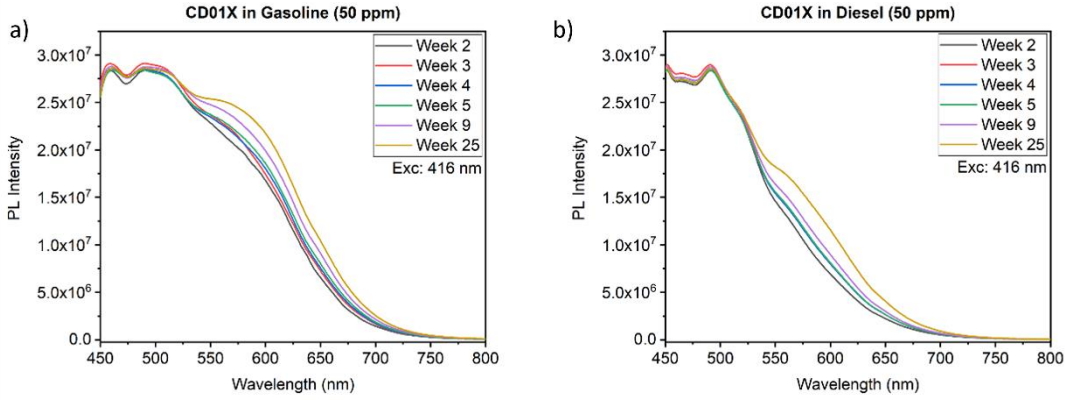

Figure 3.3. PL stability spectra of CD01X in a) gasoline b) diesel.

Since CD01 is a bare core nanoparticle, it has many surface functional groups and they play a role to disperse CD in both polar and nonpolar mediums. There was a study to show that adding Oleylamine to hydrophilic CDs and making them hydrophobic increases the dispersibility in synthetic base oils (Shang et al., 2018).

Oleylamine addition had no dramatic effect on dispersion in xylene, but it causes to emission maxima shift from 580 nm (CD01X) to 630 nm. This redshift is a big advantage for marker purposes since higher wavelength maxima reduce the overlapping area in the PL curve. Despite that dispersion in xylene has not changed significantly, gasoline dispersibility has increased. In gasoline 630 nm could not be preserved and emission maxima shifted to 605 nm. The reason for this shift in gasoline would be the solvatochromic effect of CDs due to bare core structures and since the excess medium was not xylene anymore, gasoline affects more strongly. However, when benchmark (F10X5) is compared in gasoline, it gives lower wavelength emission (595 nm) with higher excitation wavelength (525 nm) and that is not a favorable relationship. Therefore, CD01OAX has a still significant advantage over F10X5 in gasoline with 92.7% ΔPL at 520 nm excitation wavelength as seen in Figure 3.4.

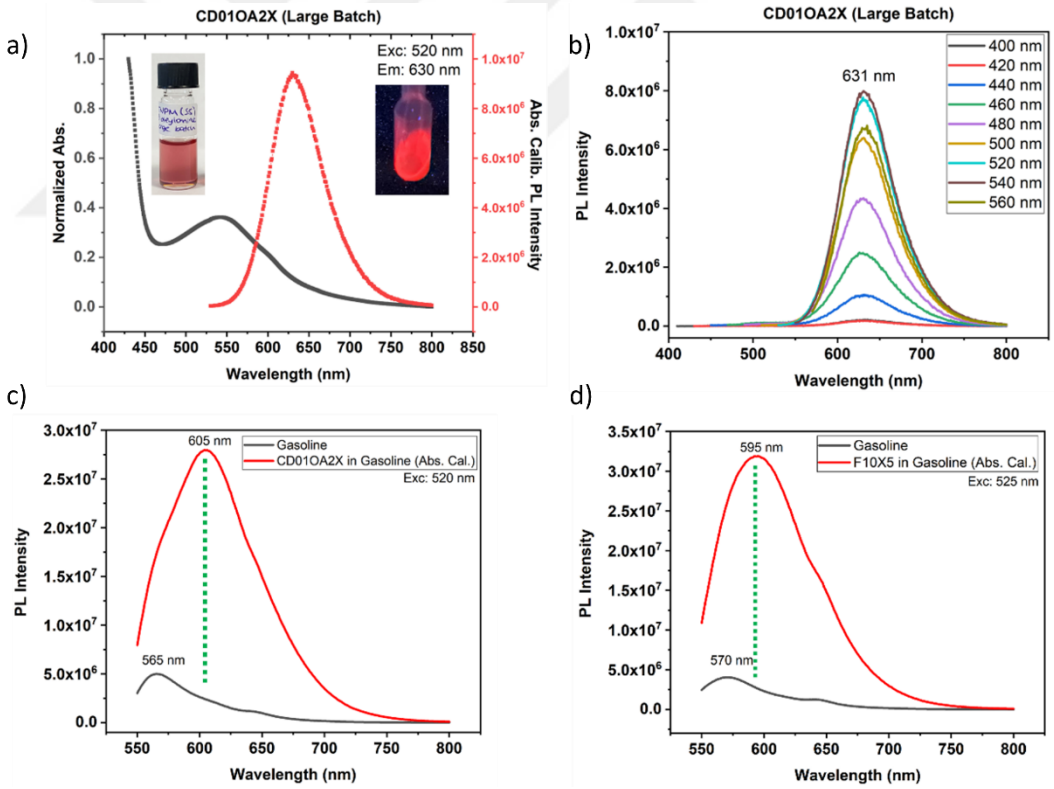

Figure 3.4. a) UV-Visible and PL spectra b) excitation dependent emission spectra of CD01OAX, c) PL emission comparison of CD01OAX with gasoline at 520 nm excitation and d) same comparison of the benchmark with gasoline at 525 nm excitation.

Another advantage of CD01OAX over the benchmark is that CD01OAX is working strongly better in diesel. Figure 3.5 shows that the benchmark has 37.5 % ΔPL at 525 nm excitation wavelength while CD01OAX has 61.5 %.

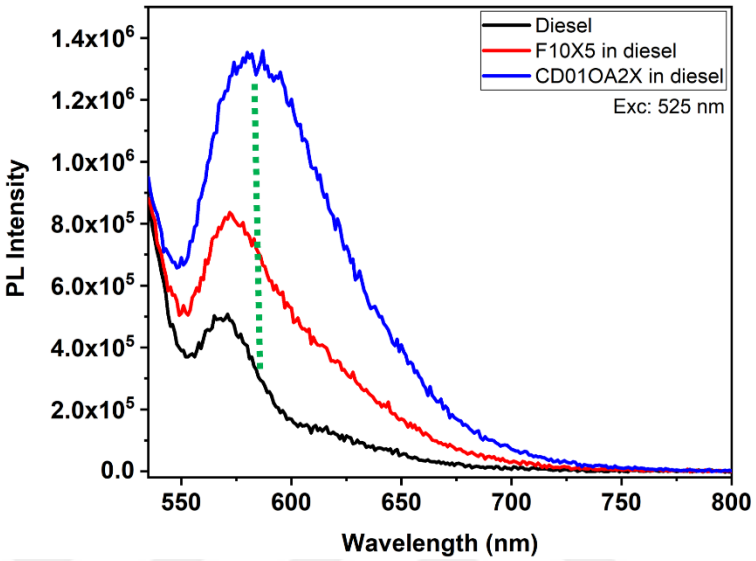

Figure 3.5. PL emission comparison of CD01OAX and benchmark in diesel.

The drawback of CD01OAX is stability in gasoline. Even though PL intensity keeps increasing in nine weeks, when it is put in gasoline, PL luminescence reduced 50% after nine weeks as seen in Figure 3.6.

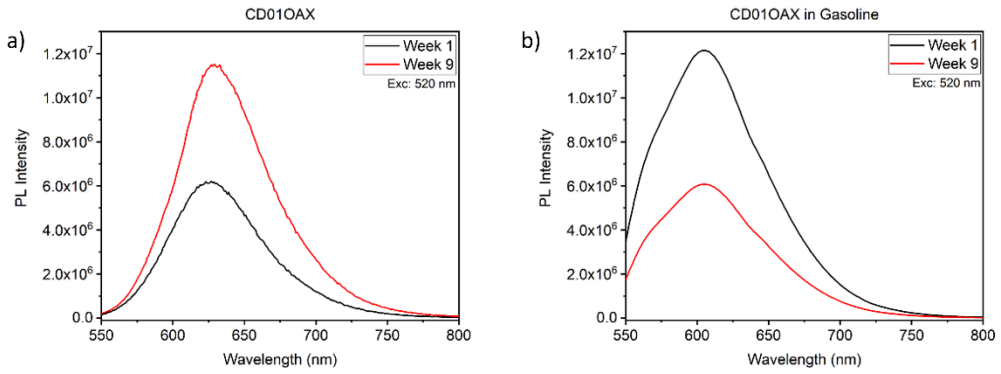

Figure 3.6. PL stability results of a) CD01OAX and b) in gasoline.

Annealing is a method for increasing carbonization and making the nanoparticles more colloidally stable. Scientists claim that with an increase of carbonization, electron transfer will have less loss, concerning that luminescence will increase (Lee et al., 2021).

Annealing under air with 200°C for an hour had a dramatic effect on luminescence in xylene; CD01AOAX. At day zero, 630 nm emission of CD01OAX shifts to 747 nm which is near-infrared region and gasoline has almost zero luminescence at that region. However, this shift was not stable, and it went back to 633 nm after a month. Since it shifted to 633 nm, it gave only 609 nm emission at 520 nm excitation when put CD01AOAX into gasoline. And Figure 3.7 shows that 75.0% ΔPL at 520 nm excitation wavelength which was lower than CD01OAX.

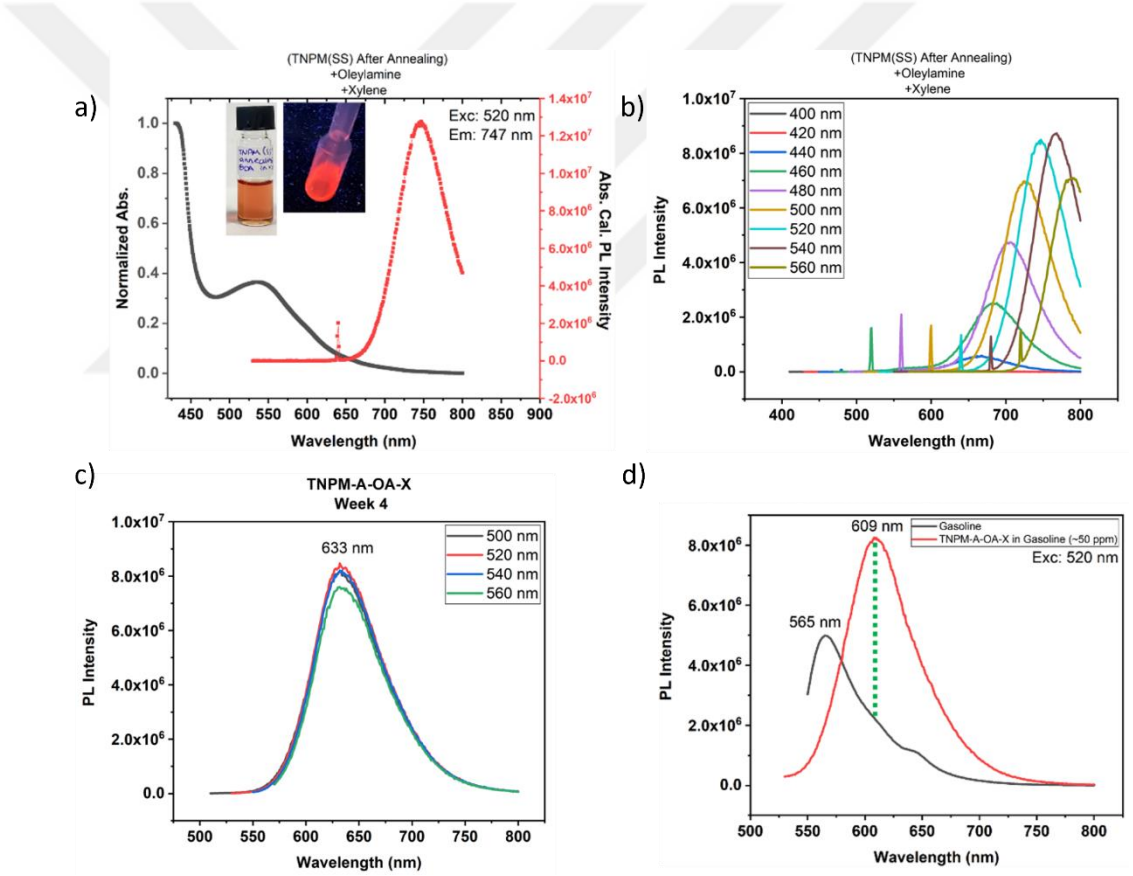

Figure 3.7. a) UV-Visible and PL spectra b) excitation dependent PL emission spectra at day zero of CD01AOAX, c) PL emission of CD01AOAX after a month d) PL emission comparison with gasoline at 520 nm excitation of CD01AOAX.

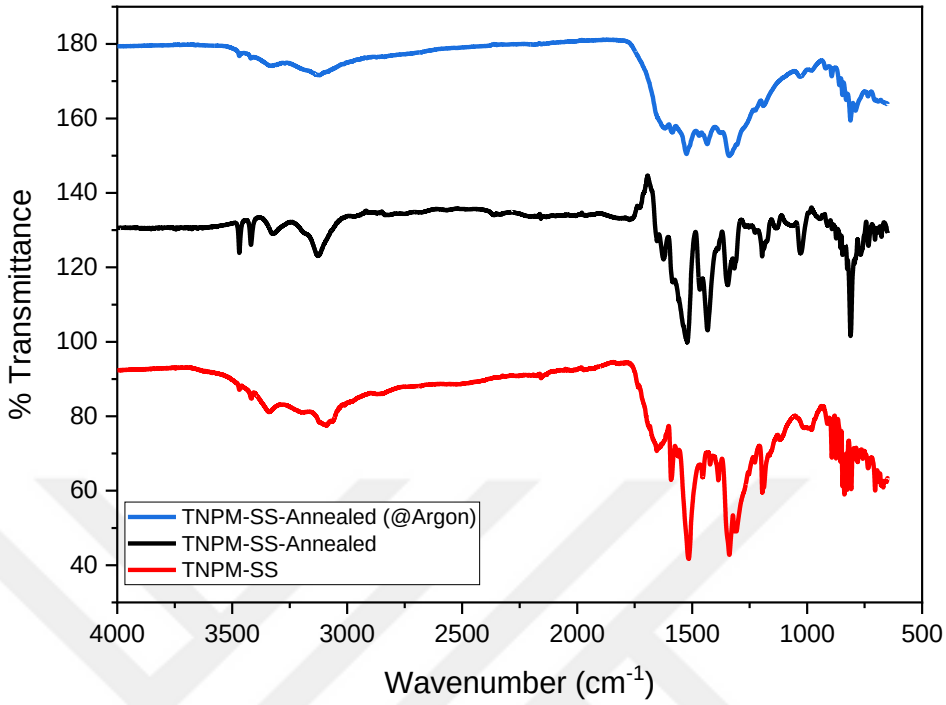

Figure 3.8. FTIR results of before annealing (red), after annealing under air (black) and after annealing under Argon (red).

To be sure that it is not because of oxygen presence in the annealing procedure, annealing under argon atmosphere was tried but as Figure 3.10 shows, CD01AArOAX had quite similar PL trends to CD01X and the whole NIR region advantage of CD01AOAX was disappeared. In addition to that, in Figure 3.10, the annealed form without Oleylamine addition was used directly in xylene, CD01AX, and was not successful like CD01AArOAX. These results proved that the redshift effect comes from OA addition and annealing is not necessary.

Figure 3.8 shows the FTIR spectra of solid-state synthesized reagent of CD01, TNPM-SS, and its derivatives by annealing under air, TNPM-SS-Annealed, and argon, TNPM-SS-Annealed (@Argon), at 200°C for an hour. There are bands centered at 1340 cm^{-1}, 1434 cm^{-1}, 1517 cm^{-1} that correspond to the vibrations of C-H, O-H and N-O respectively. Annealing does not significant effect on N-O stretching but O-H stretching increases under air. As an opposite, 1434 cm^{-1} (O-H) stretching decreases under the argon atmosphere. Both annealing procedures show a similar trend for C-H stretching which may be related to the promotion of carbonization.

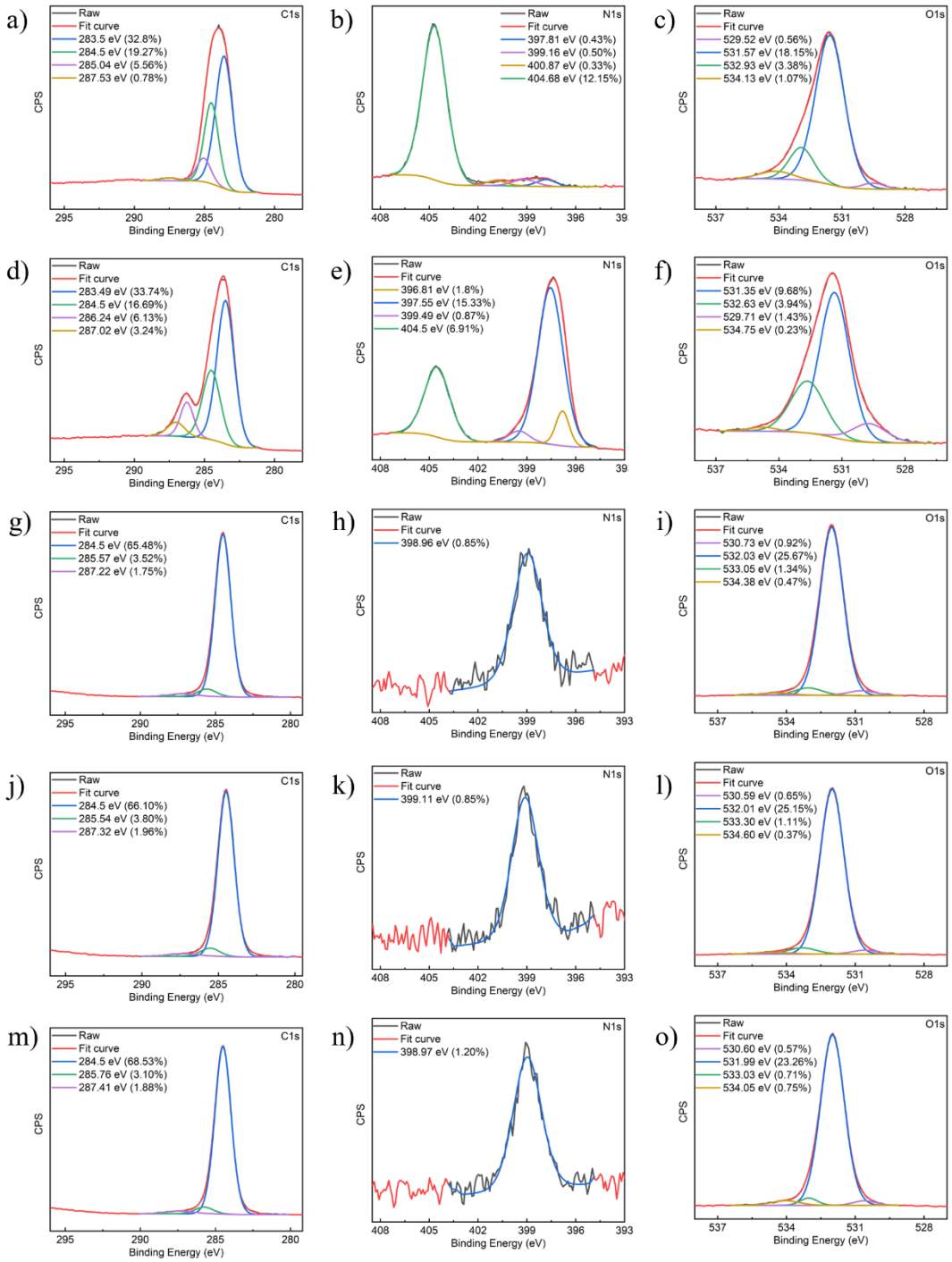

Figure 3.9. XPS results of TNP for a) C1s b) N1s c) O1s, CD01 for d) C1s e) N1s f) O1s, CD01OAX for g) C1s h) N1s i) O1s, CD01AOAX for j) C1s k) N1s l) O1s, CD01AArOAX for m) C1s n) N1s o) O1s

Figure 3.9 shows the elemental analysis for TNP, CD01, CD01OAX, CD01AOAX and CD01AArOAX. According to XPS results, C1s spectrum of TNP displays four distinct peaks at 283.59 eV (C=C), 284.5 eV (C-C), 285.04 eV (C-N) and 287.53 eV (C-O, C=O, CNO), N1s spectrum of CD01 have four peaks at 397.81 eV (pyridinic N), 399.16 eV (C-N-C), 400.87 eV (graphitic?) and 404.5 eV (NO_2), O1s spectrum reveals four peaks at 529.52 eV, 531.57 eV (C-O), 532.93 eV (C=C) and 534.13 eV (NO_2). C1s spectrum of CD01 displays four distinct peaks at 283.49 eV (C=C), 284.5 eV (C-C), 286.24 eV (C-N) and 287.02 eV (C-O, C=O, CNO), N1s spectrum of CD01 have four peaks at 396.81 eV, 397.55 eV (pyridinic N), 399.49 eV (C-N-C) and 404.5 eV (NO_2), O1s spectrum reveals four peaks at 529.71 eV, 531.35 eV (C=O), 532.63 eV (C-OH/C-O-C) and 534.75 eV (NO_2). The CD01 is a solid-state synthesis product of TNP and melamine. In C1s of CD01, the two distinct peaks at 285.04 eV (C-N) and 287.53 eV (C-O, C=O, CNO) increase compared to TNP which proves to introduce melamine to CD01. Another significant proof is the dramatic increase at 397.55 eV (pyridinic N) peak in Figure 3.9.e. After oleylamine addition, sp^2 peak became major in C1s while 285.04 eV (C-N) and 287.53 eV (C-O, C=O, CNO) peaks disappeared. In terms of N1s, 397.55 eV (pyridinic N) peak remained dominant, but others disappeared. Oxygen change with oleylamine was conserving peak at 531.57 eV (C-O) but shifted to the higher energy. Eventually, annealing did not cause a significant change but oleylamine addition as post-synthetic procedure did.

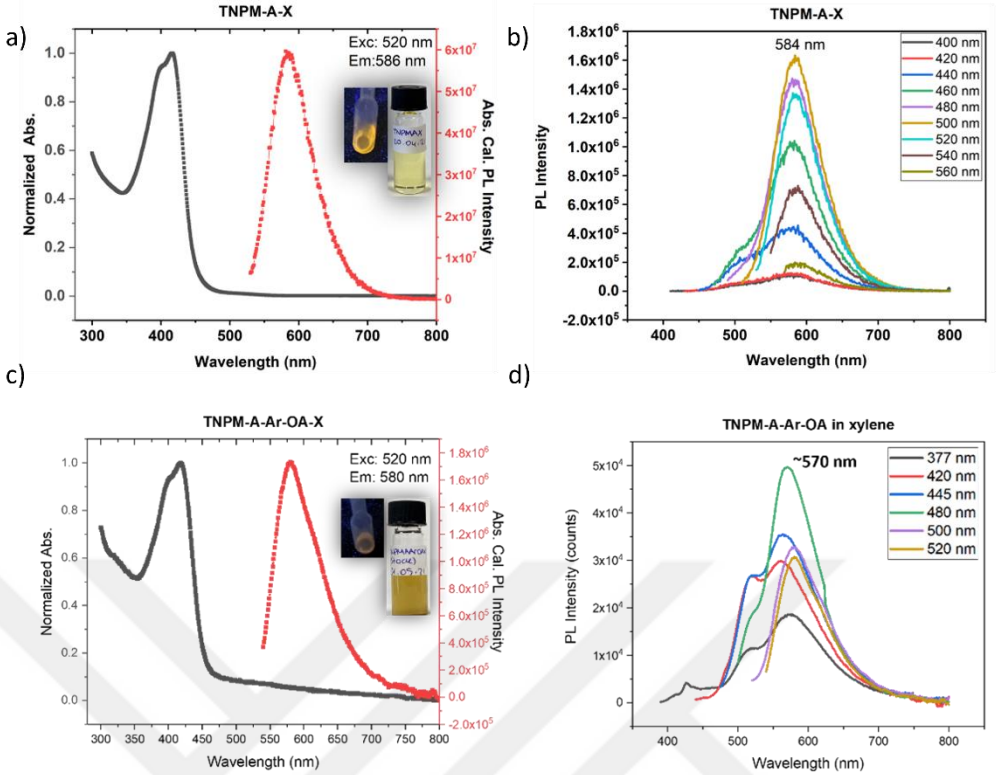

Figure 3.10. UV-Visible and PL spectra of a) CD01AX c) CD01AArOAX and excitation dependent emission spectra of b) CD01AX d) CD01AArOAX.

CDs from organic small precursors are shown with similar XRD patterns in literature. Showing a 2θ peak between 20° and 25° generally indicates the diffraction patterns of graphitic carbon. In Figure 3.10, graphitic carbon indicates a peak at 22° mains constant through OA and annealing modifications however the other peaks get broadened compared to Figure 3.11b, 3.11c and 3.11d. This phenomenon may be a result of decreasing crystalline size. Since CD01 is a carbon dot product after solid-state synthesis, and CD01OAX, CD01AOAX and CD01AArOAX are post-synthesis derivatives, sharper peaks of CD01 may point to relatively bulk compounds. However, once it is dissolved in xylene, the hydrodynamic size of the particle would be around 6 nm according to dynamic light scattering measurement which is smaller than CD01OAX (Table 3.3). The still larger full width at half maximum (FWHM) and diffraction peak broadening in post-synthesis derivatives may be evidence for nanocrystalline materials.

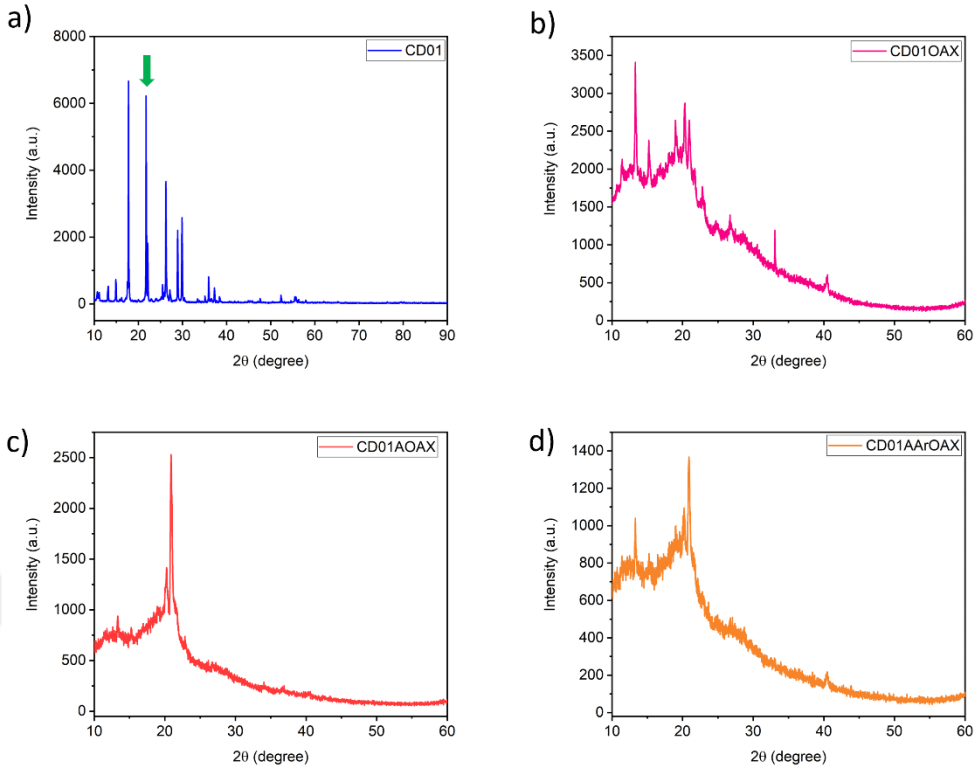

Figure 3.11. XRD results of a) CD01X b) CD01OAX c) CD01AOAX d) CD01AArOAX

The QY data is important to decide which luminescent nanoparticle will be more efficient to use in fuel oils since the mechanism of QY is based on the ratio of photons emitted to photons absorbed. As in Table 3.1, CD01X shows 19.30 % QY but CD01OAX does 15.49 %. Therefore, in terms of QY, oleylamine addition was not an improvement but 15.49 % is still close to QY of CD01X and this absorption to emission conversion occurs at a longer wavelength range which means less overlapping with self-photoluminescence of fuel oils.

Table 3.1. Quantum yield results of CD01X and its derivatives.

Title of CD	**Quantum Yield (%)**	**Excitation (nm)**	**Scanning Range (nm)**
CD01X	19.30	460	470-800
CD01OAX	15.49	520	580-800
CD01AOAX	16.40	480	500-700

Table 3.2. Lifetime results of CD01X, its derivatives and benchmark (F10X5).

Title of CD	**Value (ns)**	**Rel %**	**Excitation (nm)**	**Emission (nm)**
CD01X	3.29	54.76	445	558
	8.89	45.24		
CD01OAX	4.99	61.11	445	642
	23.52	38.89		
CD01AOAX	2.06	17.11	377	570
	5.27	82.89		
F10X5	6.20	98.52	455	608
	34.34	1.48		

In Table 3.2, lifetime measurements are summarized. These results are important as it is an experiment that shows how long and how many photoluminescent events take. Corresponding excitation wavelengths were limited to existing light sources which the lifetime experimental set-up has. Therefore, the closest excitation sources to the actual excitation wavelength which gives maximum emission were chosen. The common features of CDs according to this table can be listed as follows: multi-events and majority belong to shorter events. Only annealing seems to affect this trend in an opposite direction and longer event (5.27 ns) has a higher relative percentage (82.89).

3.3.2 Oleylamine and CD01 Interaction

While redshift can be provided by oleylamine addition to CD01 with post-synthesis procedure, annealing under air and argon did not help to keep that shift so CD01OAX became more favorable. However, it is important to understand the interaction between oleylamine and CD01. Firstly, the image of CD01OAX in Figure 3.12 was obtained to indicate nanoparticles. In Figure 2.10, CD01 itself was shown as a more amorphous structure than being high crystalline. Since the image taken from the solid synthesis product it is also compatible with sharp diffraction peaks of CD01 in the XRD graph in Figure 3.11. After oleylamine addition, crystalline clusters became more visible to observe as seen in Figure 3.12.

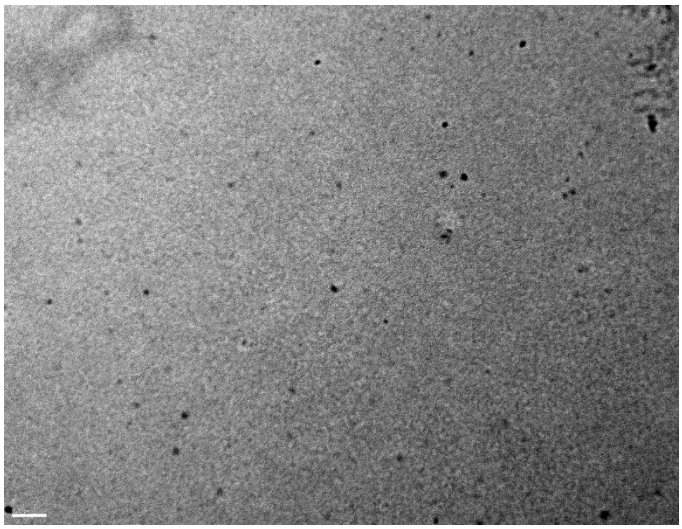

Figure 3.12. TEM image of CD01OAX

CD01 could not dissolve in gasoline or diesel directly. Therefore, oleylamine was first tried to dissolve CD01 in gasoline and interestingly a slow color change was observed after successfully managing to dissolve CD01. As a next thing, to fabricate colloidally stable CD01 with oleylamine, oleylamine was added to CD01 powder form and then dissolved in xylene. A similar color change was observed. In Figure 3.13, this time-dependent color change was reported by using UV-Visible absorption and photoluminescence spectra. Under daylight, the yellow color turned into orange first and finalized at reddish pink. Accordingly, emission color got more intense and slightly shifted to red. This image-based color change observation was also confirmed by UV-Visible absorption spectra and at 531 nm peak dramatically increased in time. Similarly, more absorption causes more photons to excite so PL intensity also increased. However, the maximum intensity was reached after eight days and then due to the quenching effect, PL intensity started to decrease even though absorption continued to increase.

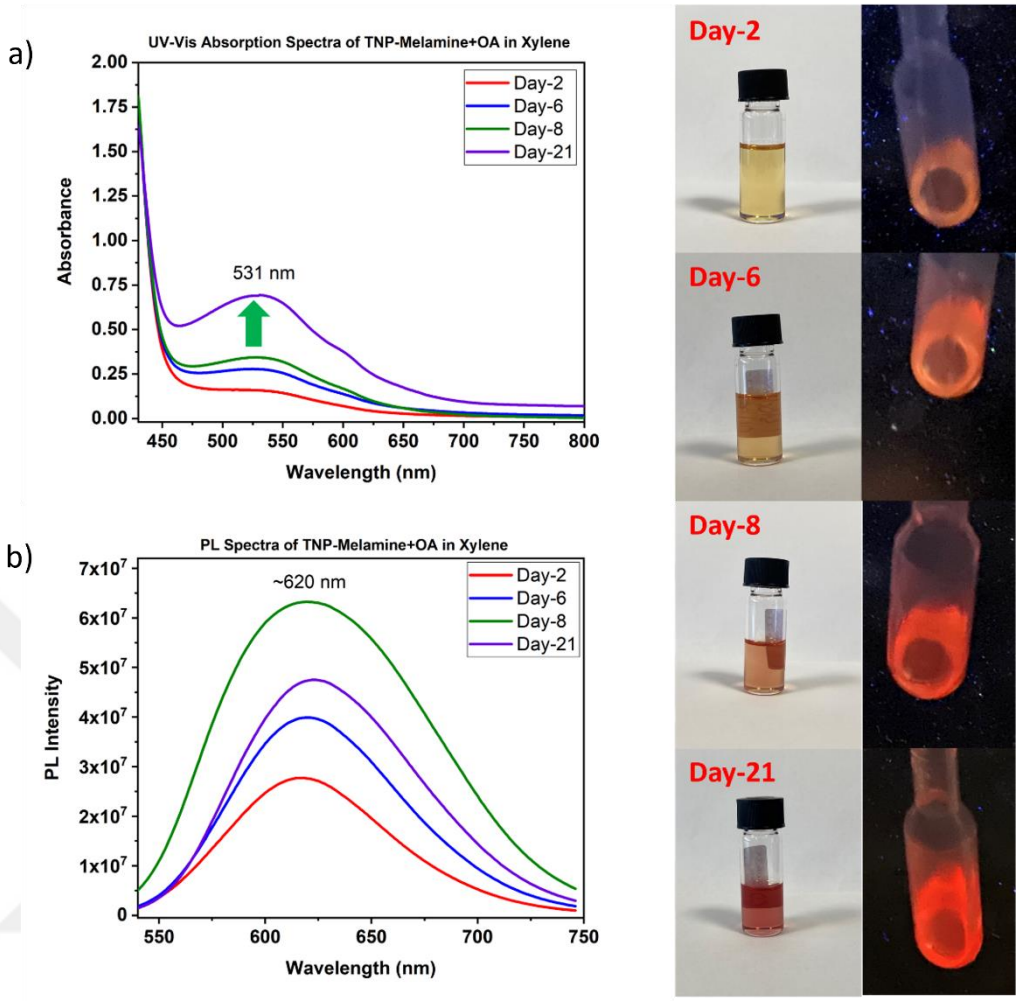

Figure 3.13. Daily tracking of a) UV-Visible b) PL spectra after OA addition to CD01 and image changes under daylight and 366 nm UV light.

When oleylamine interacts with CD01, hydrodynamic size sharply increases. This is not surprising since an excess amount of oleylamine was used compared to CD01 and it helps to stabilize the bare surface of the carbon dot. In time, this interaction became stronger and size increases to micron level, it may show the formation of clusters of oleylamine and carbon dot as seen in Table 3.3.

Table 3.3 Daily tracking of CD01 after OA addition in terms of hydrodynamic size.

Title of CD	**Size by number (nm)**	**Size by intensity (nm)**	**PDI**
CD01 in xylene	6.522 (±2.169)	28.13 (±20.17)	0.309
CD01OAX (Day-0)	710.5 (±106.7)	723.9 (±82.01)	0.314
CD01OAX (Day-40)	5413 (±648.0)	5406 (±305.1)	0.416

3.3.3 Oleylamine Optimization

Once oleylamine addition is confirmed as an improvement for CD01, the next thing was performing the optimization of oleylamine amount. Three different CD:OA w/w ratios were tried as 1:80, 1:200 and 1:400. If the ratio is smaller, the color change will less significant, and the redshift will be shorter.

As seen in Figure 3.14, when the OA amount increases, color change takes place in a shorter period. And daily tracking proved that the absorbance increases around 530 nm as in Figure 3.13. Among three ratios, both 1:200 and 1:400 gave similar high PL intensity at day zero. And their PL intensities were slightly shifted to red compared to 1:80. The common event was PL intensity increase in time but the 1:400 ratio quenched after a month. Moreover, the 1:200 ratio kept a red-shifted emission peak with increasing intensity. Therefore, the optimum w/w ratio between CD and OA was considered as 1:200.

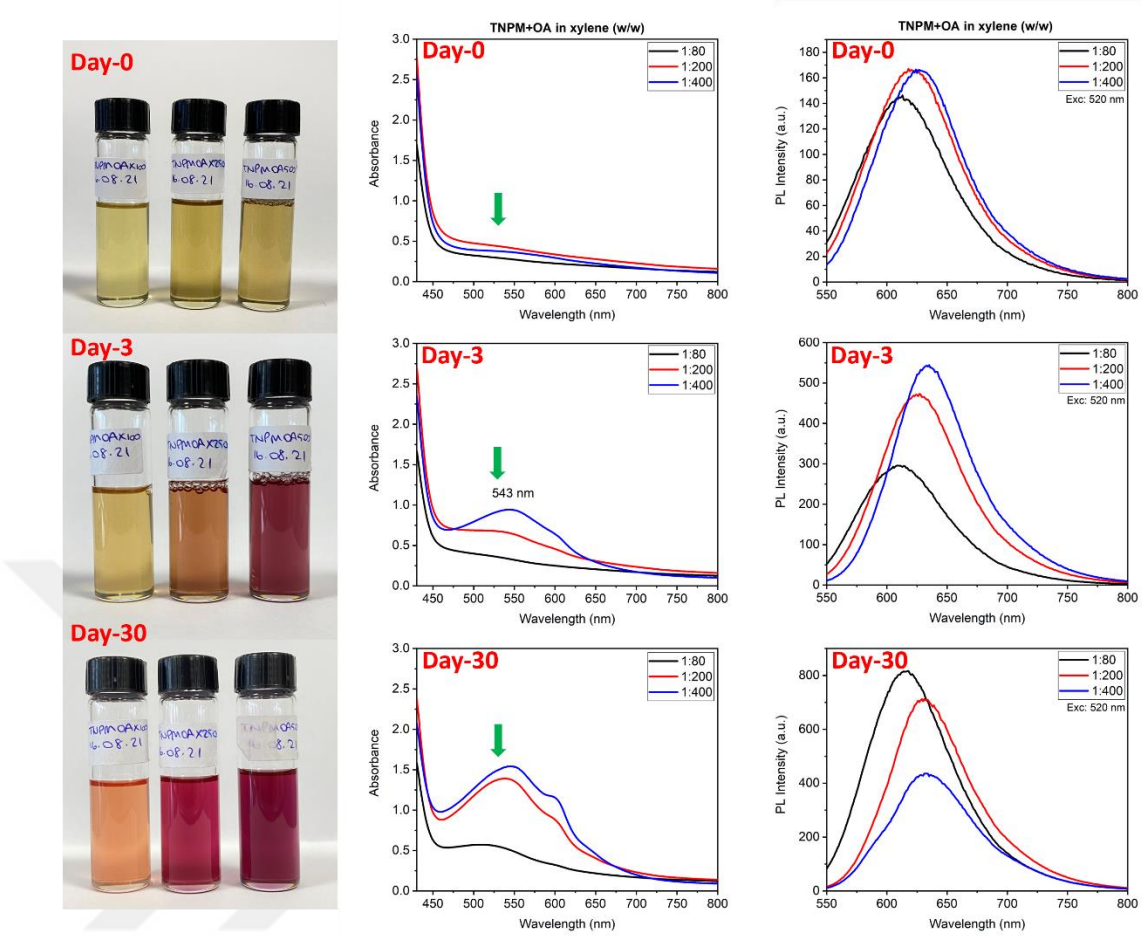

Figure 3.14. Daily tracking of UV-Visible and PL spectra after OA addition with 1:80, 1:200 and 1:400 w/w ratios to CD01 and their image changes under daylight.

3.3.4 CDs in AdBlue

Other than gasoline and diesel, there is a rising product in the market, AdBlue. AdBlue is a market name for 30% urea solution which is used as an emission filter in diesel engines. Since it is an aqueous product, organic CDs are not useful for tagging. CD07 and CD24, both successfully fabricated aqueous CDs, were put in AdBlue with different concentrations. Since AdBlue is a non-luminescent product even 1 ppm CD was enough to tag the product as seen in Figure 3.15. Low concentration requirement is an advantage in terms of cost-benefit on an industrial scale. Another advantage was stability which provides longer shelf life. For CD07, that period was at least seven months without PL intensity loss. For CD24, after seven months still, high PL intensity was observed even with 54.5% loss.

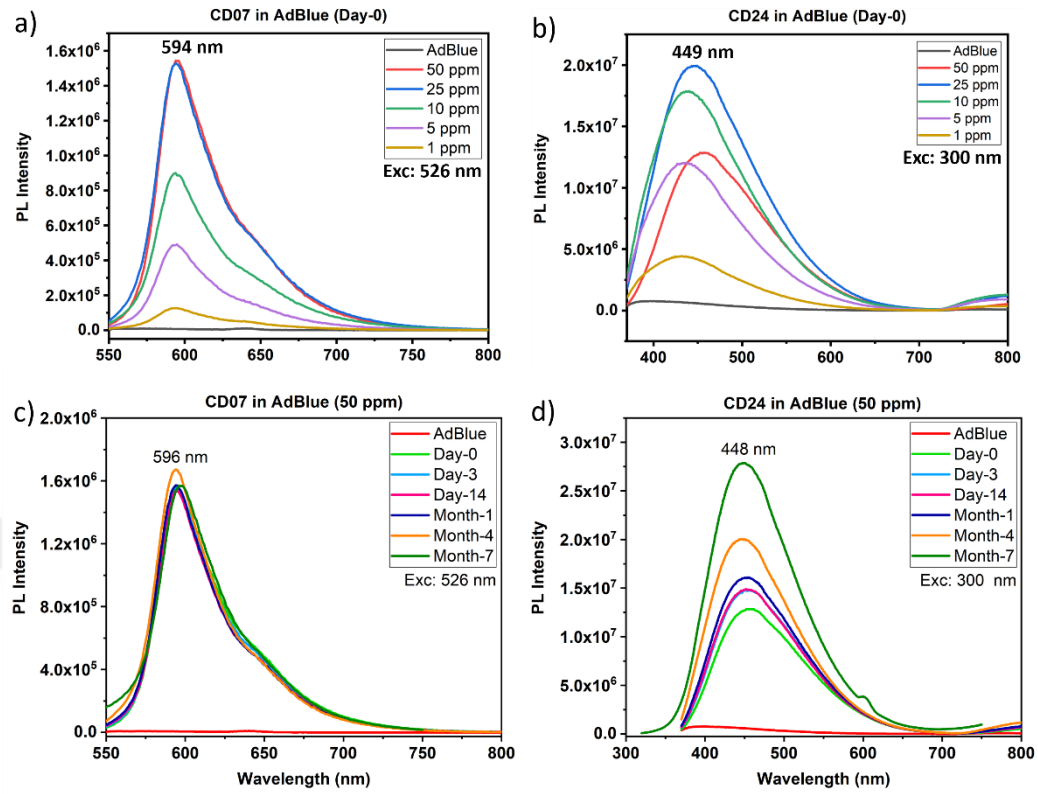

Figure 3.15. Concentration dependent PL spectra of a) CD07 b) CD24 in AdBlue, PL stability spectra of c) CD07 d) CD24 in AdBlue.

CD07 is a better candidate for tagging material in AdBlue since it has enhanced stability over time. However, CD07 itself has a pH-dependent characteristic and that makes understanding how PL change in AdBlue is important. The red line in Figure 3.16 shows CD07 product after standard synthesis procedure which is in acidic pH. If pH would be 7, it shifts to blue, and intensity slightly decreases. Finally, if basic medium due to AdBlue would be the case, this blue shift and intensity decrease become dramatic. Consequently, CD07 loses a part of its photoluminescence intensity in AdBlue and yet that much PL difference can maintain stability after seven months and that makes the CD07 more favorable than CD24 as AdBlue tag.

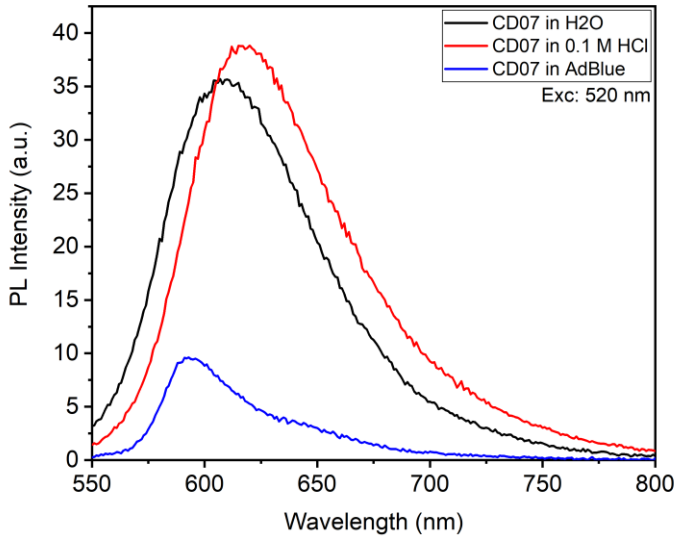

Figure 3.16. PL spectra of CD07 (25 ppm) in H_2O, 0.1 M HCl and AdBlue.

3.3.5 Barcode with CDs in AdBlue

Since both CD07 and CD24 have excitation independent emission, their emission wavelengths around 600 nm and 455 nm respectively are suitable for barcode trials. 420 nm was chosen as an excitation wavelength since they have enough PL intensity in their emission regions when excited at 420 nm.

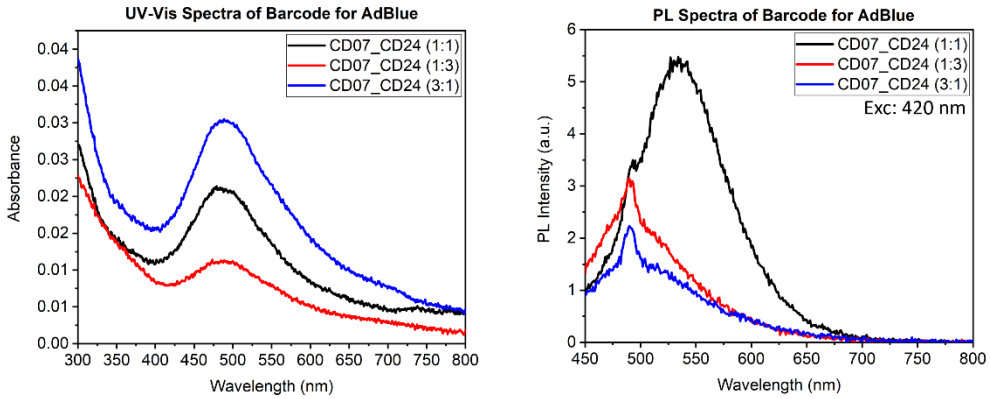

Figure 3.17. UV-Visible and PL spectra of barcode trials by using CD07 and CD24 in AdBlue according to 1:1, 1:3 and 3:1 ratios.

Although different ratios were tried, the expectation of preserving two different emission centers from two different CDs could not execute. The UV-Visible graph in Figure 3.17 shows the dominance of CD07 even for 1:3 (CD07:CD24) ratio. However, PL data does not perfectly match with CD07. This may indicate that two different emission centers could not be preserved but they engaged in all ratios.

3.4 Conclusion

Influence of post-synthetic procedures such as treatment with OA or thermal annealing of CDs, specifically, CD01 was investigated. Photostability and emission intensity was improved with OA treatment but not with the annealing. The most important outcome was the redshift in photoluminescence after OA treatment. Due to this redshift, CD01OAX showed 92.7% ΔPL against gasoline which is similar performance to the benchmark, however in diesel, the benchmark had 37.5% ΔPL at 525 nm excitation wavelength while CD01OAX had 61.5% as seen in Figure 3.5. And the amount of OA was optimized as 1:200 w/w (CD/OA) ratio.

In literature, only one study so far has been reported that uses carbon-based nanoparticle as a tracer in crude oil. However, this blue-emitting particle gives excitation independent emission at 453 nm and that is highly dominated by the photoluminescence of gasoline itself. Therefore, their relatively easier synthesis method (microwave for 6 min at 300 W) does not provide a substantial advantage over CD01OAX.

In addition to this promising performance of CD01OAX, tagging ability was investigated for AdBlue. Although the barcode system did not work successfully, individual CD tagging in AdBlue worked well with both CD07 and CD24 and they were stable in terms of photoluminescence even after seven months.

Chapter 4:
INVESTIGATION OF PAA@SPION NANOPARTICLES WITH ORGANIC PHOTOSENSITIZER FOR ENHANCED PHOTODYNAMIC THERAPY

4.1 Introduction

Among the cancer treatment methods, photodynamic therapy requires a minimally invasive procedure. This therapy is based on cytotoxicity of reactive oxygen species (ROS) by light irradiation of dye sensitizers. In literature, photosensitizer chart consists of porphyrin and non-porphyrin type dye molecules such as protoporphyrin IX, rhodamine, methylene blue or BODIPY. Hydrophilic PSs show poor cell penetration and their stability under biological conditions are low. On the other hand, hydrophobic PSs have their drawbacks like aggregation in aqueous media and taking a longer time to eliminate from the patient body. To better efficiency with organic PSs may be possible by combining them with nanoparticles. Possible advantages of NP usage are better drug delivery and then higher cancer cell death and lower healthy cell toxicity.

SPIONs have been attracted to phototherapy since their biocompatible nature and several FDA approved compositions. In recent years, different PSs decorated on SPIONs for better delivery of PS in PDT studies have increased. Among PSs, BODIPY shows superior characteristics such as high absorption coefficient, photostability, ease of modification. However, hydrophobic core and tumor selectivity may a problem. In 2019, Karaman et al. introduced a new type of BODIPY, BOD-Se-I, which bears an iodo-selenophene group at 2,6-positions and a cationic methyl pyridinium unit at 3,5-positions (Figure 4.1) (Karaman et al., 2019).

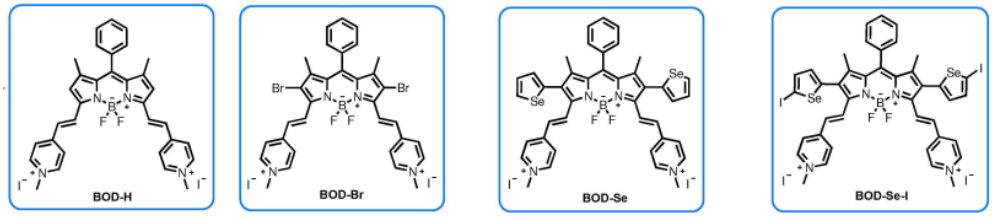

Figure 4.1. Chemical structures of BODIPY derivatives.

In this chapter, the aim to deliver BOD-Se-I (it will be mentioned as just BODIPY at the following parts) selectively to tumor cells to enhance its PDT efficiency while reducing its toxicity in healthy cells. For this purpose, EGFR targeting Cetuximab (Cet) was conjugated PAA@SPION and was used as a non-toxic delivery vehicle of the BODIPY derivative with low water solubility and poor stability. Overall, BODIPY loaded Cet conjugated nanoparticles were designed for antibody-mediated targeting of EGFR(+) colon cancer cells and hence, improved PDT of the targeted cancer cells.

4.2 Experimental

4.2.1 Materials

All reagents that were used in the synthesis of BODIPY were purchased from Sigma and used as supplied without further purification. Iron (II) chloride and iron (III) chloride were obtained from Merck (purity levels 99 %, Darmstadt, Germany). Poly (acrylic acid) (Mw 5100 kDa) and dimethyl sulfoxide Hybrid-Max™ were purchased from Sigma (MO, USA). Vivaspin 20 centrifugal filters were provided by Sartorius (Goettingen, Germany). McCoy, MEM, trypsin EDTA and penicillin-streptomycin solutions were purchased from Multicell, Wisent Inc. (QC, Canada). Fetal bovine serum (FBS) was obtained from Capricorn Scientific GmbH (Ebsdorfergrund, Germany). Phosphate-buffered saline (PBS) and thiazolyl blue tetrazolium bromide (MTT) were provided by Biomatik Corp. (ON, Canada). 96-well plates were purchased from Nest Biotechnology Co., Ltd (Wuxi, China). Only ultra-pure water (18.2 MΩ, RephiLe Bioscience and Technology, Shanghai, China) was used when needed.

4.2.2 Synthesis

PAA Coated Iron Oxide Nanoparticle Synthesis: Iron (III) and Iron (II) salts (2:1) were dissolved with 1.2 g of PAA in deoxygenated water. Obtained solution after 20 min at 85°C under argon atmosphere was combined with 4.63 mL of 4.5 M NH_4OH as vigorous stirring continued. A colloidal solution was produced after 1-hour reaction. Once the solution reached room temperature, final PAA coated SPIONs were washed to

remove residuals by using 5 kDa centrifugal filters with DI water several times and stored at room temperature.

BODIPY Synthesis: BODIPY was synthesized according to the literature (Karaman et al., 2019).

Dye conjugation to PAA@SPIONs: Using EDC/NHS chemistry, Alexa FluorTM 647 Cadaverine was conjugated to PAA@SPIONs. Firstly, activation of PAA@SPIONs with $3.088x10^{-8}$ mol EDC and sulfo-NHS in MES buffer was performed for 30 min. The buffer of activated PAA@SPIONs was exchanged to PBS (pH=7.4) with centrifugal filters. Lastly, $1.961x10^{-5}$ mol of Alexa FluorTM 647 Cadaverine was added and let the reaction occurs for 24 h. The final mixture was quenched by adding excess hydroxylamine. And dye conjugated PAA@SPIONs were purified with PBS using centrifugal filters.

Cet conjugation to Dye-PAA@SPIONs: NH2-PEG-MI was used in Cet conjugation to SPIONs as a bridge. SPIONs were activated in MES buffer using $2.264x10^{-7}$ mol EDC and sulfo-NHS. Then, the buffer was replaced with PBS buffer (pH=7) and then $2.264x10^{-8}$ mol NH2-PEG-MI was added in PBS to solution. After 24 h reaction, the solution was washed with PBS through 3 kDa centrifugal filters. Cet was thiolated to react with maleimide of the PEG via thiol-ene reaction. $2.264x10^{-8}$ mol Cet was mixed with $2.264x10^{-6}$ mol iminothiolane solutions (Traut's reagent, pH = 8) for 2 h at room temperature and then washed with centrifugal filters with phosphate buffer-EDTA. Thiolated-Cet was added to PEG-SPION solution and mixed for 24 h at room temperature. Then, Cet conjugated SPIONs were washed with 100 kDa centrifugal filters several times. Bound Cet was calculated from Bradford assay. Briefly, calibration curve was prepared by free BSA at different concentrations. 1 mL of each reference or washed product of Cet-PAA@SPION was mixed with 1 mL of Bradford reagent and shaken for 10 min at room temperature. Then, the absorbance of that solution at 595 nm was recorded using UV-Vis spectroscopy.

BODIPY loading to conjugated and non-conjugated SPIONs: BODIPY at a concentration of 1 mg/mL was added dropwise to PAA@SPION and Cet-PAA@SPION (50 mg) and mixed at 750 rpm for 2 h at room temperature. Isothermal titration calorimetry (Affinity ITC, USA) was used to confirm electrostatic loading of BODIPY to SPIONs. SPIONs (1 mg/mL) were titrated with BODIPY at 25 °C.

4.2.3 Characterization

Hydrodynamic sizes and zeta potential data was obtained by using a Malvern Zetasizer Nano ZS. Absorbance measurements were performed using a Shimadzu UV-VIS-NIR spectrophotometer and the range was 600-800 nm. The iron content of prepared NPs was determined using an Agilent 7700XICP-MS (inductively coupled plasma-mass spectrometer). The samples for that were prepared by digestion with a mixture of sulphuric and nitric acid.

4.2.4 Detection of singlet oxygen generation (SOSG) in solution

Singlet oxygen generation capacities of BODIPY, PAA@SPION, BODIPY-PAA@SPION, BODIPY-Cet-PAA@SPION were investigated by using a trapping molecule Singlet Oxygen Sensor Green (SOSG) in aqueous solutions (PBS pH 7.4, 1% DMSO). Each sample containing 10 mM of BODIPY was mixed with 5 μM SOSG solution in oxygen bubbled PBS (pH 7.4, 1% DMSO). The first measurement was taken in dark and then the solution was exposed to the LED light (635 nm, 66.7 mW/cm^2) for 5 minutes with 1-minute intervals. After each irradiation, the emission change of SOSG at 524 nm was recorded (λex = 504 nm).

4.2.5 Cell culture and conditions

HT29, SW480 and L929 cells were cultured in McCoy's 5A, MEM and DMEM medium respectively supplemented with 10 % (v/v) fetal bovine serum and 1 % (v/v) penicillin streptomycin and incubated in a 5 % CO_2 humidified incubator at 37 °C.

4.2.6 Cytotoxicity assays

The cytotoxicity of free BODIPY and prepared NPs in HT29, SW480 and L929 cells were examined using MTT ((Thiazolyl blue tetrazolium bromide (3-(4, 5-dimethylthiazol-2-yl)-2, 5-diphenyltetrazolium bromide)) assay protocol. The density of seeded cells for this assay was 1x10^4 cells per well. And 96 well plates were used during the 24 h incubation. Injection of different concentrations of BODIPY and prepared NPs into cells was performed in a fresh culture medium. 50 μL of MTT (5 mg/mL in PBS) solution and 150 μL fresh medium were added to cells after 4 h incubation. Finally, the

formation of purple formazan crystals by the viable cells was dissolved with the addition of DMSO:Ethanol (1:1 v/v). Reading absorbance was 570 nm and reference was 650 nm at Synergy H1 (Biotek Instruments). The results were analyzed by using GraphPad Prism 8 software (California, U.S). Relative cell viability was found by dividing absorbance of sample to absorbance of control and multiplied by 100.

4.2.7 In vitro imaging of free BODIPY and prepared NPs

The density of seeded cells for in vitro imaging was $1.75x10^5$ cells per well. And 6 well plates were used during the 24 h incubation. In the following step, cells were treated with free BODIPY and prepared NPs (0.1 µg/mL BODIPY or 23 µg/mL Fe) for 4 h. Then, the medium was removed, and 4 % paraformaldehyde was used to fix the cells. Let cells to be fixed for 20 min incubation and then washed with PBS (x3). Nuclear staining dye DAPI was added at 10 µg/mL and cells were incubated for 15 min. To remove excess DAPI, cells were washed with PBS (x3). As control cells, without free BODIPY or NPs were used. Images were obtained by a Zeiss fluorescence microscope using filters for DAPI (λexc=365 nm and λem=461 nm) and AF647 (λexc=640 nm and λem=670 nm), respectively.

4.2.8 In vitro LED irradiation

The density of seeded cells for this assay was $1x10^4$ cells per well. And 96 well plates were used during the 24 h incubation. Injection of different concentrations of BODIPY and prepared NPs into cells was performed in a fresh culture medium. An uptake of particles by cells continued for 4 h incubation and the cell medium were refreshed at the end. Using 635 nm LED at 66.7 W/cm^2 for 5 min from the top of the plate, irradiation of cells was performed. After irradiation, cells were placed for 24 h incubation. Finally, the MTT assay protocol was used to determine the cell viability as mentioned before. Cells that were not treated with free BODIPY, NPs or LED were used as a control.

4.2.9 In vitro ROS generation

SW480 and HT29 cells were seeded and treated with free BODIPY and BODIPY-Cet-SPIONs as described above. Each group was treated with 10 µM DCFH-DA for 40 min at 37 °C after 4 hours incubation. Then each group was irradiated using LED light

(635 nm, 66.7 mW/cm^2) for 5 min. Fluorescence intensity was read at Ex/Em=485/535 nm using a microplate reader (Synergy H1, Biotek Instruments).

4.2.10 Statistical analysis

Statistical significance of data was determined using Kruskall-Wallis one-way analysis of variance followed by Dunn's comparison test of GraphPad Prism software package (GraphPad Software, Inc., CA, USA). P value < 0.01 was considered for statistical significance. All data were reported as mean ± standard deviation (SD).

4.3 Results and Discussion

4.3.1 Preparation and characterization of Cet conjugated BODIPY loaded SPIONs

BODIPY was loaded onto anionic SPIONs tagged with Cet for tumor-specific PDT for the treatment of colon cancer. These nanoparticles were prepared as mentioned in section 4.2.2. First, anionic PAA coated SPIONs were synthesized by a co-precipitation method as described previously by our group. To track the nanoparticles in cells, nanoparticles were labelled with a fluorescent dye (Alexa Fluor 647). Then, Cet was conjugated to 0.1 mol % carboxylic acid groups of dye tagged SPIONs to target EGFR overexpressing cells via a PEG spacer to enhance the availability of Cet to EGFRs. Briefly, NH2-PEG-MI (2 kDa) was conjugated PAA@SPIONs using EDC/NHS chemistry. Cet was thiolated using Trout's reagent thiol-ene chemistry. The Cet conjugation efficiency to SPIONs was calculated as 95% using Bradford assay. Finally, cationic BODIPY was loaded non-conjugated and Cet-conjugated anionic PAA@SPIONs via electrostatic interaction. Size results in Table 4.1 showed that all prepared NPs can be considered as small and surface functionalization did not cause any aggregation in hydrodynamic sizes. PAA@SPIONs have number-based hydrodynamic size of 16.71 nm with ζ potential of -52.5 mV. There was no significant change in size after Cet conjugation (Cet-PAA@SPION, 14.46 nm) and BODIPY loading (BODIPY-PAA@SPION, 7.586 nm) to PAA@SPION. However, the ζ potential was measured as -35.9 and -30 mV for Cet-PAA@SPION and BODIPY-PAA@SPION, respectively. BODIPY loading increases the hydrodynamic size of the Cet conjugated PAA@SPION, slightly (73.90 nm) and reduced the ζ to -38.5 mV.

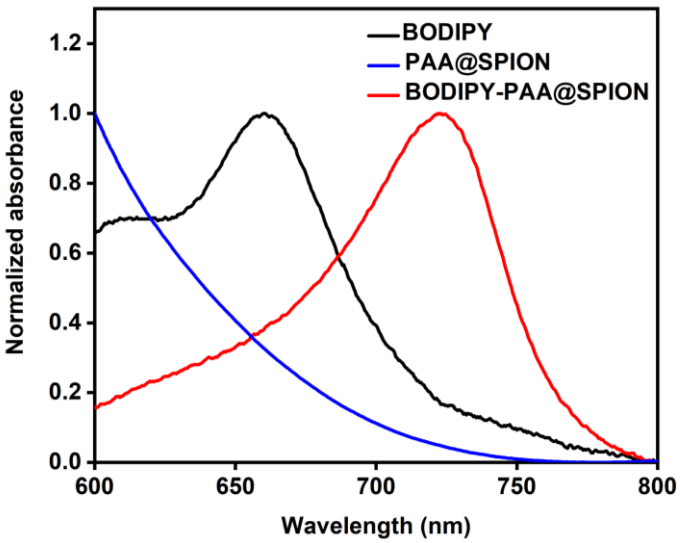

Figure 4.2. UV-vis absorption spectra of BODIPY, PAA@SPION and BODIPY-PAA@SPION.

Figure 4.2 shows UV-vis absorbance spectrum of BODIPY, PAA@SPION and BODIPY-PAA@SPION in the 600-800 nm range. PAA@SPION has decreasing absorbance with wavelength from 600 to 800 nm; however, BODIPY possess a strong absorbance peak at 660 nm. After BODIPY loading, PAA@SPION has strong absorbance peak at 720 nm. Overall, small, anionic, targeted SPIONs with BODIPY were successfully produced for enhanced PDT of colon cancer cells.

Table 4.1. Hydrodynamic sizes and zeta potential of BODIPY, PAA@SPION, Cet-PAA@SPION, BODIPY-PAA@SPION and BODIPY-Cet-PAA@SPION in water.

Sample	Size by number (nm)	Size by intensity (nm)	Zeta potential, ζ (mV)
BODIPY	22.57	152.2	18.4
PAA@SPION	16.71	21.23, 105.8	-52.5
Cet-PAA@SPION	14.46	68.94	-35.9
BODIPY-PAA@SPION	7.586	106.6	-30
BODIPY-Cet-PAA@SPION	73.90	116.7	-38.5

4.3.2 Dark toxicity of BODIPY and prepared nanoparticles

The dose-dependent dark toxicity of free BODIPY, PAA@SPIONs, Cet-PAA@SPIONs, BODIPY-PAA@SPIONs and BODIPY-Cet-PAA@SPIONs was evaluated on SW480, HT29 and L929 cell lines between 0.1-5 µg BODIPY/mL and 23-1150 µg Fe/mL concentration using MTT assay after 4 h incubation as seen in Figure 4.3. Prepared NPs were biocompatible on both healthy and cancer cell lines in the studied concentration range. Free BODIPY did not cause any significant cell death on the HT29 cell line; however, viability dropped to 76.8 at 5 µg/mL on the SW480 cell line. On a healthy cell line, cell viability was between 76-88 % in the 0.5-5 µg BODIPY/mL concentration range. These results suggest that prepared NPs more biocompatible than free BODIPY on the healthy cell line.

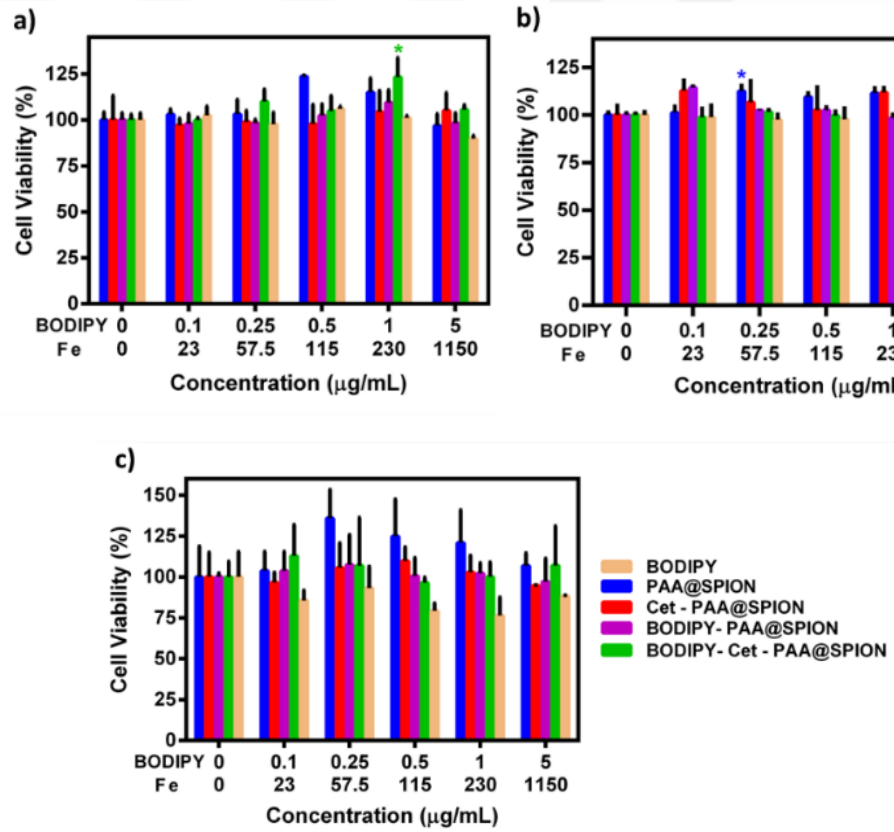

Figure 4.3. Dose dependent cell viability of a) HT29, b) SW480 and c) L929 cells treated with free BODIPY, PAA@SPION, Cet-PAA@SPION, BODIPY-PAA@SPION and BODIPY-Cet-PAA@SPION after 4 h incubation. Untreated cells were used as control. Data are expressed as mean ± SD (n=3).

4.3.3 Cell imaging

Internalization of free BODIPY, PAA@SPION, Cet-PAA@SPION, BODIPY-PAA@SPION and BODIPY-Cet-PAA@SPION was investigated by each cell line with fluorescence microscopy after 4 h incubation at 0.1 µg/mL. No signal was recorded in PAA@SPION or Cet-PAA@SPION treated cell lines as seen in Figure 4.4 Figure *4.4*. Fluorescence microscopy images of a) HT29, b) SW480 and c) L929 cells after 4 h incubation with free BODIPY and prepared NPs. (i) Control, ii) free BODIPY, iii) PAA@SPION, iv) Cet-PAA@SPION, v) BODIPY-PAA@SPION and vi) BODIPY-Cet-PAA@SPION) indicating that longer incubation time is necessary for high uptake of nanoparticles.

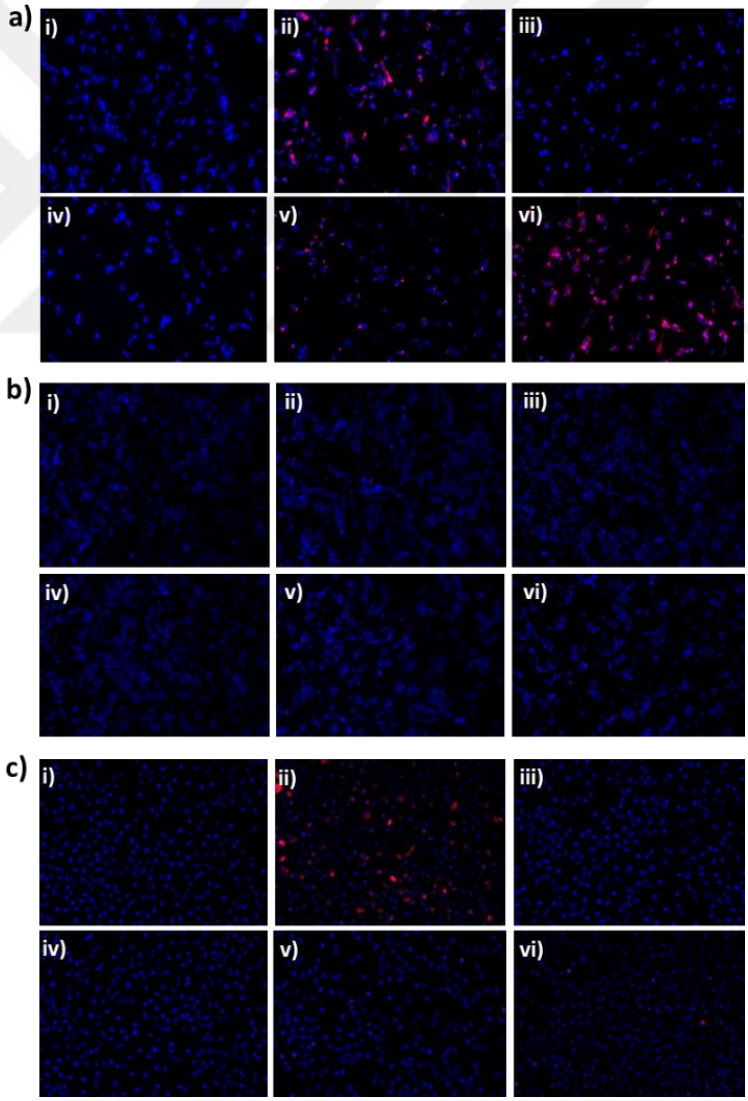

Figure 4.4. Fluorescence microscopy images of a) HT29, b) SW480 and c) L929 cells after 4 h incubation with free BODIPY and prepared NPs. (i) Control, ii) free BODIPY,

iii) PAA@SPION, iv) Cet-PAA@SPION, v) BODIPY-PAA@SPION and vi) BODIPY-Cet-PAA@SPION)

In HT29 cell line, uptake of BODIPY-Cet-PAA@SPION was dramatically higher than free BODIPY at 0.1 µg/mL (Figure 4.4a). Due to high EGFR expression of HT29 cell line, strong fluorescence signal was observed with BODIPY-Cet-PAA@SPION compared to BODIPY-PAA@SPION as well. In SW480 cell line, no fluorescence signal was observed with free BODIPY or prepared NPs at 0.1 µg/mL (Figure 4.4b). At high concentration (1 µg/mL), a significantly higher fluorescence signal was recorded with both free BODIPY and BODIPY-Cet-PAA@SPION as seen in Figure 4.5. L929 cells showed a strong fluorescence signal of free BODIPY while there was no signal in L929 cells with BODIPY-PAA@SPION and BODIPY-Cet-PAA@SPION (Figure 4.4c). Imaging results showed that high amount of BODIPY can be delivered specifically to high EGFR-expressing cancer cell line in short incubation time.

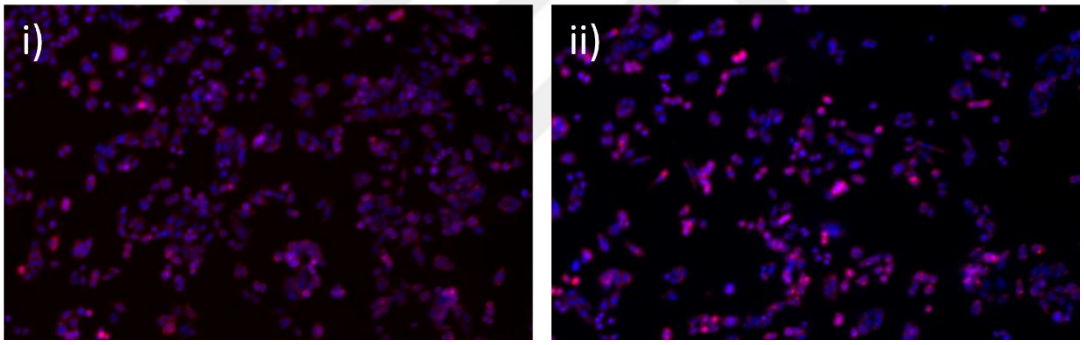

Figure 4.5 Fluorescence microscopy images of SW480 cells after 4 h incubation at 1 µg/mL with i) free BODIPY and ii) BODIPY-Cet-PAA@SPION

4.3.4 Detection of singlet oxygen generation (SOSG) in solution experiments

Photosensitized $^1O_2$ generation of all agents was first investigated in oxygen saturated solutions (PBS, pH 7.4, 1% DMSO) by utilizing a $^1O_2$-selective water-soluble trap molecule, Singlet Oxygen Sensor Green (SOSG). SOSG emission is quenched because of an effective PeT mechanism and its characteristic green emission at 530 nm can only be restored in the presence of $^1O_2$. Irradiation of all samples with a 635 nm red LED light source for 5 min resulted in a turn-on response in SOSG emission, suggesting that these agents can trigger $^1O_2$ formation upon excitation.

Fluorescent enhancement was found to be more pronounced in the case of BODIPY-PAA@SPION and BODIPY-Cet-PAA@SPION, which may be at least partially

attributed to improved water solubility and consequent less aggregate formation upon SPION conjugation.

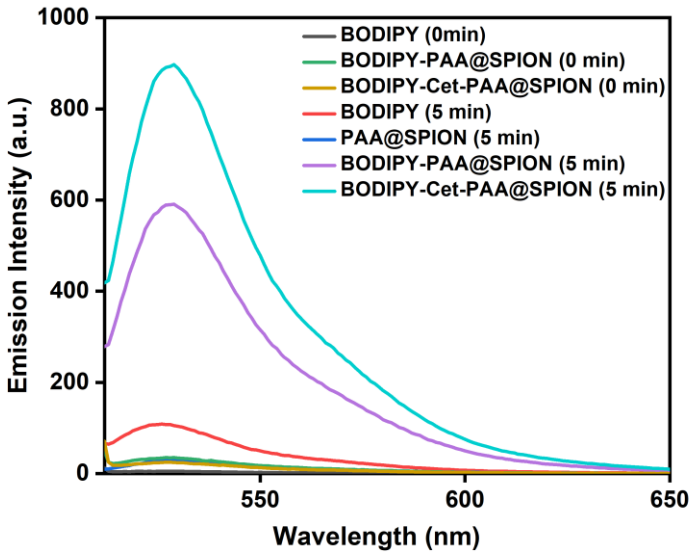

Figure 4.6. Fluorescence spectra of free BODIPY and prepared NPs in PBS buffer (pH 7.4).

4.3.5 Phototoxicity and enhanced PDT

Phototoxicity of free BODIPY, PAA@SPIONs, Cet-PAA@SPIONs, BODIPY-PAA@SPIONs and BODIPY-Cet-PAA@SPIONs was investigated under 635 nm irradiation using 66.7 mW/cm^2 after 5 min. Same LED conditions were applied to cells that were not treated with free BODIPY or prepared NPs to confirm the safety of the LED irradiation protocol itself. Furthermore, LED irradiation of PAA@SPION and Cet-PAA@SPION did not cause any reduction in the cell viability as well indicating that SPION does not create significant phototoxicity at these studied doses on both cell lines.

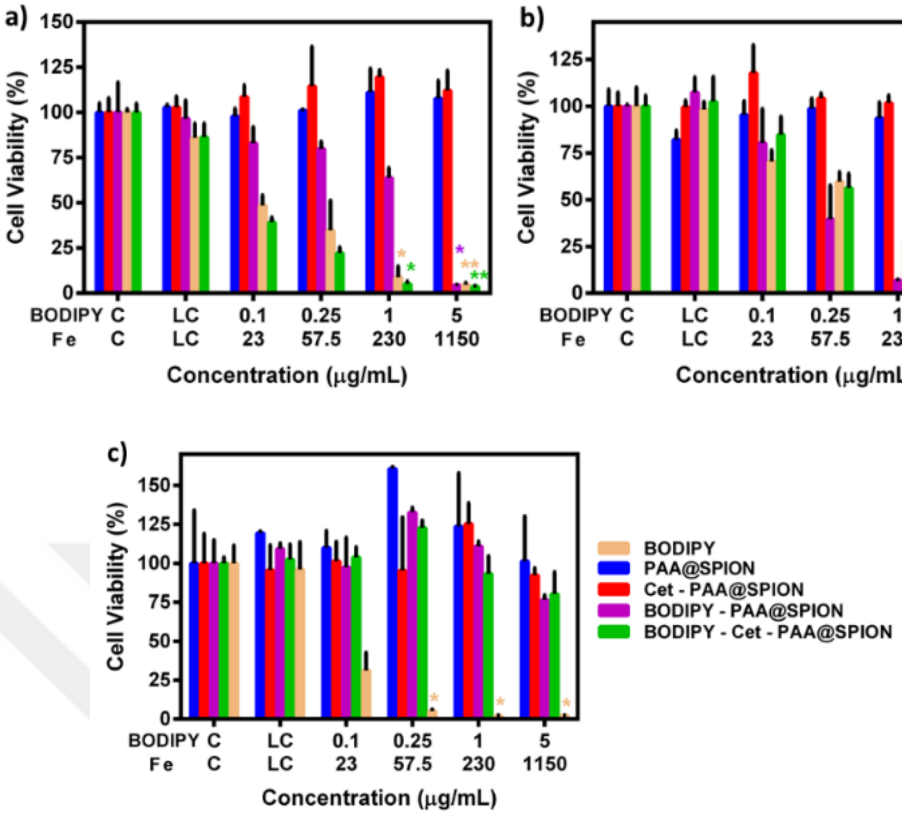

Figure 4.7. Dose dependent cell viability of a) HT29, b) SW480 and c) L929 cells treated with free BODIPY, PAA@SPION, Cet-PAA@SPION, BODIPY-PAA@SPION and BODIPY-Cet-PAA@SPION after 4 h incubation. Untreated cells were used as control. Data are expressed as mean ± SD (n=3).

In the case of HT29, no significant toxicity was observed with BODIPY-PAA@SPION between 0.1-1 μg BODIPY/mL. The viability of HT29 cells treated with free BODIPY and BODIPY-Cet-PAA@SPION sharply decreased to 48.5 and 39.1 % at 0.1 μg/mL, respectively. BODIPY-Cet-PAA@SPION showed higher toxicity than free BODIPY at mid doses, which can be attributed to high EGFR expression in HT29 cells (Figure 4.7a). All agents caused almost complete cell death at 5 μg BODIPY/mL in SW480 cells. In the case of SW480, both BODIPY-PAA@SPION and BODIPY-Cet-PAA@SPION induced higher phototoxicity compared to free BODIPY at 1 μg BODIPY/mL concentration (Figure 4.7b). The cell viability was 26.9, 6.85 and 8.7 % for free BODIPY, BODIPY-PAA@SPION and BODIPY-Cet-PAA@SPION, respectively. However, no significant differences between BODIPY-PAA@SPION and BODIPY-Cet-PAA@SPION was detected, which is expected since Cet would not dramatically enhance accumulation of BODIPY-Cet-PAA@SPION in low EGFR-expressing SW480 cells.

Almost complete cell death was observed with all agents at 5 µg BODIPY/mL. The phototoxicity of PAA@SPION was not significant at SW480 and HT29 cell lines; however, increased cellular uptake of BODIPY with NPs could be the reason for enhanced PDT with BODIPY-PAA@SPION and BODIPY-Cet-PAA@SPION. Another critical result was the phototoxicity of agents on healthy cell line, L929, which showed that BODIPY-PAA@SPION and BODIPY-Cet-PAA@SPION did not cause any reduction, while free BODIPY sharply decreased the cell viability to 31.2 % even at 0.1 µg BODIPY/mL (Figure 4.7c). Furthermore, the cell viability was 5, 2 and 2.3 % at 0.25, 1 and 5 µg BODIPY/mL, respectively.

4.3.6 ROS generation

Intracellular ROS generation of free BODIPY and BODIPY-Cet-PAA@SPION were further investigated by using a cell permeable ROS sensor, DCFH-DA in free body and BODIPY-Cet-PAA@SPION treated SW480 and HT29 cells after 5 min LED irradiation. In the case of the SW480 cell line, free BODIPY and BODIPY-Cet-PAA@SPION generated similar ROS levels in a concentration-dependent manner reaching about 69-fold at the highest concentration. BODIPY-Cet-PAA@SPION produced a 58-fold increase while the fold increase was 32 with free BODIPY at 1 µg/mL BODIPY concentration (Figure 4.8a). At 0.1, 0.25, 1 and 5 µg BODIPY/mL doses 26.8, 26.7, 61.3 and 105.7-fold increase for free BODIPY and 43.7, 61.2, 117 and 145.5-fold increase for BODIPY-Cet-PAA@SPION was recorded with respect to control in HT29 cell line (Figure 4.8b). In HT29 cell line, high uptake of BODIPY-Cet-PAA@SPION due to high EGFR expression caused more ROS generation than free BODIPY, which is in good correlation with imaging results.

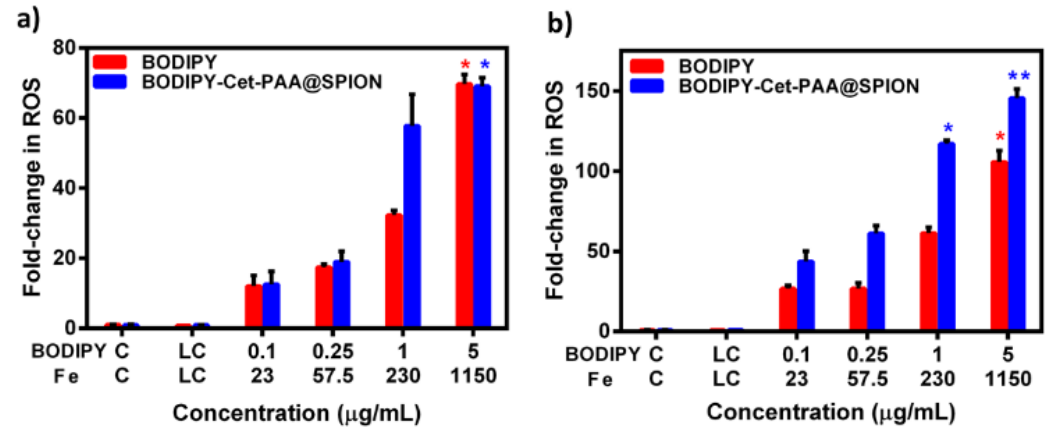

Figure 4.8. Monitoring ROS production in free BODIPY and BODIPY-Cet-PAA@SPION treated a) SW480 and b) HT29 cells by using DCFH-DA after 5 min LED irradiation. C: control, LC: light control.

4.4 Conclusion

Enhanced selectivity towards EGFR(+) colon cancer cells and improved phototoxicity of BODIPY were achieved using Cet-PAA@SPION as a safe delivery vehicle. Most importantly, severe phototoxicity of BODIPY on healthy cell lines was eliminated by this unique nanoparticle design. Short incubation time (4 h) and low dose of BODIPY for effective and selective phototoxicity are also significant advantages of the system. Although the idea was demonstrated on EGFR(+) colon cancer cells, same particles may be adopted for the treatment of other EGFR(+) tumors or the antibody may be changed to target different tumor specific receptors.

Chapter 5:
PERSPECTIVES FOR FUTURE STUDIES: POTENTIAL OF CARBON NANOPARTICLES IN BIOMEDICAL APPLICATIONS

5.1 Introduction

Carbon-based nanoparticles have risen as an alternative to other QDs in biomedical applications for a couple of decades. Nevertheless, using them in photothermal and photodynamic therapy is still in progress.

In 2012, Tao et al. introduced CDs as a good fluorescence contrast agent and this study was performed at an excitation of 595 nm (Tao et al., 2011). In the following years, as an addition to bioimaging applications, the sensing ability of CDs was discovered. Li et al. showed their potential in genetic material detection (Li et al., 2011; Du et al., 2013). This example opened new ways not only for bioimaging but also medical therapy. In terms of invasive methods for the treatment of cancer, phototherapy-based applications have minimal cost for the patients (Zhou et al., 2019). However, the most promising CDs are NIR light-responsive ones due to their longer penetration depth in tissue and at first, synthesizing this kind of CDs for photothermal and photodynamic therapies was a difficult task.

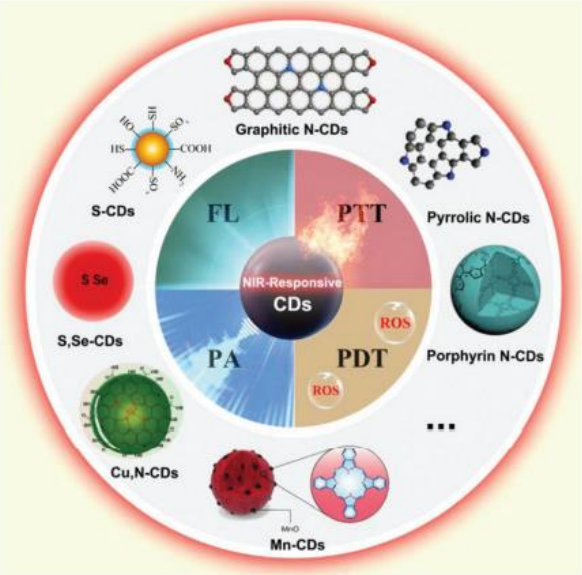

Figure 5.1. NIR light-responsive CDs and their potential applications (Zhou et al., 2019).

The challenge was obtaining aqueous red or NIR light-responsive CDs since water as a media generally causes to blue shift. Ge et al. successfully produced red-emitting CDs in aqueous media for photothermal therapy and worked with HeLa cells, but cytotoxicity was a problem (Ge et al., 2015). In 2016, Li et al. applied post-treatment to their hydrothermally synthesized citric acid and urea-based CDs. They placed CDs under 60% humidity for seven days which shifted the blue emission to red and provided 50% light to heat conversion efficiency (Li et al., 2016).

After a year, Lan et al. published an article about the recently discovered feature of NIR light-responsive CDs called two-photon excitation and that accelerated the studies on CD-based PDT and PTT (Lan et al., 2017).

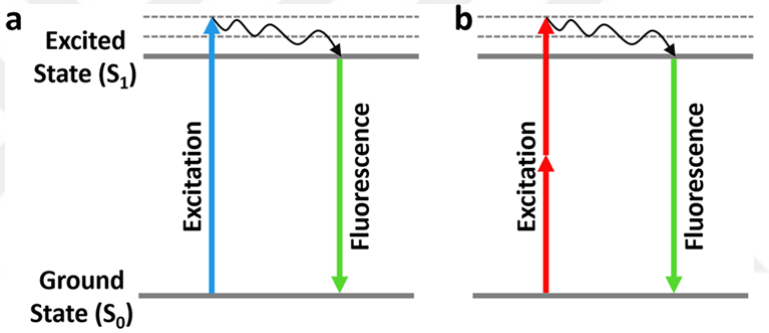

Figure 5.2. Schematic illustration of a) single-photon b) two-photon excitation mechanisms (Lan et al., 2017).

Although two-photon excited NIR-emissive CDs may show one of the highest ratios of light to heat efficiency in the literature (~58.2%), most of them include co-doping of sulfur or selenium elements which increase the cytotoxicity (Lan et al., 2017; Bai et al., 2021).

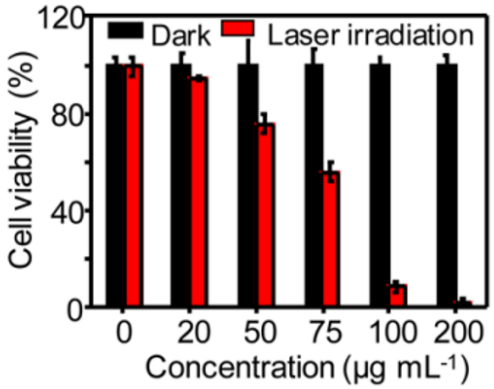

Figure 5.3. The viability of MCF-7 cells was incubated with different concentrations of the R-CDs before and after laser irradiation for 10 min (Sun et al., 2016).

Two-photon excited red-emissive or NIR-emissive CDs were used in PDT as well. As seen in Figure 5.3 Sun et al. showed a significant decrease in viability of MCF-7 cells treated with red CDs after 10 min laser irradiation (671 nm laser, 2.5 W cm^{-2}) (Sun et al., 2016).

In this chapter, knowledge on the synthesis of red-emissive CDs from Chapter 2 and the use of nanoparticles in phototherapy from Chapter 4 will be combined and the potential of these red CDs (Chen et al., 2017) as phototherapy agents will be investigated as the first step for future studies.

5.2 Experimental

5.2.1 Materials

Ethanol, NaOH pellets, hydrochloric acid (fuming 37%) and p-phenylenediamine were purchased from Sigma (Missouri, U.S.). Phosphoric acid was obtained from Merck (Darmstadt, Germany). Pure water (18.2 mΩ, RephiLe Bioscience and Technology, Shanghai, China) was used. RPMI, trypsin EDTA and penicillin-streptomycin solutions were purchased from Multicell, Wisent Inc. (QC, Canada). Fetal bovine serum (FBS) was obtained from Capricorn Scientific GmbH (Ebsdorfergrund, Germany). Phosphate-buffered saline (PBS) and thiazolyl blue tetrazolium bromide (MTT) were provided by Biomatik Corp. (ON, Canada). 96-well plates were purchased from Nest Biotechnology Co., Ltd (Wuxi, China). Only ultra-pure water (18.2 MΩ, RephiLe Bioscience and Technology, Shanghai, China) was used when needed.

5.2.2 Synthesis

Firstly, p-phenylenediamine (0.1 g) was dissolved in 20 mL distilled water which includes 1 mL phosphoric acid and then the suspension was transferred into a Teflon-lined autoclave (45 mL) and placed into the oven under 180°C for 24 h. Obtaining dark red suspensions were filtered 0.22 µm microporous membrane to remove large size clusters. The solution was neutralized with 0.1 M NaOH. Afterwards, this suspension was precipitated in the centrifugal tube (5000 rpm, 25 min). The precipitate was washed off with cold EtOH and distilled water respectively to remove by-products. The final carbon dot was produced by dissolving the precipitate in 0.1 M HCl.

5.2.3 Characterization

UV-Visible spectra were obtained by using a Shimadzu UV-Vis-NIR spectrometer in the 300-800 nm. Photoluminescence spectra were measured by using Agilent Cary Eclipse PL.

5.2.4 Cell culture and conditions

A549 cells were culture in RPMI medium, respectively supplemented with 10 % (v/v) fetal bovine serum and 1 % (v/v) penicillin streptomycin and incubated in a 5 % CO_2 humidified incubator at 37 °C.

5.2.5 Cytotoxicity assays

The cytotoxicity of CD07 in A549 cells were examined using MTT ((Thiazolyl blue tetrazolium bromide (3-(4, 5-dimethylthiazol-2-yl)-2, 5-diphenyltetrazolium bromide)) assay protocol. The density of seeded cells for this assay was $1x10^4$ cells per well. And 96 well plates were used during the 24 h incubation. Injection of different concentrations of CD07 into cells was performed in a fresh culture medium. 50 µL of MTT (5 mg/mL in PBS) solution and 150 µL fresh medium were added to cells after 4 h incubation. Finally, the formation of purple formazan crystals by the viable cells was dissolved with the addition of DMSO:Ethanol (1:1 v/v). Reading absorbance was 570 nm and reference was 650 nm at Synergy H1 (Biotek Instruments). The results were analyzed by using

GraphPad Prism 8 software (California, U.S). Relative cell viability was found by dividing absorbance of sample to absorbance of control and multiplied by 100.

5.2.6 In vitro laser irradiation

A549 cells incubated with particles for 24 hours were irradiated with 0.78 W/cm^2 output 640 nm laser for 10 min. Irradiation was applied from the bottom of the plate.

5.2.7 Detection of singlet oxygen generation (SOSG)

Photosensitized $^1O_2$ generation of CD07 was first investigated in oxygen saturated solutions (PBS, pH 7.4, 1% DMSO) by utilizing a $^1O_2$-selective water-soluble trap molecule, Singlet Oxygen Sensor Green (SOSG). SOSG emission is quenched because of an effective PeT mechanism and its characteristic green emission at 530 nm can only be restored in the presence of $^1O_2$. Irradiation of CD07 with a 635 nm red LED light source for 1 min resulted in a turn-on response in SOSG emission, suggesting that these agents can trigger $^1O_2$ formation upon excitation.

5.2.8 NIR irradiation of aqueous solutions

A solution of CD07 at 200 µg/mL was irradiated with a 635 nm red LED light source for 5 min and temperature change was recorded by probe simultaneously.

5.3 Results and Discussion

5.3.1 Dark toxicity of CD in A549 cell line

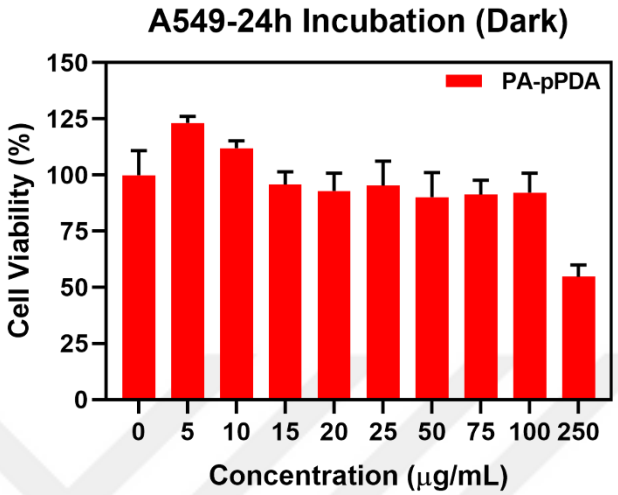

Figure 5.4. Viability of A549 cells treated with different concentrations of CD07 after 24 h incubation in the dark.

Figure 5.4 shows that CD07 has quite a low cytotoxicity, even at 100 ug/mL, cell viability is around 90%. This provides better dosage control and tunable concentration for applications.

5.3.2 Phototoxicity of CD in A549 cell line

A549 cells treated with CD07 and subjected to 10 min irradiation at 640 nm with a power density of 0.78 W cm^{-2} showed about 25% loss in viability within the studied concentration range (Figure 5.5). This is a very promising result considering the low power intensity used in the study and the lack of S or Se in the composition of CD07. Combination of this CD with other photosensitizers or toxic chemotherapeutic agents may provide strong therapeutic effects.

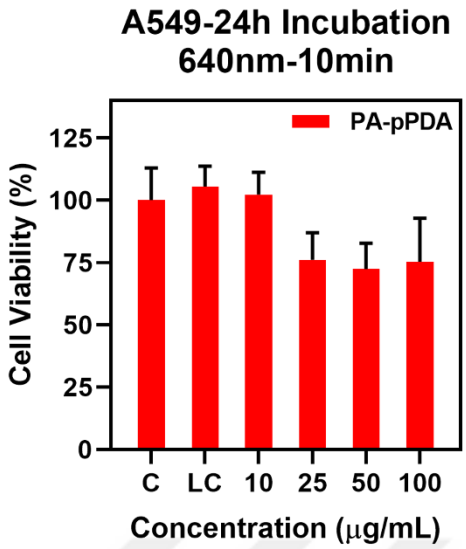

Figure 5.5. Viability of A549 cells treated with different concentrations of CD07 after 24 h incubation at 640 nm laser irradiation for 10 min. Untreated cells were used as a control.

5.3.3 Origin of the phototoxicity of CD07

Most photosensitizers produce singlet oxygen upon excitation, which helps to produce reactive oxygen species causing cell death. However, no singlet oxygen production was detected in the case of CD07 as seen in Figure 5.6.

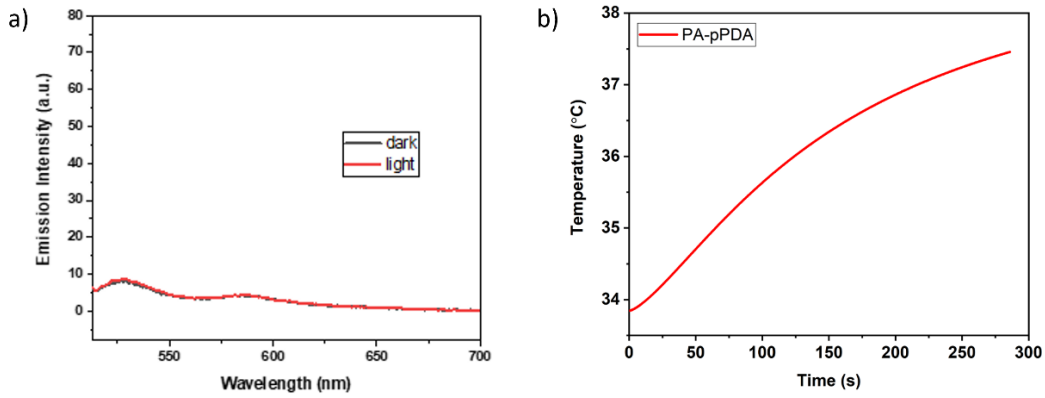

Figure 5.6. CD07 (200 µg/mL) a) SOSG emission at dark and light b) temperature increase (Red LED)

On the other hand, about 3.5 °C temperature increase in the solution of CD07 was detected when irradiated 10 min, which is not enough for thermal ablation, but it is close

to mild hyperthermia which may enhance the sensitivity of tumor cells to conventional therapies such as chemotherapy.

One important point here is the fact that in vitro phototoxicity studies performed with a 640 nm laser but detection of singlet oxygen and temperature increase was tested with a 635 nm red LED irradiation. Power density of LED is lower than laser, so these experiments should be repeated with the laser.

5.3.4 Two-photon excitation potential of CDs

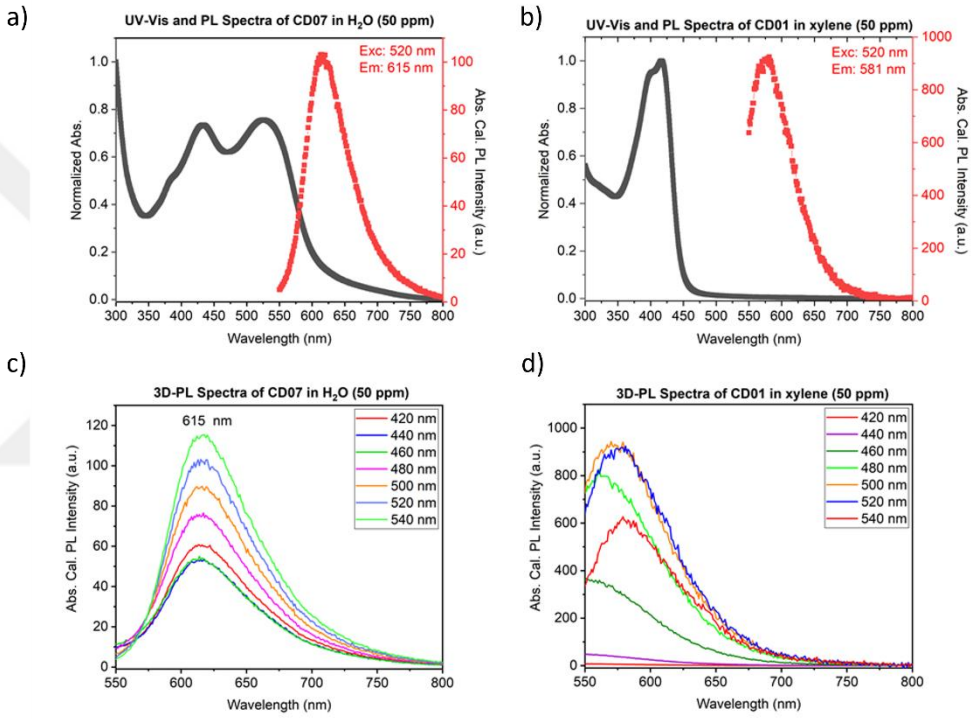

Figure 5.7. UV-Vis and PL spectra of a) CD07 b) CD01X, excitation dependent emission spectra of c) CD07 d) CD01X.

Light to heat conversion efficiency of CDs with two-photon absorption was reported as highest in the literature (Lan et al., 2017; Bai et al., 2021). Therefore, two-photon excitation of CD07 was investigated but such a characteristic was not detected (Figure 5.7a). However, a yellow emissive CD, CD01, showed a different behaviour. As seen in Figure 5.7b, there is a highly intense emission peak when CD01 was excited at 520 nm despite the lack of any significant absorption at 520 nm. This may be because of the two-photon excitation characteristic of CD01. However, more comprehensive experiments should be performed to understand this property better.

5.3.5 Intracellular NO sensing potential of CDs

In addition to cancer therapy applications, CD07 may be an ideal nanoparticle for intracellular NO sensing applications. It is important to sense NO amount in the cellular matrix since it takes a role in the cell death mechanism. There is only one study in the literature that was able to do that with carbon nanotubes (Ulissi et al., 2014).

As shown in Figure 3.16, CD07 is a pH-dependent carbon dot and that makes it ideal for pH-related sensing. With this insight, CD07 was tested for NO concentration dependent detection by Gözde Demirci and Ahmet Ferid Fırat. And initial results seen in Figure 5.8 are highly promising to take a step further and use CD07 for intracellular NO detection.

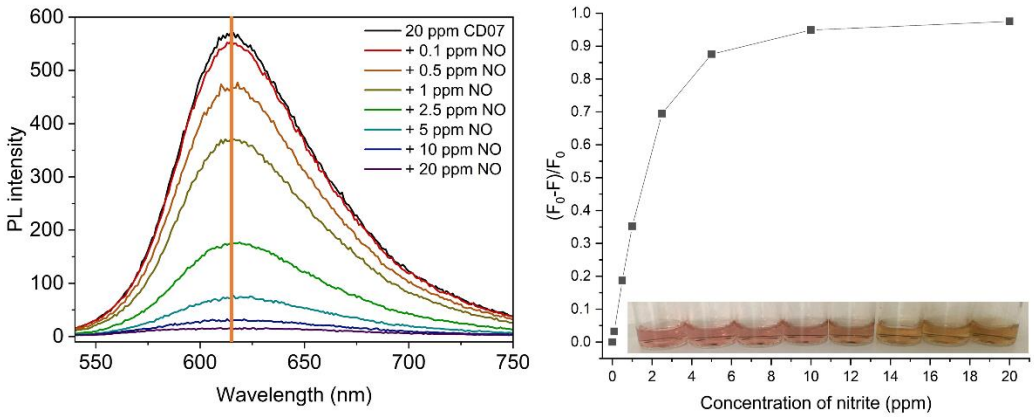

Figure 5.8. Concentration dependent NO detection with CD07 via PL spectra.

5.4 Conclusion

Laser irradiation of cells treated with CD07 provides a ~30% decrease in cell viability in the A549 cell line after 10 min 640 nm laser irradiation. However, this could not be confirmed as PDT or PTT effect since solution experiments were performed with low power LED irradiation. This phototoxicity may be coupled with other therapeutic methods in future studies. Also, two-photon excitation characteristics for two different CDs; CD07 and CD01 was investigated. In contrast to literature red CD did not show two-photon excitation but yellow emitting CD01 did, which may be utilized for medical purposes in the future. Last but not least, these CDs may be utilized in many sensing applications, including pH sensing or NO sensing.

BIBLIOGRAPHY

Adhikari, R., Jin, L., Navarro-Pardo, F., Benetti, D., AlOtaibi, B., Vanka, S., Zhao, H., Mi, Z., Vomiero, A., & Rosei, F. (2016). High efficiency, Pt-free photoelectrochemical cells for solar hydrogen generation based on “giant” quantum dots. *Nano Energy*, *27*, 265–274. https://doi.org/10.1016/j.nanoen.2016.07.010

Alexiou, C., Arnold, W., Klein, R. J., Parak, F. G., Hulin, P., Bergemann, C., Erhardt, W., Wagenpfeil, S., & Lübbe, A. S. (2000). Locoregional cancer treatment with magnetic drug targeting. *Cancer research*, *60*(23), 6641–6648.

Allison, E., & Mandler, B. (2018). Petroleum and the Environment. *Van Haren Publishing*.

Atilgan, S., Ekmekci, Z., Dogan, A. L., Guc, D., & Akkaya, E. U. (2006). Water soluble distyryl-boradiazaindacenes as efficient photosensitizers for photodynamic therapy. *Chemical Communications*, *42*, 4398. https://doi.org/10.1039/b612347c

Bai, Y., Zhao, J., Wang, S., Lin, T., Ye, F., & Zhao, S. (2021). Carbon Dots with Absorption Red-Shifting for Two-Photon Fluorescence Imaging of Tumor Tissue pH and Synergistic Phototherapy. *ACS Applied Materials & Interfaces*, *13*(30), 35365–35375. https://doi.org/10.1021/acsami.1c08076

Bian, S., Shen, C., Hua, H., Zhou, L., Zhu, H., Xi, F., Liu, J., & Dong, X. (2016). One-pot synthesis of sulfur-doped graphene quantum dots as a novel fluorescent probe for highly selective and sensitive detection of lead(ii). *RSC Advances*, *6*(74), 69977–69983. https://doi.org/10.1039/c6ra10836a

Bilici, K., Muti, A., Demir Duman, F., Sennaroğlu, A., & Yağcı Acar, H. (2018). Investigation of the factors affecting the photothermal therapy potential of small iron oxide nanoparticles over the 730–840 nm spectral region. *Photochemical & Photobiological Sciences*, *17*(11), 1787–1793. https://doi.org/10.1039/c8pp00203g

Chahal, S., Yousefi, N., & Tufenkji, N. (2020). Green Synthesis of High Quantum Yield Carbon Dots from Phenylalanine and Citric Acid: Role of Stoichiometry and Nitrogen Doping. *ACS Sustainable Chemistry & Engineering*, *8*(14), 5566–5575. https://doi.org/10.1021/acssuschemeng.9b07463

Chen, J., Wei, J. S., Zhang, P., Niu, X. Q., Zhao, W., Zhu, Z. Y., Ding, H., & Xiong, H. M. (2017). Red-Emissive Carbon Dots for Fingerprints Detection by Spray Method: Coffee Ring Effect and Unquenched Fluorescence in Drying Process. *ACS Applied Materials & Interfaces*, *9*(22), 18429–18433. https://doi.org/10.1021/acsami.7b03917

Correa-Baena, J. P., Abate, A., Saliba, M., Tress, W., Jesper Jacobsson, T., Grätzel, M., & Hagfeldt, A. (2017). The rapid evolution of highly efficient perovskite solar cells. *Energy & Environmental Science*, *10*(3), 710–727. https://doi.org/10.1039/c6ee03397k

Crista, D. M. A., Esteves Da Silva, J. C. G., & Pinto Da Silva, L. (2020). Evaluation of Different Bottom-up Routes for the Fabrication of Carbon Dots. *Nanomaterials*, *10*(7), 1316. https://doi.org/10.3390/nano10071316

Deng, Y., Zhao, D., Chen, X., Wang, F., Song, H., & Shen, D. (2013). Long lifetime pure organic phosphorescence based on water soluble carbon dots. *Chemical Communications*, *49*(51), 5751. https://doi.org/10.1039/c3cc42600a

Ding, H., Yu, S. B., Wei, J. S., & Xiong, H. M. (2015). Full-Color Light-Emitting Carbon Dots with a Surface-State-Controlled Luminescence Mechanism. *ACS Nano*, *10*(1), 484–491. https://doi.org/10.1021/acsnano.5b05406

Ding, H., Zhou, X. X., Wei, J. S., Li, X. B., Qin, B. T., Chen, X. B., & Xiong, H. M. (2020). Carbon dots with red/near-infrared emissions and their intrinsic merits for biomedical applications. *Carbon*, *167*, 322–344. https://doi.org/10.1016/j.carbon.2020.06.024

Ding, H., Wei, J. S., Zhang, P., Zhou, Z. Y., Gao, Q. Y., & Xiong, H. M. (2018). Solvent-Controlled Synthesis of Highly Luminescent Carbon Dots with a Wide Color Gamut and Narrowed Emission Peak Widths. *Small*, *14*(22), 1800612. https://doi.org/10.1002/smll.201800612

Ding, H., Zhou, X. X., Zhang, Z. H., Zhao, Y. P., Wei, J. S., & Xiong, H. M. (2021). Large scale synthesis of full-color emissive carbon dots from a single carbon source by a solvent-free method. *Nano Research*. Published. https://doi.org/10.1007/s12274-021-3891-0

Ding, H., Wei, J. S., Zhong, N., Gao, Q. Y., & Xiong, H. M. (2017). Highly Efficient Red-Emitting Carbon Dots with Gram-Scale Yield for Bioimaging. *Langmuir*, *33*(44), 12635–12642. https://doi.org/10.1021/acs.langmuir.7b02385

Du, F., Min, Y., Zeng, F., Yu, C., & Wu, S. (2013). A Targeted and FRET-Based Ratiometric Fluorescent Nanoprobe for Imaging Mitochondrial Hydrogen Peroxide in Living Cells. *Small*, *10*(5), 964–972. https://doi.org/10.1002/smll.201302036

Ertem, E., Bekdemir, A., Atilgan, A., & Akkaya, E. U. (2014). Near-IR absorbing Bodipy functionalized SPIONs: A potential magnetic nanoplatform for diagnosis and therapy. *Pure and Applied Chemistry*, *86*(6), 899–903. https://doi.org/10.1515/pac-2013-1114

Escudero, A., Carrillo-Carrión, C., Castillejos, M. C., Romero-Ben, E., Rosales-Barrios, C., & Khiar, N. (2021). Photodynamic therapy: photosensitizers and

nanostructures. *Materials Chemistry Frontiers*, *5*(10), 3788–3812. https://doi.org/10.1039/d0qm00922a

Esfandiari, N., Bagheri, Z., Ehtesabi, H., Fatahi, Z., Tavana, H., & Latifi, H. (2019). Effect of carbonization degree of carbon dots on cytotoxicity and photo-induced toxicity to cells. *Heliyon*, *5*(12), e02940. https://doi.org/10.1016/j.heliyon.2019.e02940

Estelrich, J., & Busquets, M. (2018). Iron Oxide Nanoparticles in Photothermal Therapy. *Molecules*, *23*(7), 1567. https://doi.org/10.3390/molecules23071567

Fang, Q., Dong, Y., Chen, Y., Lu, C. H., Chi, Y., Yang, H. H., & Yu, T. (2017). Luminescence origin of carbon based dots obtained from citric acid and amino group-containing molecules. *Carbon*, *118*, 319–326. https://doi.org/10.1016/j.carbon.2017.03.061

Franco, C. A., Candela, C. H., Gallego, J., Marin, J., Patiño, L. E., Ospina, N., Patiño, E., Molano, M., Villamil, F., Bernal, K. M., Lopera, S. H., Franco, C. A., & Cortés, F. B. (2020). Easy and Rapid Synthesis of Carbon Quantum Dots from Mortiño (Vaccinium Meridionale Swartz) Extract for Use as Green Tracers in the Oil and Gas Industry: Lab-to-Field Trial Development in Colombia. *Industrial & Engineering Chemistry Research*, *59*(25), 11359–11369. https://doi.org/10.1021/acs.iecr.0c01194

Fuel Additives: Use and Benefits. (2013). *ATC Technical Committee of Petroleum Additive Manufacturers in Europe*. https://www.atc-europe.org/public/Doc113%202013-11-20.pdf

Ge, J., Jia, Q., Liu, W., Guo, L., Liu, Q., Lan, M., Zhang, H., Meng, X., & Wang, P. (2015). Red-Emissive Carbon Dots for Fluorescent, Photoacoustic, and Thermal Theranostics in Living Mice. *Advanced Materials*, *27*(28), 4169–4177. https://doi.org/10.1002/adma.201500323

Geng, B., Yang, D., Pan, D., Wang, L., Zheng, F., Shen, W., Zhang, C., & Li, X. (2018b). NIR-responsive carbon dots for efficient photothermal cancer therapy at low power densities. *Carbon*, *134*, 153–162. https://doi.org/10.1016/j.carbon.2018.03.084

Ghosh, D., Sarkar, K., Devi, P., Kim, K. H., & Kumar, P. (2021). Current and future perspectives of carbon and graphene quantum dots: From synthesis to strategy for building optoelectronic and energy devices. *Renewable and Sustainable Energy Reviews*, *135*(July 2020), 110391. https://doi.org/10.1016/j.rser.2020.110391

Guo, Y., Zhang, J., Zhang, W., & Hu, D. (2019). Green fluorescent carbon quantum dots functionalized with polyethyleneimine, and their application to aptamer-based determination of thrombin and ATP. *Microchimica Acta*, *186*(11). https://doi.org/10.1007/s00604-019-3874-y

Han, B., Wang, W., Wu, H., Fang, F., Wang, N., Zhang, X., & Xu, S. (2012). Polyethyleneimine modified fluorescent carbon dots and their application in cell labeling. *Colloids and Surfaces B: Biointerfaces, 100*, 209–214. https://doi.org/10.1016/j.colsurfb.2012.05.016

Harisinghani, M. G., Barentsz, J., Hahn, P. F., Deserno, W. M., Tabatabaei, S., van de Kaa, C. H., de la Rosette, J., & Weissleder, R. (2003). Noninvasive Detection of Clinically Occult Lymph-Node Metastases in Prostate Cancer. *New England Journal of Medicine, 348*(25), 2491–2499. https://doi.org/10.1056/nejmoa022749

Hayashi, K., Nakamura, M., Sakamoto, W., Yogo, T., Miki, H., Ozaki, S., Abe, M., Matsumoto, T., & Ishimura, K. (2013). Superparamagnetic Nanoparticle Clusters for Cancer Theranostics Combining Magnetic Resonance Imaging and Hyperthermia Treatment. *Theranostics*, *3*(6), 366–376. https://doi.org/10.7150/thno.5860

Jaque, D., Martínez Maestro, L., del Rosal, B., Haro-Gonzalez, P., Benayas, A., Plaza, J. L., Martín Rodríguez, E., & García Solé, J. (2014). Nanoparticles for photothermal therapies. *Nanoscale*, *6*(16), 9494–9530. https://doi.org/10.1039/c4nr00708e

Jia, Q., Zhao, Z., Liang, K., Nan, F., Li, Y., Wang, J., Ge, J., & Wang, P. (2020). Recent advances and prospects of carbon dots in cancer nanotheranostics. *Materials Chemistry Frontiers*, *4*(2), 449–471. https://doi.org/10.1039/c9qm00667b

Jiang, K., Wang, Y., Cai, C., & Lin, H. (2018). Conversion of Carbon Dots from Fluorescence to Ultralong Room-Temperature Phosphorescence by Heating for Security Applications. *Advanced Materials*, *30*(26), 1–8. https://doi.org/10.1002/adma.201800783

Jiang, K., Sun, S., Zhang, L., Lu, Y., Wu, A., Cai, C., & Lin, H. (2015). Red, Green, and Blue Luminescence by Carbon Dots: Full-Color Emission Tuning and Multicolor Cellular Imaging. *Angewandte Chemie*, *127*(18), 5450–5453. https://doi.org/10.1002/ange.201501193

Kamkaew, A., Lim, S. H., Lee, H. B., Kiew, L. V., Chung, L. Y., & Burgess, K. (2013). BODIPY dyes in photodynamic therapy. *Chem. Soc. Rev.*, *42*(1), 77–88. https://doi.org/10.1039/c2cs35216h

Karaman, O., Almammadov, T., Emre Gedik, M., Gunaydin, G., Kolemen, S., & Gunbas, G. (2019). Mitochondria-Targeting Selenophene-Modified BODIPY-Based Photosensitizers for the Treatment of Hypoxic Cancer Cells. *ChemMedChem, 14*(22), 1879–1886. https://doi.org/10.1002/cmdc.201900380

Kessel, D., & Oleinick, N. L. (2018). Cell Death Pathways Associated with Photodynamic Therapy: An Update. *Photochemistry and Photobiology*, *94*(2), 213–218. https://doi.org/10.1111/php.12857

Khan, Z. M., Saifi, S., Shumaila, Aslam, Z., Khan, S. A., & Zulfequar, M. (2020). A facile one step hydrothermal synthesis of carbon quantum dots for label -free fluorescence sensing approach to detect picric acid in aqueous solution. *Journal of Photochemistry and Photobiology A: Chemistry, 388*, 112201. https://doi.org/10.1016/j.jphotochem.2019.112201

Lan, M., Zhao, S., Liu, W., Lee, C., Zhang, W., & Wang, P. (2019). Photosensitizers for Photodynamic Therapy. *Advanced Healthcare Materials, 8*(13), 1900132. https://doi.org/10.1002/adhm.201900132

Lan, M., Zhao, S., Zhang, Z., Yan, L., Guo, L., Niu, G., Zhang, J., Zhao, J., Zhang, H., Wang, P., Zhu, G., Lee, C. S., & Zhang, W. (2017). Two-photon-excited near-infrared emissive carbon dots as multifunctional agents for fluorescence imaging and photothermal therapy. *Nano Research, 10*(9), 3113–3123. https://doi.org/10.1007/s12274-017-1528-0

Landrigan P. J. (2002). The worldwide problem of lead in petrol. *Bulletin of the World Health Organization, 80*(10), 768

Lee, C., Kwon, W., Beack, S., Lee, D., Park, Y., Kim, H., Hahn, S. K., Rhee, S. W., & Kim, C. (2016). Biodegradable nitrogen-doped carbon nanodots for non-invasive photoacoustic imaging and photothermal therapy. *Theranostics, 6*(12), 2196–2208. https://doi.org/10.7150/thno.16923

Lee, T., Won, S., Park, Y., & Kwon, W. (2021). Oxygen-less Carbon Nanodots with an Absolute Quantum Yield of 80% for Display Applications. *ACS Applied Nano Materials, 4*(3), 2462–2469. https://doi.org/10.1021/acsanm.0c03011

Li, D., Han, D., Qu, S. N., Liu, L., Jing, P. T., Zhou, D., Ji, W. Y., Wang, X. Y., Zhang, T. F., & Shen, D. Z. (2016). Supra-(carbon nanodots) with a strong visible to near-infrared absorption band and efficient photothermal conversion. *Light: Science & Applications, 5*(7), e16120. https://doi.org/10.1038/lsa.2016.120

Li, H., Kang, Z., Liu, Y., & Lee, S. T. (2012). Carbon nanodots: synthesis, properties and applications. *Journal of Materials Chemistry, 22*(46), 24230. https://doi.org/10.1039/c2jm34690g

Li, H., Zhang, Y., Wang, L., Tian, J., & Sun, X. (2011). Nucleic acid detection using carbon nanoparticles as a fluorescent sensing platform. *Chem. Commun., 47*(3), 961–963. https://doi.org/10.1039/c0cc04326e

Li, L., & Dong, T. (2018). Photoluminescence tuning in carbon dots: surface passivation or/and functionalization, heteroatom doping. *Journal of Materials Chemistry C, 6*(30), 7944–7970. https://doi.org/10.1039/c7tc05878k

Lin, S., Lin, C., He, M., Yuan, R., Zhang, Y., Zhou, Y., Xiang, W., & Liang, X. (2017). Solvatochromism of bright carbon dots with tunable long-wavelength emission from green to red and their application as solid-state materials for warm WLEDs. *RSC Advances, 7*(66), 41552–41560. https://doi.org/10.1039/c7ra07736j

Liu, C., Bao, L., Tang, B., Zhao, J. Y., Zhang, Z. L., Xiong, L. H., Hu, J., Wu, L. L., & Pang, D. W. (2016). Fluorescence-Converging Carbon Nanodots-Hybridized Silica Nanosphere. *Small, 12*(34), 4702–4706. https://doi.org/10.1002/smll.201503958

Liu, C., Zhang, P., Zhai, X., Tian, F., Li, W., Yang, J., Liu, Y., Wang, H., Wang, W., & Liu, W. (2012). Nano-carrier for gene delivery and bioimaging based on carbon dots with PEI-passivation enhanced fluorescence. *Biomaterials, 33*(13), 3604–3613. https://doi.org/10.1016/j.biomaterials.2012.01.052

Liu, J., Liu, Y., Liu, N., Han, Y., Zhang, X., Huang, H., Lifshitz, Y., Lee, S. T., Zhong, J., & Kang, Z. (2015). Water splitting. Metal-free efficient photocatalyst for stable visible water splitting via a two-electron pathway. *Science (New York, N.Y.), 347*(6225), 970–974. https://doi.org/10.1126/science.aaa3145

Liu, H., Li, Z., Sun, Y., Geng, X., Hu, Y., Meng, H., Ge, J., & Qu, L. (2018). Synthesis of Luminescent Carbon Dots with Ultrahigh Quantum Yield and Inherent Folate Receptor-Positive Cancer Cell Targetability. *Scientific Reports, 8*(1), 1–8. https://doi.org/10.1038/s41598-018-19373-3

Liu, Q. W., Liu, Q. Y., Li, J. Y., Wei, L., Ren, K. K., Zhang, X. C., Ding, T., Xiao, L., Zhang, W. J., Wu, H. Y., & Xin, H. B. (2018). Therapeutic efficiency of human amniotic epithelial stem cell-derived functional hepatocyte-like cells in mice with acute hepatic failure. *Stem cell research & therapy*, *9*(1), 321. https://doi.org/10.1186/s13287-018-1063-2

Liu, J., Li, D., Zhang, K., Yang, M., Sun, H., & Yang, B. (2018). One-Step Hydrothermal Synthesis of Nitrogen-Doped Conjugated Carbonized Polymer Dots with 31% Efficient Red Emission for In Vivo Imaging. *Small, 14*(15), 1703919. https://doi.org/10.1002/smll.201703919

Loo, A. H., Sofer, Z., Bouša, D., Ulbrich, P., Bonanni, A., & Pumera, M. (2016). Carboxylic Carbon Quantum Dots as a Fluorescent Sensing Platform for DNA Detection. *ACS Applied Materials and Interfaces, 8*(3), 1951–1957. https://doi.org/10.1021/acsami.5b10160

Lu, S., Sui, L., Liu, J., Zhu, S., Chen, A., Jin, M., & Yang, B. (2017). Near-Infrared Photoluminescent Polymer-Carbon Nanodots with Two-Photon Fluorescence. *Advanced Materials, 29*(15), 1603443. https://doi.org/10.1002/adma.201603443

Lungwitz, U., Breunig, M., Blunk, T., & Göpferich, A. (2005). Polyethylenimine-based non-viral gene delivery systems. *European Journal of Pharmaceutics and Biopharmaceutics, 60*(2), 247–266. https://doi.org/10.1016/j.ejpb.2004.11.011

Mauro, N., Utzeri, M. A., Drago, S. E., Buscarino, G., Cavallaro, G., & Giammona, G. (2020). Carbon Nanodots as Functional Excipient to Develop Highly Stable and Smart PLGA Nanoparticles Useful in Cancer Theranostics. *Pharmaceutics*, *12*(11), 1012. https://doi.org/10.3390/pharmaceutics12111012

Mehraban, N., & Freeman, H. (2015). Developments in PDT Sensitizers for Increased Selectivity and Singlet Oxygen Production. *Materials, 8*(7), 4421–4456. https://doi.org/10.3390/ma8074421

Pan, Y. Y., Yin, W. M., Meng, R. J., Guo, Y. R., Zhang, J. G., & Pan, Q. J. (2021). Productive preparation of N-doped carbon dots from sodium lignosulfonate/melamine formaldehyde foam and its fluorescence detection of trivalent iron ions. *RSC Advances, 11*(39), 24038–24043. https://doi.org/10.1039/d1ra03279h

Reckmeier, C. J., Wang, Y., Zboril, R., & Rogach, A. L. (2016). Influence of Doping and Temperature on Solvatochromic Shifts in Optical Spectra of Carbon Dots. *The Journal of Physical Chemistry C, 120*(19), 10591–10604. https://doi.org/10.1021/acs.jpcc.5b12294

Ross, S., Wu, R. S., Wei, S. C., Ross, G. M., & Chang, H. T. (2020). The analytical and biomedical applications of carbon dots and their future theranostic potential: A review. *Journal of Food and Drug Analysis, 28*(4), 678–696. https://doi.org/10.38212/2224-6614.1154

Shang, W., Ye, M., Cai, T., Zhao, L., Zhang, Y., Liu, D., & Liu, S. (2018). Tuning of the hydrophilicity and hydrophobicity of nitrogen doped carbon dots: A facile approach towards high efficient lubricant nanoadditives. *Journal of Molecular Liquids, 266*, 65–74. https://doi.org/10.1016/j.molliq.2018.06.042

Sharma, A., & Das, J. (2019). Small molecules derived carbon dots: Synthesis and applications in sensing, catalysis, imaging, and biomedicine. *Journal of Nanobiotechnology, 17*(1), 1–24. https://doi.org/10.1186/s12951-019-0525-8

Shen, S., Wang, S., Zheng, R., Zhu, X., Jiang, X., Fu, D., & Yang, W. (2015). Magnetic nanoparticle clusters for photothermal therapy with near-infrared irradiation. *Biomaterials, 39*, 67–74. https://doi.org/10.1016/j.biomaterials.2014.10.064

Shibu, E. S., Hamada, M., Murase, N., & Biju, V. (2013). Nanomaterials formulations for photothermal and photodynamic therapy of cancer. *Journal of Photochemistry and Photobiology C: Photochemistry Reviews, 15*, 53–72. https://doi.org/10.1016/j.jphotochemrev.2012.09.004

Simões, E. F. C., Leitão, J. M. M., & da Silva, J. C. G. E. (2016). Carbon dots prepared from citric acid and urea as fluorescent probes for hypochlorite and peroxynitrite. *Microchimica Acta, 183(*5), 1769–1777. https://doi.org/10.1007/s00604-016-1807-6

Steitz, B., Hofmann, H., Kamau, S. W., Hassa, P. O., Hottiger, M. O., von Rechenberg, B., Hofmann-Amtenbrink, M., & Petri-Fink, A. (2007). Characterization of PEI-coated superparamagnetic iron oxide nanoparticles for transfection: Size distribution, colloidal properties and DNA interaction. *Journal of Magnetism and Magnetic Materials, 311*(1), 300–305. https://doi.org/10.1016/j.jmmm.2006.10.1194

Sun, S., Zhang, L., Jiang, K., Wu, A., & Lin, H. (2016). Toward High-Efficient Red Emissive Carbon Dots: Facile Preparation, Unique Properties, and Applications as Multifunctional Theranostic Agents. *Chemistry of Materials*, *28*(23), 8659–8668. https://doi.org/10.1021/acs.chemmater.6b03695

Tang, Q., Si, W., Huang, C., Ding, K., Huang, W., Chen, P., Zhang, Q., & Dong, X. (2017). An aza-BODIPY photosensitizer for photoacoustic and photothermal imaging guided dual modal cancer phototherapy. *Journal of Materials Chemistry B*, *5*(8), 1566–1573. https://doi.org/10.1039/c6tb02979e

Tao, H., Yang, K., Ma, Z., Wan, J., Zhang, Y., Kang, Z., & Liu, Z. (2011). In Vivo NIR Fluorescence Imaging, Biodistribution, and Toxicology of Photoluminescent Carbon Dots Produced from Carbon Nanotubes and Graphite. *Small*, *8*(2), 281–290. https://doi.org/10.1002/smll.201101706

Ulissi, Z. W., Sen, F., Gong, X., Sen, S., Iverson, N., Boghossian, A. A., Godoy, L. C., Wogan, G. N., Mukhopadhyay, D., & Strano, M. S. (2014). Spatiotemporal Intracellular Nitric Oxide Signaling Captured Using Internalized, Near-Infrared Fluorescent Carbon Nanotube Nanosensors. *Nano Letters*, *14*(8), 4887–4894. https://doi.org/10.1021/nl502338y

Ulusoy Ghobadi, T. G., Akhuseyin Yildiz, E., Buyuktemiz, M., Sadigh Akbari, S., Topkaya, D., İSci, M., Dede, Y., Yaglioglu, H. G., & Karadas, F. (2018). A Noble-Metal-Free Heterogeneous Photosensitizer-Relay Catalyst Triad That Catalyzes Water Oxidation under Visible Light. *Angewandte Chemie International Edition*, *57*(52), 17173–17177. https://doi.org/10.1002/anie.201811570

Wang, H., Sun, C., Chen, X., Zhang, Y., Colvin, V. L., Rice, Q., Seo, J., Feng, S., Wang, S., & Yu, W. W. (2017). Excitation wavelength independent visible color emission of carbon dots. *Nanoscale*, *9*(5), 1909–1915. https://doi.org/10.1039/c6nr09200d

Wang, Y., & Hu, A. (2014). Carbon quantum dots: synthesis, properties and applications. *Journal of Materials Chemistry C*, *2*(34), 6921. https://doi.org/10.1039/c4tc00988f

Wang, Y., Anilkumar, P., Cao, L., Liu, J. H., Luo, P. G., Tackett, K. N., Sahu, S., Wang, P., Wang, X., & Sun, Y. P. (2011). Carbon dots of different composition and surface functionalization: cytotoxicity issues relevant to fluorescence cell imaging. *Experimental Biology and Medicine*, *236*(11), 1231–1238. https://doi.org/10.1258/ebm.2011.011132

Wang, Y., Zhuang, Q., & Ni, Y. (2015). Facile Microwave-Assisted Solid-Phase Synthesis of Highly Fluorescent Nitrogen-Sulfur-Codoped Carbon Quantum Dots for Cellular Imaging Applications. *Chemistry - A European Journal*, *21*(37), 13004–13011. https://doi.org/10.1002/chem.201501723

Wikipedia contributors. (2021, December 12). Melamine. Wikipedia. https://en.wikipedia.org/wiki/Melamine

Wu, M., Zhan, J., Geng, B., He, P., Wu, K., Wang, L., Xu, G., Li, Z., Yin, L., & Pan, D. (2017). Scalable synthesis of organic-soluble carbon quantum dots: superior optical properties in solvents, solids, and LEDs. *Nanoscale*, *9*(35), 13195–13202. https://doi.org/10.1039/c7nr04718e

Xie, S., Li, X., Wang, L., Zhu, F., Zhao, X., Yuan, T., Liu, Q., & Chen, X. (2021). High quantum-yield carbon dots embedded metal-organic frameworks for selective and sensitive detection of dopamine. *Microchemical Journal*, *160*, 105718. https://doi.org/10.1016/j.microc.2020.105718

Xu, X., Zhang, K., Zhao, L., Li, C., Bu, W., Shen, Y., Gu, Z., Chang, B., Zheng, C., Lin, C., Sun, H., & Yang, B. (2016). Aspirin-Based Carbon Dots, a Good Biocompatibility of Material Applied for Bioimaging and Anti-Inflammation. *ACS Applied Materials & Interfaces*, *8*(48), 32706–32716. https://doi.org/10.1021/acsami.6b12252

Xu, X., Ray, R., Gu, Y., Ploehn, H. J., Gearheart, L., Raker, K., & Scrivens, W. A. (2004). Electrophoretic Analysis and Purification of Fluorescent Single-Walled Carbon Nanotube Fragments. *Journal of the American Chemical Society*, *126*(40), 12736–12737. https://doi.org/10.1021/ja040082h

Yan, F., Sun, Z., Zhang, H., Sun, X., Jiang, Y., & Bai, Z. (2019). The fluorescence mechanism of carbon dots, and methods for tuning their emission color: a review. *Microchimica Acta*, *186*(8). https://doi.org/10.1007/s00604-019-3688-y

Yang, H., Liu, Y., Guo, Z., Lei, B., Zhuang, J., Zhang, X., Liu, Z., & Hu, C. (2019). Hydrophobic carbon dots with blue dispersed emission and red aggregation-induced emission. *Nature Communications*, *10*(1). https://doi.org/10.1038/s41467-019-09830-6

Yang, S. T., Wang, X., Wang, H., Lu, F., Luo, P. G., Cao, L., Meziani, M. J., Liu, J. H., Liu, Y., Chen, M., Huang, Y., & Sun, Y. P. (2009). Carbon Dots as Nontoxic and High-Performance Fluorescence Imaging Agents. *The Journal of Physical Chemistry C*, *113*(42), 18110–18114. https://doi.org/10.1021/jp9085969

Yetisgin, A. A., Cetinel, S., Zuvin, M., Kosar, A., & Kutlu, O. (2020). Therapeutic Nanoparticles and Their Targeted Delivery Applications. *Molecules*, *25*(9), 2193. https://doi.org/10.3390/molecules25092193

Zhang, H., Chen, Y., Liang, M., Xu, L., Qi, S., Chen, H., & Chen, X. (2014). Solid-Phase Synthesis of Highly Fluorescent Nitrogen-Doped Carbon Dots for Sensitive and Selective Probing Ferric Ions in Living Cells. *Analytical Chemistry*, *86*(19), 9846–9852. https://doi.org/10.1021/ac502446m

Zhang, L., Han, Y., Zhu, J., Zhai, Y., & Dong, S. (2015). Simple and Sensitive Fluorescent and Electrochemical Trinitrotoluene Sensors Based on Aqueous Carbon Dots. *Analytical Chemistry*, *87*(4), 2033–2036. https://doi.org/10.1021/ac5043686

Zhang, T., Zhu, J., Zhai, Y., Wang, H., Bai, X., Dong, B., Wang, H., & Song, H. (2017). A novel mechanism for red emission carbon dots: hydrogen bond dominated molecular states emission. *Nanoscale*, *9*(35), 13042–13051. https://doi.org/10.1039/c7nr03570e

Zhang, X., Huang, H., Liu, J., Liu, Y., & Kang, Z. (2013). Carbon quantum dots serving as spectral converters through broadband upconversion of near-infrared photons for photoelectrochemical hydrogen generation. *Journal of Materials Chemistry A*, *1*(38), 11529. https://doi.org/10.1039/c3ta12568h

Zhang, Y., Zhan, X., Xiong, J., Peng, S., Huang, W., Joshi, R., Cai, Y., Liu, Y., Li, R., Yuan, K., Zhou, N., & Min, W. (2018). Temperature-dependent cell death patterns induced by functionalized gold nanoparticle photothermal therapy in melanoma cells. *Scientific Reports*, *8*(1). https://doi.org/10.1038/s41598-018-26978-1

Zhao, F., Yao, D., Guo, R., Deng, L., Dong, A., & Zhang, J. (2015). Composites of Polymer Hydrogels and Nanoparticulate Systems for Biomedical and Pharmaceutical Applications. *Nanomaterials*, *5*(4), 2054–2130. https://doi.org/10.3390/nano5042054

Zheng, M., Liu, S., Li, J., Qu, D., Zhao, H., Guan, X., Hu, X., Xie, Z., Jing, X., & Sun, Z. (2014). Integrating Oxaliplatin with Highly Luminescent Carbon Dots: An Unprecedented Theranostic Agent for Personalized Medicine. *Advanced Materials*, *26*(21), 3554–3560. https://doi.org/10.1002/adma.201306192

Zheng, Y., Zheng, J., Wang, J., Yang, Y., Lu, T., & Liu, X. (2020). Facile Preparation of Stable Solid-State Carbon Quantum Dots with Multi-Peak Emission. *Nanomaterials*, *10*(2), 303. https://doi.org/10.3390/nano10020303

Zhou, B., Guo, Z., Lin, Z., Zhang, L., Jiang, B. P., & Shen, X. C. (2019b). Recent insights into near-infrared light-responsive carbon dots for bioimaging and cancer phototherapy. *Inorganic Chemistry Frontiers*, *6*(5), 1116–1128. https://doi.org/10.1039/c9qi00201d

Zhu, S., Song, Y., Zhao, X., Shao, J., Zhang, J., & Yang, B. (2015). The photoluminescence mechanism in carbon dots (graphene quantum dots, carbon nanodots, and polymer dots): current state and future perspective. *Nano Research*, *8*(2), 355–381. https://doi.org/10.1007/s12274-014-0644-3

Zhu, Z., Zhai, Y., Li, Z., Zhu, P., Mao, S., Zhu, C., Du, D., Belfiore, L. A., Tang, J., & Lin, Y. (2019). Red carbon dots: Optical property regulations and applications. *Materials Today*, *30*, 52–79. https://doi.org/10.1016/j.mattod.2019.05.003